This manuscript is a non-peer-reviewed preprint

submitted to EarthArXiv.

Subsequent versions of this manuscript may have

slightly different content.

submitted to *Geophys. J. Int.*

Ambient Noise Surface-Wave Polarization in Anisotropic Media: Theory, Measurement, and Interpretation

Xiongwei Liu and Michael H. Ritzwoller,

Department of Physics, University of Colorado Boulder, Boulder, CO 80309, USA.

E-mail:xiongwei.liu@colorado.edu

SUMMARY

We develop an adiabatic theory and practical methodology for measuring quasi-Rayleigh and quasi-Love polarization from the complete ambient noise cross-correlation tensor. The formulation allows the polarization parameters at both stations of a pair to be estimated jointly and, under sufficiently adiabatic propagation, interpreted in terms of local anisotropic structure at those locations. A new empirical processing step approximates the theoretical source-group normalization to reduce source-related amplitude effects, providing the practical link between observations and theory. In geologically relevant limiting regimes, simple relations link diagonal carrier (TT, ZZ) and off-diagonal polarization-sensitive (TZ, ZT) waveforms, yielding information complementary to conventional phase-speed observations.

In numerical benchmarks, predictions of the polarization-sensitive waveforms are accurate when anisotropy varies sufficiently slowly relative to wavelength. Stronger or shorter-scale structural variations can increase conversion between the two wave types, degrading the adiabatic approximation and local interpretability of measured polarization.

We present the first measurements of surface-wave polarization from ambient noise cross-correlations in Alaska, focusing on the 20–30 s period band. For relatively short paths

south of the Denali Fault, repeated polarization estimates are mutually consistent and broadly consistent between the two station endpoints, supporting a local interpretation. For paths crossing the fault, boundary-transient behavior develops, waveform fits degrade on average, and the polarization parameters change systematically, consistent with a breakdown of local interpretation across a strong structural boundary. Finally, in this example, adding a single polarization constraint to an inversion of Rayleigh- and Love-wave 2ψ and 4ψ phase-speed observations resolves a dip-orientation nonuniqueness that remains in the phase-speed-only inversion. The alternative dip solutions correspond to distinct three-dimensional orientations of the anisotropic fabric and may have important tectonic implications.

1 INTRODUCTION

Surface-wave polarization has the potential to provide information about the anisotropic structure of the Earth that complements the phase-speed observations used in most surface-wave inversions. Whether it can provide a local constraint depends on how polarization evolves during propagation through laterally varying anisotropic structure. If mode conversion and scattering remain weak, polarization can retain a meaningful relationship to local structure; if they become appreciable, polarization may remain measurable but need not be locally interpretable.

Surface waves propagating in isotropic media have particularly simple polarizations. Love waves are linearly polarized transverse to the direction of propagation, whereas Rayleigh waves are elliptically polarized in the radial-vertical plane. In anisotropic media, surface waves are referred to as quasi-Rayleigh and quasi-Love waves, and their polarizations are generally more complex and three-dimensional, although they retain their simpler forms in a transversely isotropic medium with a vertical symmetry axis (VTI).

In this paper, we address two principal questions. First, how can the distinct polarizations of quasi-Rayleigh and quasi-Love waves be measured reliably from ambient noise observations? Second, how can those measurements be interpreted in terms of the anisotropic elastic structure of the Earth, and under what propagation conditions is a local interpretation justified? We address these questions using surface waves recovered from seismic ambient noise cross-correlations. In this setting, an important observational challenge is that quasi-Rayleigh and quasi-Love waveforms commonly overlap at the relatively short inter-station distances used in continental ambient noise studies, as illustrated in Fig-

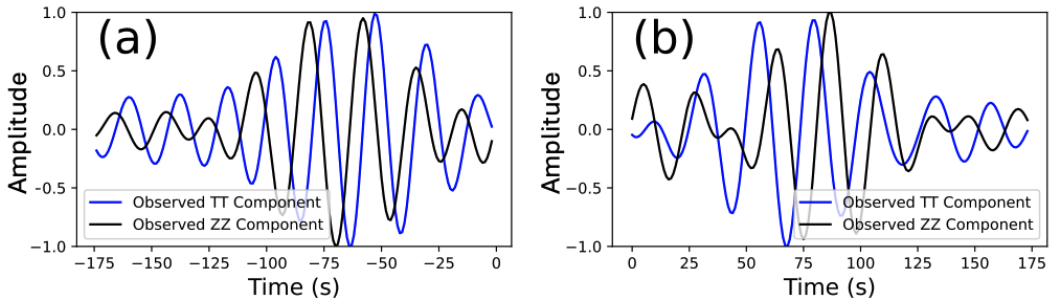

Figure 1. Vertical–vertical (ZZ, black) and transverse–transverse (TT, blue) ambient noise cross-correlations between stations AK.BAE and AV.WACK in southern Alaska, separated by 223 km and filtered in the 20–30 s period band. (a) Negative lag; (b) positive lag. The ZZ and TT waveforms are dominated by quasi-Rayleigh and quasi-Love waves, respectively, whose arrivals overlap strongly at both lags.

ure 1. Their individual particle motions therefore cannot generally be isolated simply by separating their arrivals in time.

Teleseismic surface-wave observations have provided evidence for the effects of anisotropy on quasi-Rayleigh and quasi-Love wave propagation. Early studies used the presence and amplitude of scattered energy to identify strong lateral gradients in upper-mantle anisotropy (Park & Yu, 1992; Yu & Park, 1994; Yu et al., 1995; Levin & Park 1998; Levin et al., 2007; Rieger & Park, 2010). Subsequent studies used the differential timing of scattered quasi-Rayleigh and quasi-Love waves to estimate the location of anisotropic gradients along the propagation path and applied the method to continental margins and other tectonic boundaries (Servali et al., 2020; Cheng et al., 2021 and 2026; Eakin, 2021; Merry & Eakin, 2024). In a distinct approach, Pettersen & Maupin (2002) directly measured anomalous polarization of fundamental-mode quasi-Rayleigh waves without explicitly considering scattering between quasi-Rayleigh and quasi-Love waves. This study showed that polarization itself can provide useful information about anisotropic structure, although a general theory relating the measured polarization directly to the elastic tensor was not then available.

In addition to teleseismic studies, a series of investigations demonstrated that surface-wave polarization in anisotropic media can be measured from ambient noise cross-correlations. Durand et al. (2011) addressed the problem of overlapping quasi-Rayleigh and quasi-Love waveforms using the complete nine-component cross-correlation tensor. They introduced an optimal-rotation procedure that rotates the coordinate systems at the two stations to minimize energy in the off-diagonal components, thereby defining horizontal and vertical rotation angles that characterize polarization anomalies. Applications of this approach, together with numerical simulations, showed that the measured polarization anomalies are sensitive to the strength, depth, and orientation of anisotropy and can vary through

time in response to changes in Earth structure (e.g., Durand et al., 2011; Saade et al., 2015, 2017, 2019).

These studies established that surface-wave polarization anomalies are observable in ambient noise cross-correlations and are highly sensitive to anisotropy. Their principal emphasis, however, was on polarization as a diagnostic of anisotropy or structural change rather than as an independent observable to be related quantitatively to the elastic tensor. Moreover, the optimal-rotation approach represents the quasi-Rayleigh and quasi-Love polarizations through a common rotation of the coordinate system, whereas in a generally anisotropic medium the two wave types can possess distinct polarization states that cannot be represented by a single rotation. In addition, these studies did not establish the general relationship between the distinct quasi-Rayleigh and quasi-Love polarization states and the elastic tensor.

Tanimoto (2004) established an important premise of the present study: polarization can, in principle, provide constraints on anisotropic structure that are complementary to and distinct from those obtained from phase speed. In particular, this study emphasized the vertical component of quasi-Love-wave polarization and derived its depth-dependent sensitivity to anisotropic structure. However, Tanimoto's formulation represents Rayleigh–Love coupling with a real mixing coefficient, which is appropriate when the imaginary component of the mixing coefficient vanishes or is negligible, as in transversely isotropic media with a horizontal symmetry axis (HTI). This restriction is not generally valid for transversely isotropic media with a tilted symmetry axis (TTI) or for more general anisotropic media.

Liu & Ritzwoller (2025) presented a more general theory of Rayleigh–Love coupling and the polarization of quasi-Rayleigh and quasi-Love waves. In this theory, the mixing coefficient is generally complex, and the formulation applies to media of general anisotropic symmetry. It provides the foundation used here to relate measurable quasi-Rayleigh and quasi-Love polarization states to the elastic tensor.

The complete nine-component ambient noise cross-correlation tensor commonly contains coherent energy in several off-diagonal components, as illustrated in Figure 2. In particular, the TZ and ZT components can contain polarization-sensitive signals even when the quasi-Rayleigh and quasi-Love waveforms overlap in time. We show here that their polarization can be measured from the appropriately normalized cross-correlation tensor. The theory requires a source-group normalization that removes source-related amplitude factors, and we introduce a new empirical processing step that approximates this normalization in observed ambient noise cross-correlations. After normalization, the dominant TT and ZZ components provide the quasi-Love and quasi-Rayleigh carrier waveforms, whereas the off-diagonal TZ and ZT components contain the polarization-sensitive perturbations. In

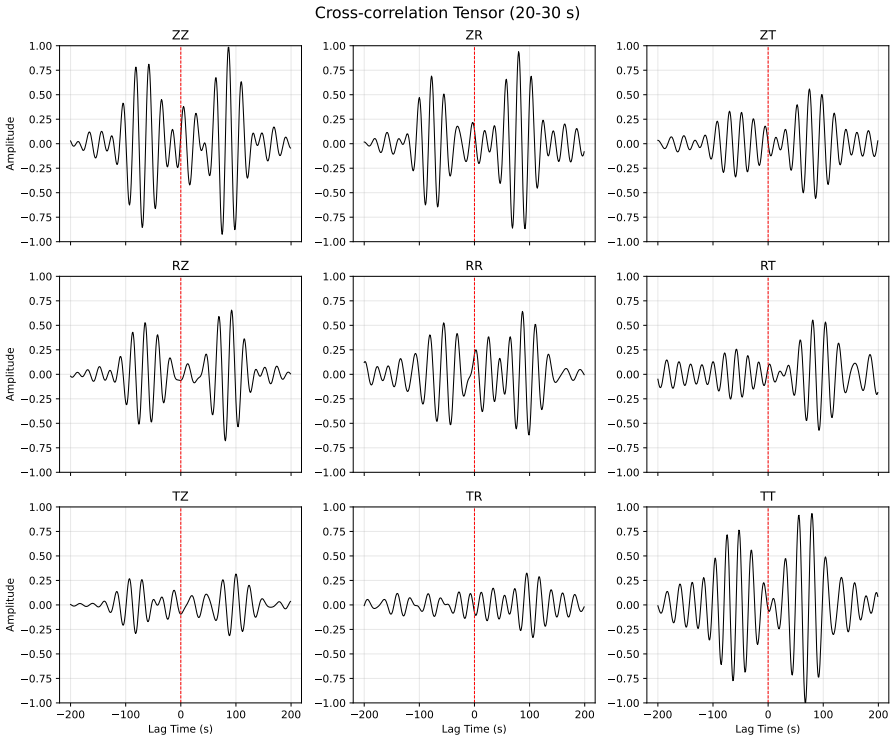

Figure 2. Nine-component ambient noise cross-correlation tensor for stations AK.BAE and AV.WACK emerging from Phase 2 of the data processing, expressed in the R, T, Z station-pair coordinate system and filtered in the 20–30 s period band. Off-diagonal components show considerable amplitudes and contain information about surface-wave polarization that constrains anisotropy.

physically motivated limiting regimes, these four components satisfy simple linear waveform relations that permit the polarization parameters at the two station locations to be estimated jointly, without requiring the overlapping quasi-Rayleigh and quasi-Love waves to be separated in time.

Reliable measurement of polarization does not by itself guarantee that the measurements can be interpreted in terms of local Earth structure. Such an interpretation requires sufficiently adiabatic propagation (e.g., Tromp & Dahlen, 1993; Tromp, 1994b), in which the polarization of quasi-Rayleigh and quasi-Love waves adjusts continuously to changes in the local anisotropic structure with negligible mode conversion between the two wave types. When nonadiabatic mode conversion becomes appreciable, the wavefield can retain information about structural variations encountered along the propagation path. Polarization may therefore remain measurable even when its relationship to the local anisotropic structure is no longer straightforward.

A useful operational condition for adiabatic propagation is that the characteristic length scale $\ell_{\mathrm{structure}}$ over which the anisotropic structure changes be large compared with the wavelength λ_{wave}

of the propagating surface wave,

$$\frac{\ell_{\mathrm{structure}}}{\lambda_{\mathrm{wave}}} \gg 1. \tag{1}$$

Equation (1) captures the role of structural length scale but is not a complete adiabaticity condition. Adiabaticity also depends on the amplitude of the structural variation and the separation of the quasi-Rayleigh and quasi-Love branches, as shown by the reduced two-mode analysis presented in the Supplementary Materials. We use equation (1) as an operational guide in the numerical benchmarks below and return to the more complete physical interpretation in Section 6.1.

The remainder of the paper addresses both the measurement and interpretation of surface-wave polarization. We first develop the theory relating the source-group-normalized ambient noise cross-correlation tensor to the distinct quasi-Rayleigh and quasi-Love polarization states and identify the assumptions underlying the working waveform relations. We then use numerical experiments to test the forward theory and parameter inference in benchmark models with different degrees of lateral variation in anisotropy. Next, we introduce an empirical source-group normalization and apply the resulting measurement procedure to ambient noise observations in Alaska to assess whether the polarization measurements can be interpreted meaningfully in terms of local anisotropic structure. Finally, we compare inversions using Rayleigh- and Love-wave phase-speed observations alone with a joint inversion that also includes polarization and show that polarization resolves a dip-orientation ambiguity that remains when only the phase-speed observations are used.

2 THEORY AND PHYSICAL ASSUMPTIONS

The complete theoretical derivation is presented in Appendix A. Here we summarize the principal assumptions underlying the working polarization relations and discuss their physical roles. The formulation combines several distinct approximations and limiting regimes. Adiabatic propagation permits the polarization to remain related to the local anisotropic structure as the waves propagate. The two-mode approximation represents the local quasi-Rayleigh and quasi-Love polarization states within the fundamental Rayleigh–Love subspace. Weak Rayleigh–Love mixing permits a first-order relation between polarization and the elastic tensor, and the X- and E-dominant limits yield simple working equations for estimating the polarization parameters at two fixed station locations. The numerical benchmarks in Section 3 evaluate the performance of the resulting forward theory and parameter inference in specific synthetic models rather than testing each of these assumptions independently.

For each station pair, we designate one station as the fixed reference station and the other as the fixed field station. The observational R, T, Z coordinate system is defined once, with $\hat{\boldsymbol{R}}$ directed from the reference station toward the field station, and the same axes are retained at both correlation lags. In

a cross-correlation component XY, the first letter denotes the component at the reference station and the second denotes the component at the field station. In the Green-tensor interpretation, the source and receiver roles change with lag: positive lag propagation is from the reference station to the field station, and negative lag propagation is in the reverse direction, from the field station to the reference station. Thus the reference station serves as the source location at positive lag and the receiver location at negative lag; the field station has the opposite roles. Fixed endpoint quantities are denoted by the subscripts ref and fld.

2.1 Adiabatic propagation and local interpretability

If the anisotropic structure varies sufficiently slowly along the propagation path, a surface wave remains on its continuously evolving local eigenbranch with negligible mode conversion to other branches. Its polarization then adjusts to the local structure, so that the polarizations at the reference and field stations retain a local relationship to the anisotropic structure at those locations. Such propagation is referred to as adiabatic. Equation (1) provides a useful condition for adiabaticity, expressing the requirement that the medium change little over one wavelength. It is not a complete criterion: the amplitude of the structural variation, the separation between neighboring modal branches, and the rate at which their eigenfunctions change also affect mode conversion. We use equation (1) as an operational guide in the numerical benchmarks of Section 3 and return to the more complete physical interpretation in Section 6.1.

Under the adiabatic approximation and motivated by Tromp & Dahlen (1993) and Tromp (1994b), the positive-lag far-field Green tensor in an anisotropic medium in the frequency (ω) domain is written in Appendix A as

$$G_{YX}(\boldsymbol{x}_{\mathrm{fld}}, \boldsymbol{x}_{\mathrm{ref}}, \omega) \simeq \sum_{\nu} \frac{(\boldsymbol{p}^{\nu}_{\mathrm{fld}})_Y (\boldsymbol{p}^{\nu *}_{\mathrm{ref}})_X}{I_1^{\nu} D_{\nu}} \exp(\mathrm{i}\Phi_{\nu}), \tag{2}$$

which is equation (A.2). Here $\boldsymbol{p}^{\nu}_{\mathrm{ref}}$ and $\boldsymbol{p}^{\nu}_{\mathrm{fld}}$ are the local polarization eigenvectors at the two fixed station locations, I_1^{ν} is the modal normalization factor, D_{ν} is the propagation factor, and Φ_{ν} is the modal phase. The Green-tensor element G_{YX} is displacement in direction Y at the field station produced by a force in direction X at the reference station. The modal index ν spans all relevant local surface-wave branches; adiabaticity does not itself truncate this sum. The subsequent two-mode treatment introduced in Section 2.2 focuses on the fundamental quasi-Rayleigh and quasi-Love branches that are central to the present measurements.

If rapid lateral variations cause adiabaticity to fail, the Green tensor must account for path-dependent scattering and mode conversion. At an abrupt change in anisotropic structure, the polarization of an incident wave will not, in general, match a single wave type supported on the other side,

so energy can be redistributed among reflected and transmitted quasi-Rayleigh and quasi-Love waves and, where significant, surface-wave overtones. Even a single abrupt transition can therefore produce a downstream wavefield whose polarization depends on its scattering history as well as on the local structure. Additional structural changes can increase this complexity. Polarization may remain measurable, but its relationship to the local anisotropic structure can no longer necessarily be interpreted uniquely.

2.2 The two-mode approximation

The two-mode approximation represents the local quasi-Rayleigh and quasi-Love eigenfunctions in terms of the fundamental Rayleigh and Love modes of a local isotropic or VTI reference model. At a given horizontal position, the exact local quasi-Love and quasi-Rayleigh eigenfunctions can be decomposed as

$$\boldsymbol{p}_{qL} = a_L \boldsymbol{p}_L^0 + b_L \boldsymbol{p}_R^0 + \boldsymbol{\eta}^L, \tag{3}$$

$$\boldsymbol{p}_{qR} = a_R \boldsymbol{p}_R^0 + b_R \boldsymbol{p}_L^0 + \boldsymbol{\eta}^R, \tag{4}$$

corresponding to equations (A.12) and (A.13). The reference vectors $\boldsymbol{p}_L^0$ and $\boldsymbol{p}_R^0$ are the fundamental Love and Rayleigh eigenfunctions, whereas $\boldsymbol{\eta}^L$ and $\boldsymbol{\eta}^R$ are orthogonal to their span. These residuals describe the parts of the local anisotropic eigenfunctions that cannot be represented by mixing only the two fundamental reference modes.

The two-mode approximation assumes that the residuals contribute only at second order, $\boldsymbol{\eta}^L, \boldsymbol{\eta}^R = \mathcal{O}(\epsilon^2)$. With the normalization and weak-mixing assumptions developed in Appendix A, the local eigenfunctions then reduce to

$$\boldsymbol{p}_{qL} = \boldsymbol{p}_L^0 + \chi \boldsymbol{p}_R^0 + \mathcal{O}(\epsilon^2), \tag{5}$$

$$\boldsymbol{p}_{qR} = \boldsymbol{p}_R^0 - \chi^* \boldsymbol{p}_L^0 + \mathcal{O}(\epsilon^2), \tag{6}$$

which are equations (A.22) and (A.23). The complex mixing coefficient χ therefore describes the first-order mixing of the fundamental Rayleigh and Love polarizations. The approximation becomes inaccurate if contributions outside this two-mode representation become important. First-order corrections for non-negligible residuals are developed in Section 2 of the Supplementary Materials.

Under the phase convention of Appendix A, the reference Love eigenfunction is transverse, $\boldsymbol{p}_L^0 = (0, W, 0)^T$, and the reference Rayleigh eigenfunction lies in the vertical plane, $\boldsymbol{p}_R^0 = (V, 0, \mathrm{i}U)^T$ [equation (A.9)]. Equations (5) and (6) therefore give $\boldsymbol{p}_{qL} = (\chi V, W, \mathrm{i}\chi U)^T$ and $\boldsymbol{p}_{qR} = (V, -\chi^* W, \mathrm{i}U)^T$ [equations (A.31) and (A.32)].

The polarization geometry is particularly simple in the X-dominant regime, where X is a real

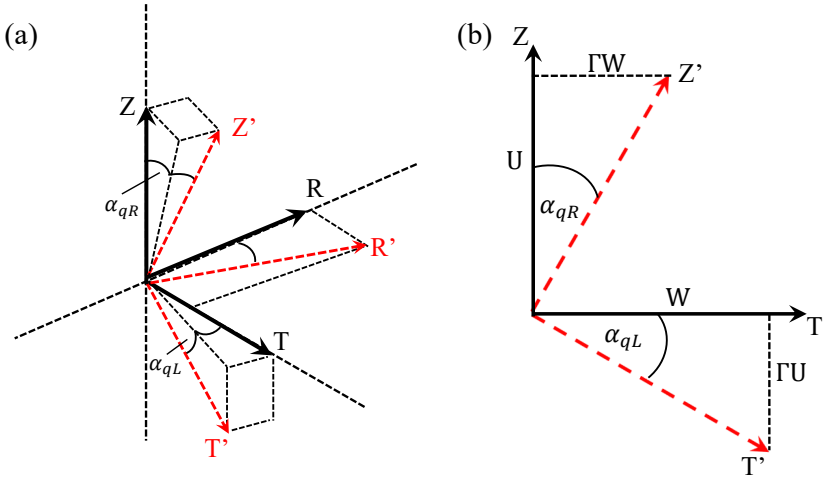

Figure 3. Surface-wave polarization geometry in the X-dominant regime. (a) Schematic perturbation of the reference Rayleigh- and Love-wave polarizations in an isotropic medium to the quasi-Rayleigh and quasi-Love polarizations in an anisotropic medium. The red dashed primed directions indicate the perturbed polarization directions; any horizontal rotation about the Z axis is omitted for clarity. (b) Relationship between the signed polarization parameter Γ and the quasi-Rayleigh and quasi-Love polarization angles in the Z–T plane, $\tan\alpha_{qR} = \Gamma W(0)/U(0)$ and $\tan\alpha_{qL} = \Gamma U(0)/W(0)$. Here $U(0)$ and $W(0)$ are the surface amplitudes of the reference Rayleigh- and Love-wave eigenfunctions. A single Γ governs both modes, but in general $\alpha_{qR} \neq \alpha_{qL}$. Panel (a) is inspired by Durand et al. (2011).

depth integral of the elastic tensor and reference eigenfunctions that controls the imaginary part of the Rayleigh–Love mixing coefficient χ. The quantities X and χ are defined explicitly in Section 2.3. In this regime, to first order, $\chi = \mathrm{i}\Gamma$, where Γ is a signed real polarization parameter.

The corresponding quasi-Rayleigh and quasi-Love polarization angles in the Z–T plane satisfy

$$\tan\alpha_{qR} = \Gamma\frac{W(0)}{U(0)}, \tag{7}$$

$$\tan\alpha_{qL} = \Gamma\frac{U(0)}{W(0)}, \tag{8}$$

where terms of order ϵ^2 are omitted. Thus, a single Γ governs the first-order polarization of both modes, although generally $\alpha_{qR} \neq \alpha_{qL}$. Figure 3 illustrates this polarization geometry. Representative values of W/U are presented in Section 2.5.

2.3 Weak anisotropy, Rayleigh–Love mixing, and the cross-correlation tensor

Within the two-mode approximation, the quasi-degenerate coupling theory of Liu & Ritzwoller (2025) gives the mixing coefficient that controls the first-order polarization of quasi-Rayleigh and quasi-Love

waves [equations (A.31) and (A.32)]:

$$\chi = \frac{E + \mathrm{i}X}{A - B}, \tag{9}$$

which is equation (A.24). The real-valued quantities A, B, E, and X are depth integrals of the elastic tensor and the reference eigenfunctions. The complex quantity $E + \mathrm{i}X$ describes the anisotropic coupling between the reference Rayleigh and Love modes, whereas $|A - B|$ measures their separation in the perturbation theory. Because E and X are linear depth integrals of the anisotropic elastic parameters, their magnitudes generally increase with the strength of the relevant anisotropy. Their explicit dependence on the elastic tensor is given by equations (A.27)–(A.30), providing the direct connection between surface-wave polarization and anisotropic structure.

The coupling calculation evaluates the reference Rayleigh and Love modes at a nearly common wavenumber, whereas the Green tensor is evaluated at fixed frequency, where the two branches generally have slightly different wavenumbers. We assume that the reference eigenfunctions and mixing coefficient change negligibly across this small wavenumber difference. In general, χ is complex and may be written $\chi = \widetilde{\Gamma} e^{\mathrm{i}\phi}$, where $\widetilde{\Gamma} = |\chi| \geq 0$ and ϕ is its phase. The signed polarization parameter Γ used below is introduced in the X- and E-dominant limits.

For the weak-anisotropy theory, we require the resulting Rayleigh–Love mixing to remain small,

$$|\chi| = \frac{(E^2 + X^2)^{1/2}}{|A - B|} \ll 1. \tag{10}$$

Stronger anisotropy generally produces stronger mixing, although even weak anisotropy can produce strong mixing if the reference branches approach degeneracy, in which case the first-order approximation may fail. The first-order theory neglects terms of order $|\chi|^2$.

The ambient noise cross-correlation tensor contains source-related amplitude factors that depend on the ambient noise source distribution (e.g., Stehly et al., 2006) and effective source direction. These factors must be accounted for before relative amplitudes among tensor components can be interpreted in terms of polarization. We assume that, even for an uneven noise-source distribution, the positive- and negative-lag cross-correlations remain proportional to the corresponding Green tensors, with their asymmetry represented by source-strength factors associated with the radial, transverse, and vertical effective source directions. Appendix A introduces a theoretical source-group normalization [equations (A.47)–(A.49) and (A.81)] that removes these factors within the assumptions of the theory. Components with the same effective source direction are normalized together: at positive lag the first component index identifies the source group, whereas at negative lag the second component index does so. For real data, the theoretical normalization factors are not known and must be approximated empirically. In Section 4.2, we therefore estimate their magnitudes from the observed TT and ZZ

carrier amplitude spectra within each narrow frequency band. The polarization relations below apply to the source-group-normalized tensor, not directly to the unnormalized observations. This empirical normalization provides the practical link between the observed cross-correlations and the theoretical polarization relations that connect polarization to the elastic tensor.

The theoretically source-group-normalized positive-lag cross-correlation tensor, representing propagation from the reference station to the field station, is [equation (A.63)]

$$\widetilde{\boldsymbol{C}}^{+} \equiv \begin{pmatrix} RR^{+} & TR^{+} & ZR^{+} \\ RT^{+} & TT^{+} & ZT^{+} \\ RZ^{+} & TZ^{+} & ZZ^{+} \end{pmatrix} = \begin{pmatrix} ZZ^{+} & -\mathrm{i}\dfrac{V_{\mathrm{fld}}}{U_{\mathrm{fld}}}TZ^{+} & -\mathrm{i}\dfrac{V_{\mathrm{fld}}}{U_{\mathrm{fld}}}ZZ^{+} \\ \mathrm{i}\dfrac{U_{\mathrm{fld}}}{V_{\mathrm{fld}}}ZT^{+} & TT^{+} & ZT^{+} \\ \mathrm{i}\dfrac{U_{\mathrm{fld}}}{V_{\mathrm{fld}}}ZZ^{+} & TZ^{+} & ZZ^{+} \end{pmatrix} + \mathcal{O}(\epsilon^{2}). \tag{11}$$

At negative lag, propagation is from the field station to the reference station, and the corresponding normalized tensor is [equation (A.89)]

$$\widetilde{\boldsymbol{C}}^{-} \equiv \begin{pmatrix} RR^{-} & TR^{-} & ZR^{-} \\ RT^{-} & TT^{-} & ZT^{-} \\ RZ^{-} & TZ^{-} & ZZ^{-} \end{pmatrix} = \begin{pmatrix} ZZ^{-} & -\mathrm{i}\dfrac{U_{\mathrm{ref}}}{V_{\mathrm{ref}}}TZ^{-} & -\mathrm{i}\dfrac{U_{\mathrm{ref}}}{V_{\mathrm{ref}}}ZZ^{-} \\ \mathrm{i}\dfrac{V_{\mathrm{ref}}}{U_{\mathrm{ref}}}ZT^{-} & TT^{-} & ZT^{-} \\ \mathrm{i}\dfrac{V_{\mathrm{ref}}}{U_{\mathrm{ref}}}ZZ^{-} & TZ^{-} & ZZ^{-} \end{pmatrix} + \mathcal{O}(\epsilon^{2}). \tag{12}$$

Thus, to first order, the complete nine-component tensor at either lag is specified by four components: $TT^{\pm}$, $ZZ^{\pm}$, $TZ^{\pm}$, and $ZT^{\pm}$. The $TT^{\pm}$ and $ZZ^{\pm}$ components contain the quasi-Love and quasi-Rayleigh carrier waveforms, whereas $TZ^{\pm}$ and $ZT^{\pm}$ contain the independent polarization information used below. The remaining tensor components are determined algebraically from these four quantities.

2.4 X- and E-dominant polarization regimes

The first-order cross-correlation tensors in equations (11) and (12) remain valid even when E and X have comparable magnitudes. Two limiting regimes are especially useful, however, because they yield simple relationships among the observed waveforms. These are specializations of the weak-anisotropy theory, not additional modal approximations.

In the X-dominant regime, $X/(A-B) = \mathcal{O}(\epsilon)$ and $E/(A-B) = \mathcal{O}(\epsilon^{2})$. We define the signed polarization parameter, for $j = \mathrm{ref}, \mathrm{fld}$, with respect to the fixed reference-to-field azimuth by

$$\Gamma_{j} = \frac{X_{j}}{A_{j} - B_{j}}, \tag{13}$$

so that $\chi_{j} = \mathrm{i}\Gamma_{j} + \mathcal{O}(\epsilon^{2})$. A single Γ_{j} governs the first-order polarization of both the quasi-Rayleigh and quasi-Love waves at location j. Their polarization angles are not, in general, equal, because they depend differently on the reference eigenfunction ratio W/U [equations (7) and (8)].

Equation (A.30) shows that X contains 1ψ and 3ψ azimuthal variations; for the quasi-Rayleigh and quasi-Love waves considered here, the 1ψ terms are expected to dominate. The positive-lag relations between the polarization-sensitive off-diagonal components and the diagonal carrier components are [equations (A.65) and (A.66)]

$$TZ^{+} = \frac{U_{\mathrm{fld}}}{W_{\mathrm{fld}}}\left(-\Gamma_{\mathrm{fld}}TT^{+} + \Gamma_{\mathrm{ref}}ZZ^{+}\right), \tag{14}$$

$$ZT^{+} = \frac{W_{\mathrm{fld}}}{U_{\mathrm{fld}}}\left(-\Gamma_{\mathrm{ref}}TT^{+} + \Gamma_{\mathrm{fld}}ZZ^{+}\right). \tag{15}$$

The corresponding negative-lag equations [equations (A.93) and (A.94)] are

$$TZ^{-} = \frac{W_{\mathrm{ref}}}{U_{\mathrm{ref}}}\left(-\Gamma_{\mathrm{fld}}TT^{-} + \Gamma_{\mathrm{ref}}ZZ^{-}\right), \tag{16}$$

$$ZT^{-} = \frac{U_{\mathrm{ref}}}{W_{\mathrm{ref}}}\left(-\Gamma_{\mathrm{ref}}TT^{-} + \Gamma_{\mathrm{fld}}ZZ^{-}\right). \tag{17}$$

where terms of order ϵ^2 are suppressed. We present only TZ and ZT because, together with TT and ZZ, they determine the remaining elements of the cross-correlation tensor through equations (11) and (12).

In the E-dominant regime, $E/(A-B) = \mathcal{O}(\epsilon)$ and $X/(A-B) = \mathcal{O}(\epsilon^2)$, so $\chi_j = \Gamma_j + \mathcal{O}(\epsilon^2)$ with $\Gamma_j = E_j/(A_j - B_j)$. Equation (A.29) shows that E contains 2ψ and 4ψ azimuthal variations. The positive-lag equations [equations (A.71) and (A.72)] are

$$TZ^{+} = \mathrm{i}\frac{U_{\mathrm{fld}}}{W_{\mathrm{fld}}}\left(\Gamma_{\mathrm{fld}}TT^{+} - \Gamma_{\mathrm{ref}}ZZ^{+}\right), \tag{18}$$

$$ZT^{+} = \mathrm{i}\frac{W_{\mathrm{fld}}}{U_{\mathrm{fld}}}\left(-\Gamma_{\mathrm{ref}}TT^{+} + \Gamma_{\mathrm{fld}}ZZ^{+}\right). \tag{19}$$

The corresponding negative-lag equations [equations (A.95) and (A.96)] are

$$TZ^{-} = \mathrm{i}\frac{W_{\mathrm{ref}}}{U_{\mathrm{ref}}}\left(\Gamma_{\mathrm{fld}}TT^{-} - \Gamma_{\mathrm{ref}}ZZ^{-}\right), \tag{20}$$

$$ZT^{-} = \mathrm{i}\frac{U_{\mathrm{ref}}}{W_{\mathrm{ref}}}\left(-\Gamma_{\mathrm{ref}}TT^{-} + \Gamma_{\mathrm{fld}}ZZ^{-}\right). \tag{21}$$

The distinction between the two limiting regimes is controlled by the phase of the mixing coefficient. In the X-dominant regime the mixing coefficient is purely imaginary, producing a geometrical rotation of the quasi-Rayleigh and quasi-Love polarizations. In the E-dominant regime the mixing coefficient is purely real, placing the transverse and vertical perturbations in phase quadrature with the reference modes. When neither term is asymptotically smaller, the general complex-χ equations in Appendix A must be applied.

2.5 Representative values

Figures 4 and 5 illustrate representative values of the quantities discussed here. The calculations use synthetic models based on a three-dimensional Alaska model inferred from Rayleigh- and Love-wave

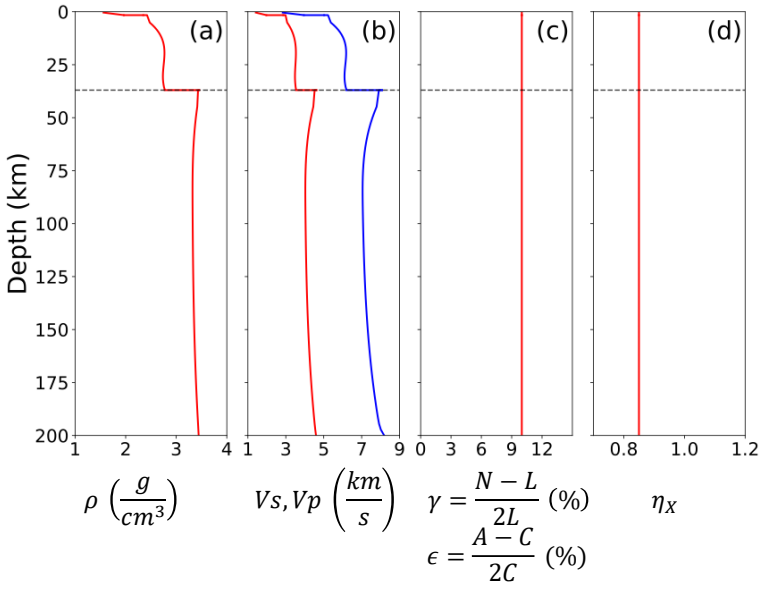

Figure 4. Isotropic and VTI reference models used to illustrate representative polarization quantities. (a) Density and (b) V_S (red) and V_P (blue) in the isotropic reference model. (c) S-wave and P-wave radial anisotropy, $\gamma = (N - L)/(2L) = 10\%$ and $\epsilon = (A - C)/(2C) = 10\%$, respectively; the two profiles coincide. (d) The ellipticity parameter, $\eta_X = 4L/(A + C - 2F) = 0.85$, in the VTI reference model. Here A, C, N, L, and F are the Love moduli, and γ and ϵ are the corresponding Thomsen parameters for S-wave and P-wave radial anisotropy (Thomsen, 1986). The VTI model is constructed from the isotropic model by introducing non-elliptical radial anisotropy from the surface to 200 km depth. The dashed horizontal line marks the Moho.

azimuthal anisotropy. The isotropic reference model supplies the eigenfunctions U, V, and W (Figures 4a,b). A VTI model is constructed from the isotropic model by introducing non-elliptical radial anisotropy from the surface to 200 km depth (Figures 4c,d). A family of TTI models is then generated by tilting the mantle symmetry axis over a range of dip angles θ while retaining a VTI crust.

The surface ratio W/U is negative under the adopted eigenfunction convention and has an absolute value of about 1.2–1.6 over much of the period range shown (Figure 5a). Because $|W/U| > 1$ in this model, a given $|\Gamma|$ in the X-dominant regime produces a larger quasi-Rayleigh than quasi-Love polarization angle in the Z–T plane. For example, $|\Gamma| = 0.15$ and $|W/U| = 1.5$ correspond to polarization angles of approximately 13° and 6°, respectively.

The relative importance of X and E varies strongly with symmetry-axis dip angle θ in a TTI medium (Figure 5b). Both vanish in the VTI limit, where Rayleigh and Love waves retain their reference polarizations. For the illustrated TTI family, X becomes large at intermediate dip angles and vanishes again in the HTI limit, whereas E becomes relatively important as the symmetry axis ap-

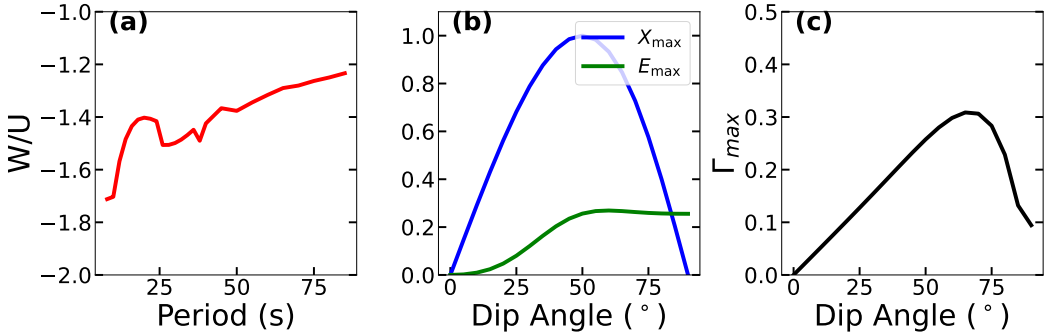

Figure 5. Representative quantities governing surface-wave polarization and their dependence on dip angle. (a) Ratio of the surface eigenfunctions W/U in the isotropic reference model, which relates the signed polarization parameter Γ to the quasi-Rayleigh and quasi-Love polarization angles through equations (7) and (8). (b) Maximum absolute values over propagation azimuth, $|X|_{\max}$ and $|E|_{\max}$, for a set of TTI models generated by tilting the mantle symmetry axis of the VTI reference model through a range of dip angles θ, while retaining the same VTI crust. Both quantities are normalized by the largest value of $|X|_{\max}$ among these models. (c) Corresponding maximum mixing magnitude, $\widetilde{\Gamma}_{\max} = |\chi|_{\max}$, where the maximum is again taken over propagation azimuth. Panels (b) and (c) are computed at a period of 40 s. For these models, X dominates over most intermediate dip angles, whereas E becomes relatively important as the symmetry axis approaches horizontal.

proaches horizontal. The strongest X-type coupling therefore occurs away from both VTI and HTI. The corresponding mixing magnitude $\widetilde{\Gamma} = |\chi|$ is largest at intermediate dip angles but remains nonzero near HTI through the E contribution (Figure 5c).

The relative importance of X and E depends on the elastic tensor and is not determined by dip angle alone. Our emphasis on the X-dominant regime is motivated by Alaska observations and models. The observed Rayleigh- and Love-wave 2ψ and 4ψ phase-speed variations across Alaska (X. Liu, C. Liu & Ritzwoller 2025) constrain elastic-tensor models that most commonly place the Alaska structure in the X-dominant regime (X. Liu, C. Liu & Ritzwoller 2026). Our numerical benchmarks and observational analysis therefore emphasize the X-dominant equations, while the E-dominant theory is retained as an important limiting case, particularly for nearly HTI media.

2.6 Recoverability of polarization parameters

A valid forward theory does not guarantee that the signed polarization parameters at the two stations can be estimated reliably. The parameters Γ_{ref} and Γ_{fld} are local quantities determined by the elastic tensor at the reference and field stations, respectively. In general they are frequency dependent, but within each narrow frequency band we assume that their frequency dependence, together with that of the relevant reference eigenfunction ratios, is negligible. In the X-dominant regime, the positive-lag

equations (14) and (15) can therefore be written at each time sample as

$$\begin{bmatrix} TZ^{+}(W_{\mathrm{fld}}/U_{\mathrm{fld}}) \\ ZT^{+}(U_{\mathrm{fld}}/W_{\mathrm{fld}}) \end{bmatrix} = \begin{bmatrix} -TT^{+} & ZZ^{+} \\ ZZ^{+} & -TT^{+} \end{bmatrix} \begin{bmatrix} \Gamma_{\mathrm{fld}} \\ \Gamma_{\mathrm{ref}} \end{bmatrix}. \tag{22}$$

At negative lag, equations (16) and (17) can be written in the same form, with the matrix formed from the TT^{-} and ZZ^{-} carrier-wave cross-correlations,

$$\begin{bmatrix} TZ^{-}(U_{\mathrm{ref}}/W_{\mathrm{ref}}) \\ ZT^{-}(W_{\mathrm{ref}}/U_{\mathrm{ref}}) \end{bmatrix} = \begin{bmatrix} -TT^{-} & ZZ^{-} \\ ZZ^{-} & -TT^{-} \end{bmatrix} \begin{bmatrix} \Gamma_{\mathrm{fld}} \\ \Gamma_{\mathrm{ref}} \end{bmatrix}. \tag{23}$$

Defining the matrix appearing on the right-hand side of equations (22) and (23) as $\mathbf{A}^{\pm}$, its determinant for either lag is

$$\det \mathbf{A}^{\pm} = (\mathbf{TT}^{\pm})^{\mathbf{2}} - (\mathbf{ZZ}^{\pm})^{\mathbf{2}}. \tag{24}$$

Thus, at an individual time sample, the two polarization parameters cannot be separated when $TT^{\pm} = \pm ZZ^{\pm}$. This pointwise singularity illustrates the more general conditioning problem. In practice, Γ_{ref} and Γ_{fld} are estimated from all samples in a finite signal window, so their recoverability depends on the independence of the $TT^{\pm}$ and $ZZ^{\pm}$ carrier-wave cross-correlations over that window. The inference becomes poorly conditioned when these carrier waveforms are strongly correlated or anti-correlated and have comparable amplitudes.

When measurements are available at both correlation lags, the two systems in equations (22) and (23) are fit jointly. Combining the two lags can improve conditioning when they provide complementary carrier-waveform information, although strong similarity between the TT and ZZ carrier waveforms at both lags can still produce a poorly conditioned inference.

3 NUMERICAL BENCHMARKS

We use three numerical benchmarks to test two distinct issues: whether the two-mode adiabatic theory predicts the polarization-sensitive waveforms when the true local polarization parameters are known, and whether those parameters can then be recovered from the waveforms. The three models progressively challenge adiabatic propagation, allowing limitations of the forward theory to be distinguished from limitations caused by inference conditioning. This distinction is important because inaccurate estimates of the polarization parameters can arise either from deficiencies in the forward theory or from poor conditioning of an otherwise accurate inference problem.

We consider three synthetic models: a horizontally homogeneous model and two models in which the anisotropic structure varies along the propagation path. All three use the isotropic reference structure shown in Figures 4a,b, with anisotropy introduced from the surface to 200 km depth. The homo-

geneous model has $M_s/A = -3\%$ everywhere and all other anisotropy parameters zero. In the slowly varying model, M_s/A increases from -3% at the reference station in steps of 0.5 percentage points every 200 km, whereas in the rapidly varying model it increases in steps of 1 percentage point every 100 km. Thus, in both heterogeneous models, the magnitude of M_s/A first decreases to zero and then increases after M_s/A changes sign. Because M_s contributes only to X, $E = 0$ in all three experiments, so the benchmarks test the X-dominant relations in equations (14) and (15). The surface-wave wavelengths are approximately 70 and 200 km at periods of 20 and 50 s, respectively. Thus we expect the homogeneous model to satisfy the adiabatic approximation at both periods, the slowly varying model to provide a stronger test at 50 s than at 20 s, and the rapidly varying model to challenge the adiabatic approximation most strongly at 50 s. These expectations are qualitative because the amplitude of each structural change also affects mode conversion.

Synthetic Green tensors are computed with SPECFEM (Komatitsch & Tromp, 1999). Point forces with a half-duration of 5 s are applied sequentially in the R, T, and Z directions at the reference station $(0, 0, 0)$, and displacement is recorded at field stations along the positive x direction, corresponding to $\psi = 0^\circ$ in equation (A.30). The computational grid has a spacing of 5 km and extends from -1000 to 3000 km in x, from -500 to 500 km in y, and to 200 km depth. The calculations represent positive-lag propagation only. We use each Green-tensor element as the corresponding positive-lag cross-correlation component, as in equation (A.34), and process the synthetic tensor using the same narrow-band, frequency-domain empirical source-group normalization applied to the observations (Section 4.2).

To test the forward theory directly, we insert the known input values of Γ_{ref} and Γ_{fld} into equations (14) and (15) and compare the predicted TZ and ZT waveforms with the numerical Green-tensor components. Because the input polarization parameters are specified rather than estimated, this comparison is independent of inference conditioning. Disagreement can therefore reflect limitations of the two-mode adiabatic forward theory as well as inaccuracies introduced by the empirical source-group normalization applied to the synthetic cross-correlation tensor. Figure 6 shows representative comparisons at an inter-station distance of 1000 km and a period near 50 s.

We then estimate Γ_{ref} and Γ_{fld} jointly from the numerical TZ and ZT waveforms using the two-parameter grid-search formulation described in Section 4.4 and applied to the observations. Each station pair is treated independently. Because the numerical calculations contain only positive-lag propagation, this inference uses fewer waveform constraints than an observational station pair for which both correlation lags are retained. We refer to this joint pairwise estimate as Stage 1. For the two heterogeneous models, we also perform a Stage 2 calculation in which Γ_{ref} is fixed to the mean of its Stage 1 estimates over inter-station distance and Γ_{fld} is re-estimated at each field station. Stage 2

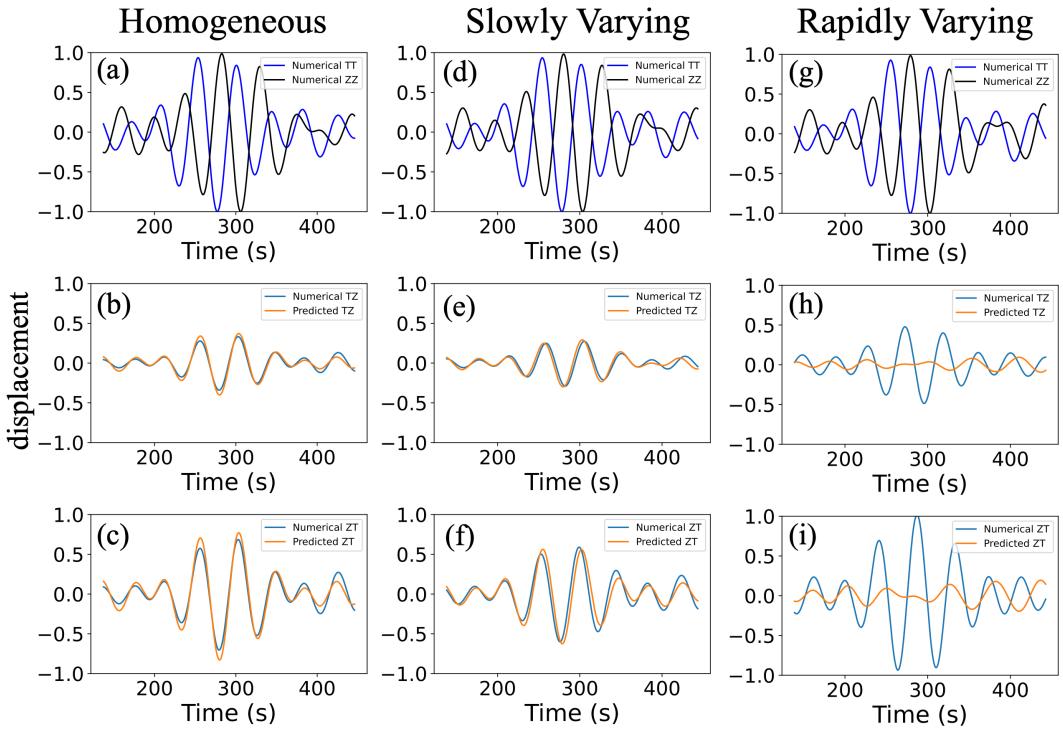

Figure 6. Example numerical waveforms providing a direct test of the two-mode adiabatic forward theory in the X-dominant regime ($E = 0$). The columns show results for the homogeneous (left), slowly varying (middle), and rapidly varying (right) anisotropic models. The top row shows the TT (blue) and ZZ (black) carrier waveforms. The middle and bottom rows compare the numerical TZ and ZT waveforms, respectively, with predictions from equations (14) and (15) computed using the known input polarization parameters. The propagation distance is 1000 km and the waveforms are filtered in a narrow band centered near 50 s. Agreement is close for the homogeneous model and remains good for the slowly varying model, but degrades substantially for the rapidly varying model. This comparison tests the forward theory independently of the parameter-estimation procedure.

is designed to diagnose conditioning problems and separate them from breakdown of the adiabatic approximation. Substantial improvement after constraining Γ_{ref} indicates that conditioning and trade-off between the two polarization parameters contribute importantly to the Stage 1 errors. Persistent disagreement instead points to limitations of the forward theory or to bias in the imposed reference-station constraint. These results are presented in Figures 7, 8, and 10.

3.1 Homogeneous medium

The homogeneous benchmark provides the simplest test of the theory because the polarization parameters are spatially constant, $\Gamma_{\mathrm{ref}} = \Gamma_{\mathrm{fld}} \approx 0.33$. At 50 s period, the TZ and ZT waveforms predicted by equations (14) and (15) using the known input polarization parameters agree closely with the nu-

merical synthetics (Figures 6b,c), showing that the forward theory performs well under homogeneous conditions. The joint recovery of the polarization parameters at 20 and 50 s, shown in Figure 7, provides a more stringent test of the inference.

The recovered values of Γ_{ref} and Γ_{fld} are nearly equal at most distances, as expected from the equality of the input polarization parameters, although their common value is generally underestimated. At 20 s period the mean bias is approximately 15%, which is also reflected in the waveform prediction in Figures 6b,c. Possible contributions include overtone energy in the numerical synthetics and the use of the reference-model eigenfunctions W and U rather than those of the perturbed medium.

The estimates also exhibit distance-dependent excursions, particularly at 50 s, where similarity between the TT and ZZ carrier waveforms reduces the information available to separate the two polarization parameters (Section 2.6). Stable recovery emerges only after propagation of approximately one to two wavelengths in this benchmark. At shorter distances, the carrier waveforms have acquired little relative phase, which contributes to poor conditioning, and the wavefield may not yet satisfy the far-field approximation underlying the theoretical Green tensor.

The homogeneous benchmark therefore establishes the baseline for the heterogeneous experiments. The remaining discrepancies in the recovered polarization parameters consist principally of a modest systematic bias, conditioning-related variations with distance, and a near-source limitation associated with conditioning and the far-field approximation. None reflects breakdown of the adiabatic approximation, because the medium is horizontally homogeneous.

3.2 Slowly varying medium

The benchmark based on the slowly varying medium provides the first test in which lateral variation can challenge the adiabatic approximation, while also testing the conditioning of the two-parameter inference. At periods of both 20 s and 50 s, the predicted TZ and ZT waveforms remain close to the numerical synthetics, although the agreement is slightly poorer than in the homogeneous model at 50 s (Figures 6e,f). Stage 1 recovery of the polarization parameters at 20 s follows the imposed decrease in Γ_{fld} reasonably well, while Γ_{ref} remains near its input value apart from the modest bias and near-source behavior seen in the homogeneous benchmark (Figures 8a,b). At 50 s, however, both estimates develop large, opposing excursions despite the comparatively small deterioration of the forward waveforms (Figures 8c,d). These variations are much stronger than the degradation of the forward waveform predictions, indicating that an additional limitation affects the parameter inference.

The dominant additional effect is a trade-off between Γ_{ref} and Γ_{fld}. Figure 9 illustrates its origin. Where the TT and ZZ carrier-wave cross-correlations are strongly correlated or anti-correlated,

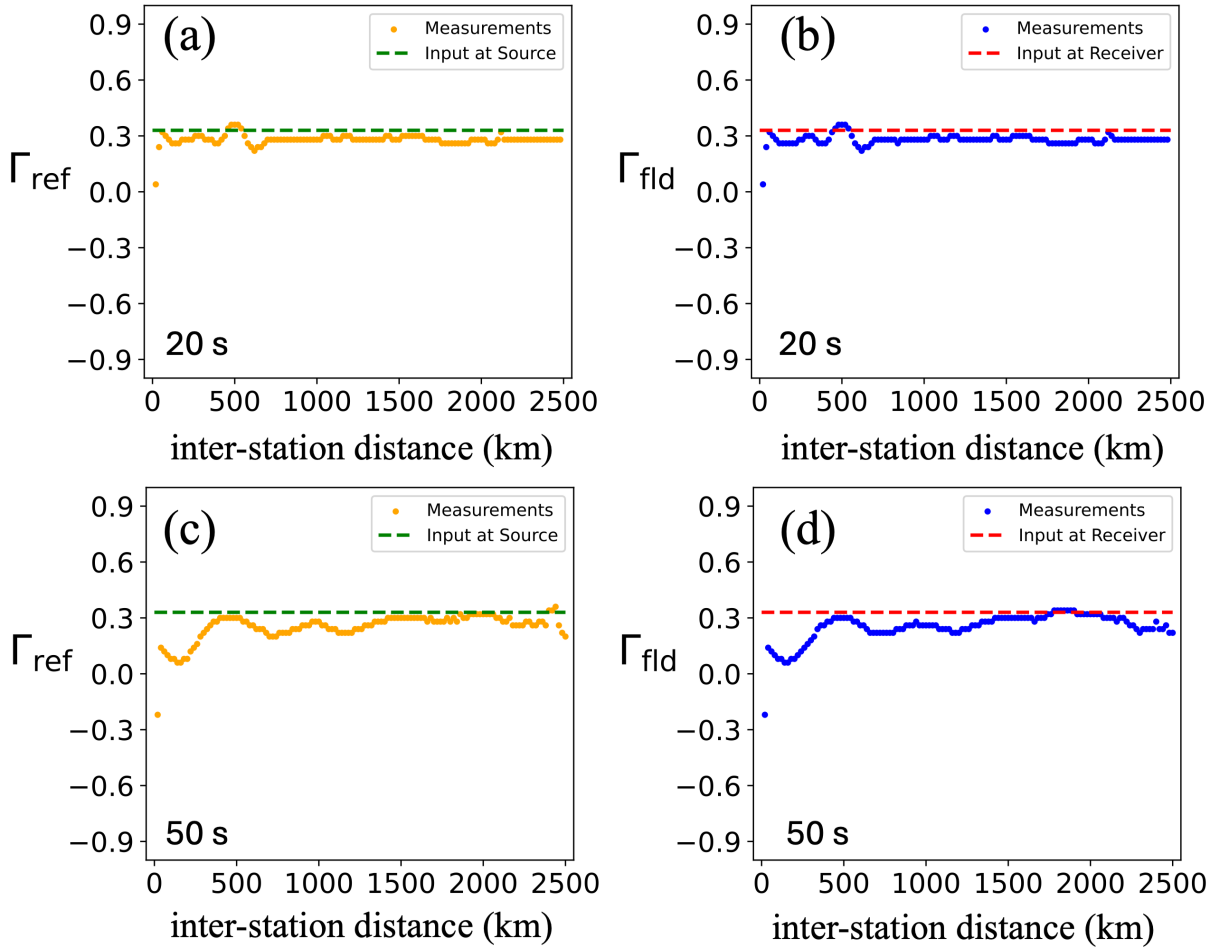

Figure 7. Polarization-parameter recovery in the homogeneous numerical benchmark in the X-dominant regime ($E = 0$). Joint measurements of Γ_{ref} and Γ_{fld} are shown as functions of source–receiver distance and compared with the spatially constant input value $\Gamma_{\mathrm{input}} = 0.33$. In these numerical experiments, the source and receiver locations correspond, respectively, to the reference- and field-station locations used for the observational analysis. Results are shown at periods of 20 and 50 s. The two endpoint measurements are generally similar and recover the input value approximately, but exhibit a modest systematic bias and distance-dependent excursions, particularly at 50 s. Because the medium is horizontally homogeneous, these discrepancies do not reflect breakdown of the adiabatic approximation.

they provide little independent information for separating the two polarization parameters (this is the case that the determinant is close to zero (equation (24))); where their correlation is smaller, the inference is better conditioned. The parameter-space misfit shows the same contrast. At 500 km, the misfit minimum is compact (Figure 9b), whereas at 850 km it forms an elongated valley along which compensating changes in Γ_{ref} and Γ_{fld} produce nearly the same waveform fit (Figure 9c).

The Stage 2 calculations provide a diagnostic test of this interpretation. At 20 s, fixing Γ_{ref} to its Stage 1 mean of 0.29 produces only a modest improvement in the recovery of Γ_{fld}. At 50 s, fixing Γ_{ref}

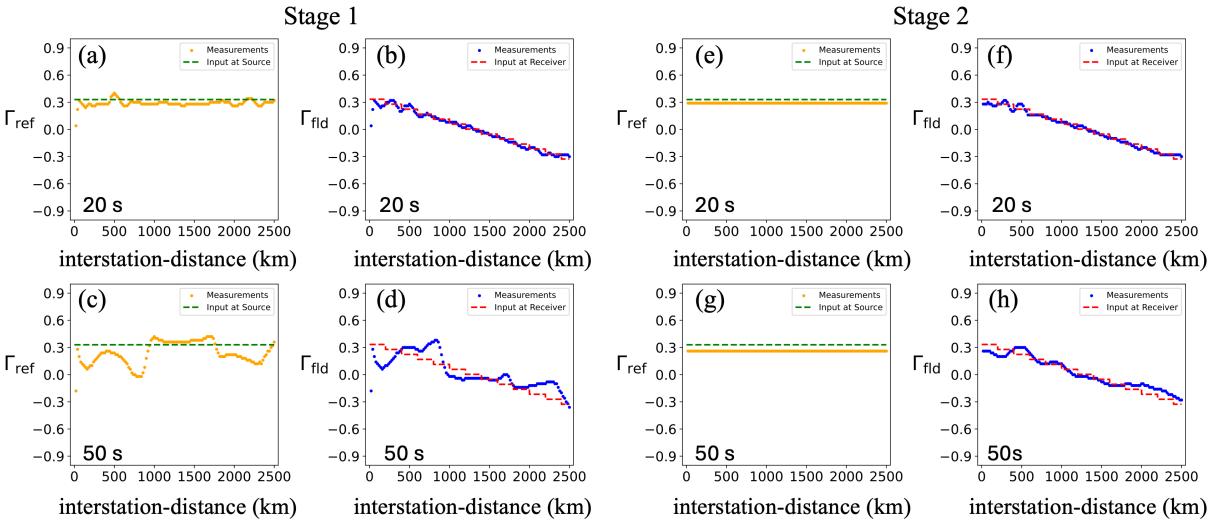

Figure 8. Polarization-parameter recovery in the slowly varying numerical benchmark in the X-dominant regime ($E = 0$). The input reference-station parameter is $\Gamma_{\mathrm{ref}} = 0.33$, while the input field-station parameter Γ_{fld} decreases in a stair-step pattern, changing every 200 km. Results are shown at periods of 20 and 50 s. (a)–(d) Stage 1 estimates, in which Γ_{ref} and Γ_{fld} are estimated jointly for each reference–field pair. (e)–(h) Stage 2 results, in which Γ_{ref} is fixed to the mean of its Stage 1 estimates over inter-station distance—0.29 at 20 s and 0.26 at 50 s—and Γ_{fld} is re-estimated at each field station. Recovery is comparatively stable at 20 s. At 50 s, the large Stage 1 excursions are substantially reduced in Stage 2, indicating that conditioning and trade-off between the endpoint parameters account for much of the Stage 1 variability.

to 0.26 substantially reduces the large distance-dependent excursions in Γ_{fld} (Figure 8). The substantial improvement at 50 s demonstrates that much of the large Stage 1 variability results from conditioning and the associated trade-off between the two polarization parameters rather than from failure of the forward theory.

The period dependence is consistent with the expected progression toward the limits of adiabatic propagation. At 20 s, the 200-km spacing between structural changes substantially exceeds the approximately 70-km wavelength, and both the forward theory and parameter recovery perform well. At 50 s, the spacing is comparable to the approximately 200-km wavelength and the forward-waveform agreement becomes slightly poorer. The much larger deterioration in the Stage 1 parameter estimates, however, is primarily a conditioning effect, as demonstrated by the substantial improvement in Stage 2.

3.3 Rapidly varying medium

The benchmark based on the rapidly varying medium provides the strongest test of the adiabatic approximation. Based on the operational adiabatic condition (equation 1), we expect propagation to remain approximately adiabatic at 20 s but to become nonadiabatic at 50 s. The conditioning of the

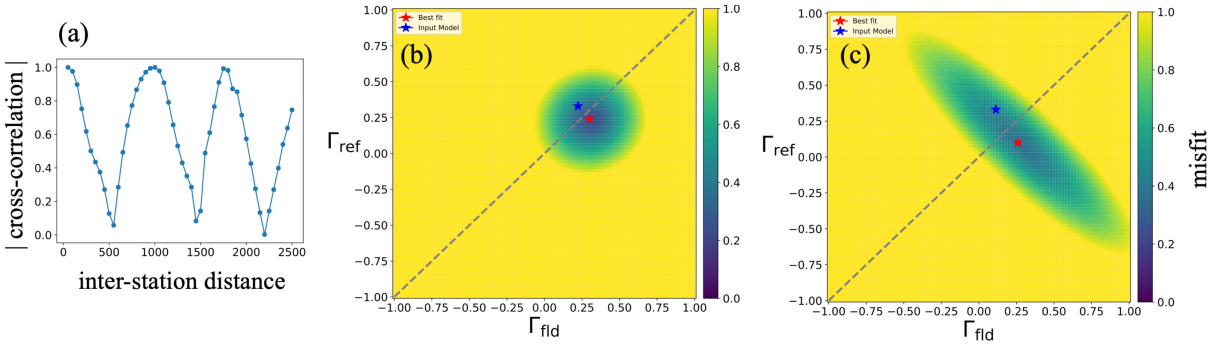

Figure 9. Illustration of how similarity between the TT and ZZ carrier waveforms controls conditioning of the two-parameter polarization inference in the slowly varying model at 50 s. (a) Absolute value of the waveform correlation coefficient between TT and ZZ as a function of inter-station distance. High correlations occur near 0, 950, and 1850 km, whereas much lower correlations occur near 550 and 1500 km. (b) Parameter-space misfit between the numerical TZ and ZT waveforms and their predictions from equations (14) and (15) at 500 km, where the inference is well conditioned. (c) Corresponding misfit at 850 km, where the inference is poorly conditioned. Blue and red stars denote the input and best-fitting parameter pairs, respectively, and the dashed line marks $\Gamma_{\mathrm{ref}} = \Gamma_{\mathrm{fld}}$. The compact minimum in (b) and elongated valley in (c) illustrate how carrier-waveform similarity produces a trade-off between the endpoint parameter estimates.

two-parameter inference remains a separate issue that must be distinguished from breakdown of the forward theory.

At 20 s, the Stage 1 inference captures the overall decrease in Γ_{fld}, while Γ_{ref} remains moderately close to its input value (Figures 10a,b). Recovery is poorer than in the slowly varying model, with stronger distance-dependent excursions and near-source instability, but the forward theory remains sufficiently accurate to act as the basis for inference. At 50 s, by contrast, neither polarization parameter is recovered reliably (Figures 10c,d).

The direct forward-waveform comparison at 50 s clearly shows how breakdown of the adiabatic approximation diminishes waveform fit. The TZ and ZT waveforms predicted using the known input values of Γ_{ref} and Γ_{fld} are substantially degraded relative to the numerical synthetics (Figures 6h,i). Because no inferred polarization parameters enter this comparison, the disagreement is independent of inference conditioning.

The Stage 2 calculations help separate this failure of the forward theory from conditioning effects. At 20 s, fixing Γ_{ref} to the mean of its Stage 1 estimates, 0.45, produces a modest improvement in the recovery of Γ_{fld} (Figure 10e). At 50 s, the Stage 1 mean gives an erroneous reference-station value, $\Gamma_{\mathrm{ref}} = -0.12$. Fixing Γ_{ref} to this value reduces some of the trade-off between the two polarization parameters, but Γ_{fld} remains poorly recovered over broad ranges of distance (Figure 10f). Recovery also remains poor when Γ_{ref} is fixed to its true input value. Thus, although conditioning contributes

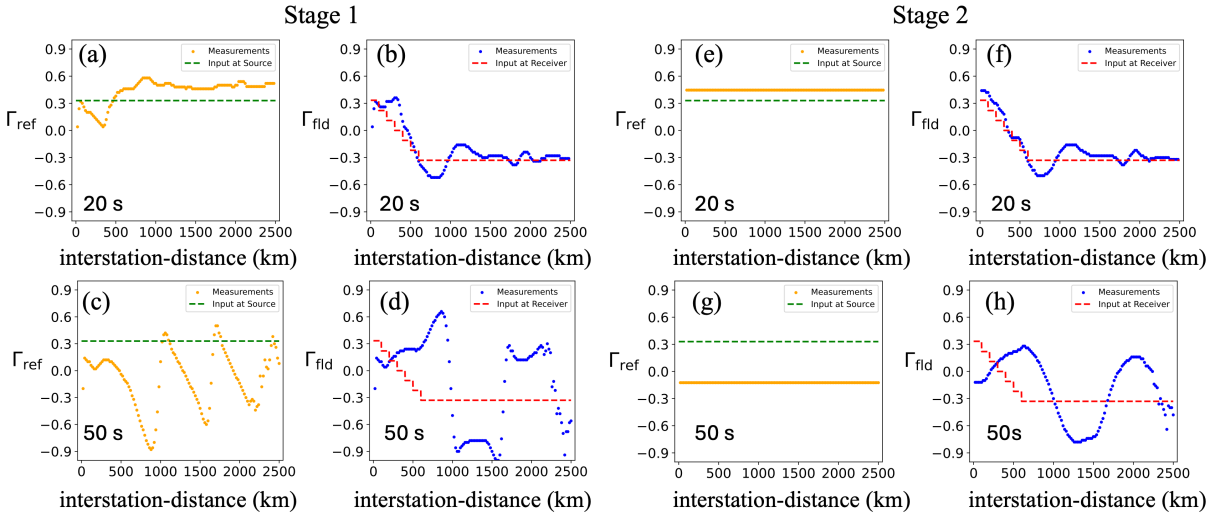

Figure 10. Similar to Figure 8, but for the rapidly varying model, in which Γ_{fld} decreases through larger stair-step changes separated by 100 km. In Stage 2, Γ_{ref} is fixed to the mean of its Stage 1 estimates over inter-station distance: 0.45 at 20 s and -0.12 at 50 s. At 50 s, parameter recovery remains poor after the Stage 2 constraint. Together with the degraded forward-waveform predictions in Figure 6, this indicates that loss of accuracy of the adiabatic forward theory has become a major limitation.

to the Stage 1 instability at 50 s, reducing the trade-off does not restore accurate parameter recovery. Together with the degraded forward-waveform predictions, this indicates that violation of the adiabatic approximation dominates over inference conditioning as the limitation on parameter recovery in this benchmark at 50 s.

The period dependence is consistent with the expected breakdown of adiabatic propagation. At 20 s, the 100-km spacing between structural changes modestly exceeds the approximately 70-km wavelength and the forward theory remains reasonably accurate. At 50 s, the same spacing is substantially smaller than the approximately 200-km wavelength and the forward-waveform predictions deteriorate. For the structural amplitudes tested here, this behavior is consistent with nonadiabatic mode conversion becoming important.

3.4 Synthesis of benchmark results

The three benchmark tests identify challenges to polarization-parameter inference caused both by poor conditioning and by limitations of the forward theory. In the homogeneous model, the adiabatic theory accurately predicts the polarization-sensitive waveforms, and the remaining errors in Γ_{ref} and Γ_{fld} arise from modest approximation bias, conditioning, and near-source limitations. In the slowly varying model, the forward theory remains reasonably accurate at both periods, but poor conditioning produces strong trade-offs between the two polarization parameters at 50 s that are substantially reduced by the

Stage 2 constraint. In the rapidly varying model, conditioning still contributes to parameter instability, but at 50 s the forward-waveform predictions themselves deteriorate and constraining the parameter trade-off does not restore accurate recovery. This progression is consistent with the operational adiabatic condition in equation (1): the forward theory performs well when the structural scale exceeds the wavelength, is increasingly challenged as the two become comparable, and breaks down in the rapidly varying 50-s benchmark when the structural scale is appreciably shorter than the wavelength. Thus the numerical experiments show separately how forward-theory limitations and inference conditioning can control the recovery and local interpretation of the polarization parameters.

4 AMBIENT NOISE DATA PROCESSING AND POLARIZATION ESTIMATION

Previous studies of ambient-noise amplitudes have primarily focused on the recovery and interpretation of absolute amplitudes, with applications to seismic attenuation (e.g. Prieto et al., 2009; Cupillard & Capdeville 2010; Lin et al., 2011; Tsai 2011; Bowden et al., 2017; Zhou et al., 2020; Peng & Li 2024) and ground-motion prediction (e.g. Prieto & Beroza 2008; Denollet al., 2013, 2014). In this section, we describe how ambient noise cross-correlations are processed to produce an observational cross-correlation tensor that can be compared with the theoretical polarization relations and used to estimate the polarization parameters. Because polarization information is carried by the relative amplitudes among tensor components, the processing must preserve those amplitude relationships. Independent normalization of the three components can alter them and bias the inferred polarization (e.g., Ritzwoller & Feng, 2019). Conventional cross-correlation processing also leaves source-group-dependent amplitude factors that differ among tensor components and between correlation lags. If these factors are not accounted for, they can distort the relative amplitudes of the carrier and polarization-sensitive components and thereby bias the inferred polarization parameters. An additional normalization is therefore required before the theoretical polarization relations can be applied.

Our procedure consists of three processing phases followed by data selection, quality control, and joint estimation of the polarization parameters and their uncertainties. Phase 1 processes the continuous three-component records before cross-correlation, largely following Lin et al. (2014), while preserving their relative amplitudes. Phase 2 constructs the nine-component cross-correlation tensor and rotates it into the fixed R, T, Z station-pair coordinates following Lin et al. (2008). Phase 3 is the additional step required to account for the source-group-dependent amplitude factors that remain after Phase 2. It applies the empirical source-group normalization introduced here to approximate the theoretical normalization derived in Appendix A and summarized in Section 2.3. The resulting normalized cross-correlations are then subjected to quality control and used to estimate Γ_{ref} and Γ_{fld} using the procedure we describe here.

4.1 Ambient noise data preparation and cross-correlation

In Phase 1, the continuous north, east, and vertical (N, E, and Z) records are processed while preserving their relative amplitudes. For each station and component, the mean, trend, and instrument response are removed from each daily time series. Temporal normalization follows Bensen et al. (2007), with an important modification for three-component polarization analysis. A 128-s running absolute mean is computed separately for each component, and at each station and time the maximum of the three values defines a single normalization factor that is applied to all three components. Spectral whitening likewise uses a common frequency-dependent normalization: at each frequency, the complex spectrum of each component is divided by the average of the three smoothed amplitude spectra. Thus, neither temporal normalization nor spectral whitening introduces component-dependent amplitude scaling.

In Phase 2, the cross-correlations are constructed for each station pair following Lin et al. (2008), using the fixed reference- and field-station notation introduced in Section 2. For any component pair X, Y, we define the cross-correlation as $C^{XY}(\tau) = \langle X_{\mathrm{ref}}(t)\, Y_{\mathrm{fld}}(t+\tau)\rangle_t$, where $\langle\cdot\rangle_t$ denotes averaging over time. In the component label XY, the first letter denotes the component at the reference station and the second denotes the component at the field station. The horizontal components are rotated into the same fixed R, T, Z coordinate system used in Section 2, with R directed from the reference station toward the field station and the transverse direction defined by $\hat{\mathbf{T}} = \hat{\mathbf{R}} \times \hat{\mathbf{Z}}$, where $\hat{\mathbf{Z}}$ is positive upward. The same coordinates are retained at both correlation lags.

With this cross-correlation convention, for $\tau > 0$ the field-station signal occurs later than the reference-station signal, so positive lag corresponds to propagation from the reference station to the field station ($\mathrm{ref} \rightarrow \mathrm{fld}$). At negative lag, propagation is $\mathrm{fld} \rightarrow \mathrm{ref}$. We retain the positive- and negative-lag cross-correlations separately rather than averaging them to form the commonly used symmetric component because the distribution and strength of the ambient noise sources contributing to the correlation may differ between the two propagation directions.

Observational examples are drawn from a narrow-azimuth station selection with AK-CNP on the Kenai Peninsula as the reference station and field stations lying between 20° and 40° north of east. Figure 11 shows the 29 station pairs from this selection that remain after Phase 3 processing and completion of the quality-control procedure. The TT, ZZ, TZ, and ZT cross-correlations that emerge from Phase 2 processing are shown in Figure 12. Because all tensor components are processed identically through Phase 2, their relative amplitudes are directly comparable. The TT and ZZ carrier waveforms have well-defined surface-wave arrivals at both lags, while the lower-amplitude TZ and ZT cross-components contain coherent arrivals with systematic moveout on many station pairs.

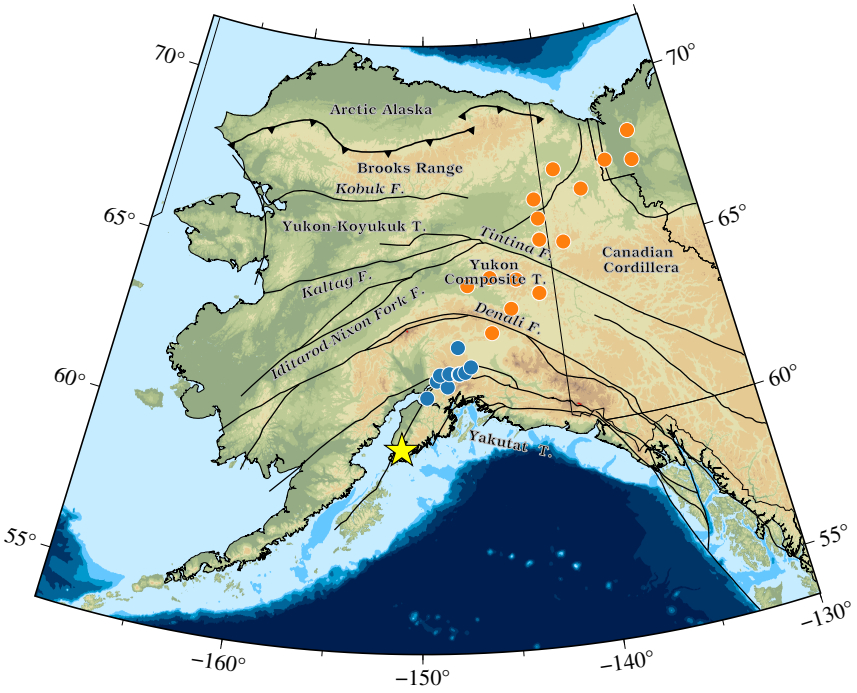

Figure 11. Station geometry for the narrow-azimuth Alaska subset used to illustrate the data processing, quality control, and distance-dependent polarization estimates. The yellow star marks the reference station AK-CNP on the Kenai Peninsula, and the blue and red circles mark the 29 field stations retained from the narrow-azimuth selection after Phase 3 processing and completion of the quality-control procedure described in Section 4.3. The field stations have azimuths between 20° and 40° north of east from AK-CNP. Blue stations are less than 450 km from the reference station and red stations are at distances greater than or equal to 450 km; this division approximately corresponds to crossing the Denali Fault.

4.2 Empirical source-group normalization

Phases 1 and 2 preserve the relative amplitudes among tensor components, but the resulting cross-correlation tensor still contains generally unknown source-group-dependent amplitude factors associated with the distribution and strength of the ambient noise sources. The theoretical source-group normalization introduced in Section 2.3 and derived in Appendix A removes these factors exactly within the assumptions of the theory. Phase 3 empirically approximates this normalization within each narrow frequency band and correlation lag.

For each period band $i = [T_{\min,i}, T_{\max,i}]$, the positive and negative lags are processed independently in the frequency domain over the corresponding frequency interval $[1/T_{\max,i}, 1/T_{\min,i}]$. The observed TT and ZZ carrier amplitude spectra are used as frequency-dependent proxies for the theoretical normalization factors of the T- and Z-source groups. To prevent division by very small carrier

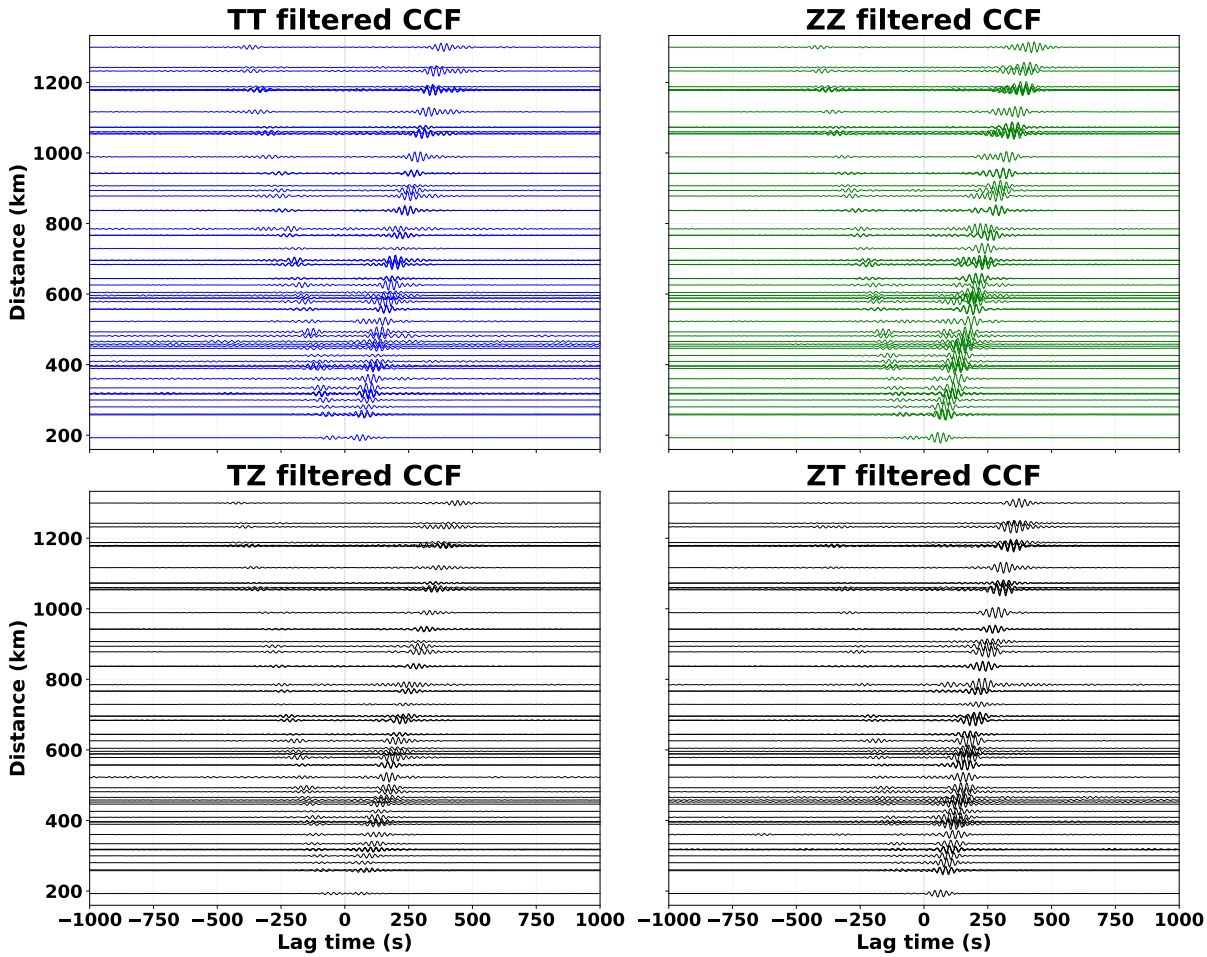

Figure 12. Phase 2 cross-correlation (CCF) record sections showing the carrier and polarization-sensitive components before Phase 3 processing. The TT, ZZ, TZ, and ZT components are shown for station pairs in the narrow-azimuth selection, with field stations lying between 20° and 40° north of east of the reference station AK-CNP, and are filtered in the 20–30 s period band. These records precede the Phase 3 empirical source-group normalization and subsequent quality control. Although the TZ and ZT amplitudes are smaller than those of the carrier components, they contain coherent arrivals with systematic moveout. The Phase 3-normalized records retained after quality control are shown in Figures 14 and 15.

amplitudes, each reference spectrum is stabilized by imposing a lower bound equal to 10% of its median amplitude within the frequency band.

At positive lag, the reference station serves as the source location in the Green-tensor interpretation. Because a cross-correlation component XY is indexed by the fixed station components, with X at the reference station and Y at the field station, whereas the Green tensor is ordered as response direction followed by force direction, C^{XY} corresponds to G_{YX} at positive lag. The first cross-correlation index therefore identifies the source direction. Thus, TT^+ and TZ^+ are normalized using the spectrally stabilized TT^+ carrier amplitude spectrum, whereas ZZ^+ and ZT^+ are normalized using the

corresponding ZZ^+ carrier amplitude spectrum. At negative lag, the source and receiver roles reverse, so the second cross-correlation index identifies the source direction. Consequently, TT^- and ZT^- use the TT^- carrier amplitude spectrum, whereas ZZ^- and TZ^- use the ZZ^- carrier amplitude spectrum. Each polarization-sensitive cross-component is therefore normalized by the same frequency-dependent reference spectrum as the carrier component in its source group rather than being normalized independently. This procedure approximately removes the source-group-dependent amplitudes while retaining the spectral phase and the relative component amplitudes that carry the polarization information.

We denote the empirically normalized tensor in frequency band i by $\overline{\boldsymbol{C}}_i^{\pm}(\omega)$, where $+$ and $-$ denote the positive and negative correlation lags, respectively. In the theoretical development, the unnormalized carrier components contain the source-group factors $N_{X,\mathrm{ref}}(\omega)$ at positive lag and $N_{X,\mathrm{fld}}(\omega)$ at negative lag. For real data, the theoretical normalization factors are not known and must be approximated empirically. We therefore use the measured carrier amplitude spectra to estimate their magnitudes. The resulting $\overline{\boldsymbol{C}}^{\pm}$ is therefore an empirical approximation to $\widetilde{\boldsymbol{C}}^{\pm}$, the theoretically source-group-normalized tensor derived in Appendix A.

Figure 13 illustrates the Phase 3 normalization for a positive-lag observation in the 20–30 s period band. The TT^+ and TZ^+ spectra are normalized using the TT^+ carrier amplitude spectrum, whereas the ZZ^+ and ZT^+ spectra are normalized using the ZZ^+ carrier amplitude spectrum.

The empirically normalized narrow-band spectra are inverse Fourier transformed to the time domain. All four components on each lag are then divided by a single common scalar chosen so that the largest absolute amplitude of the TT or ZZ carrier waveform is unity. This final rescaling changes only the common amplitude scale and therefore preserves the relative amplitudes used to estimate the polarization parameters.

Figures 14 and 15 show the fully normalized carrier and polarization-sensitive waveforms retained for subsequent analysis. For compactness, we denote the observational components $\overline{C}_i^{TT,\pm}$, $\overline{C}_i^{ZZ,\pm}$, $\overline{C}_i^{TZ,\pm}$, and $\overline{C}_i^{ZT,\pm}$ by $\overline{TT}_i^{\pm}$, $\overline{ZZ}_i^{\pm}$, $\overline{TZ}_i^{\pm}$, and $\overline{ZT}_i^{\pm}$, respectively.

4.3 Data selection and quality control

Quality control is applied to the Phase 3-normalized data in two pre-fit steps, followed by a third post-fit criterion after preliminary polarization-parameter estimation. The procedure retains only station pairs with adequate carrier signals, usable $\overline{TZ}$ and $\overline{ZT}$ waveforms, sufficient propagation distance, and acceptable waveform fits. The criteria are pragmatic and empirical and are not intended as an optimal prescription for future ambient noise polarization studies.

For the 20–30 s narrow-azimuth example considered here, the initial geometrical selection con-

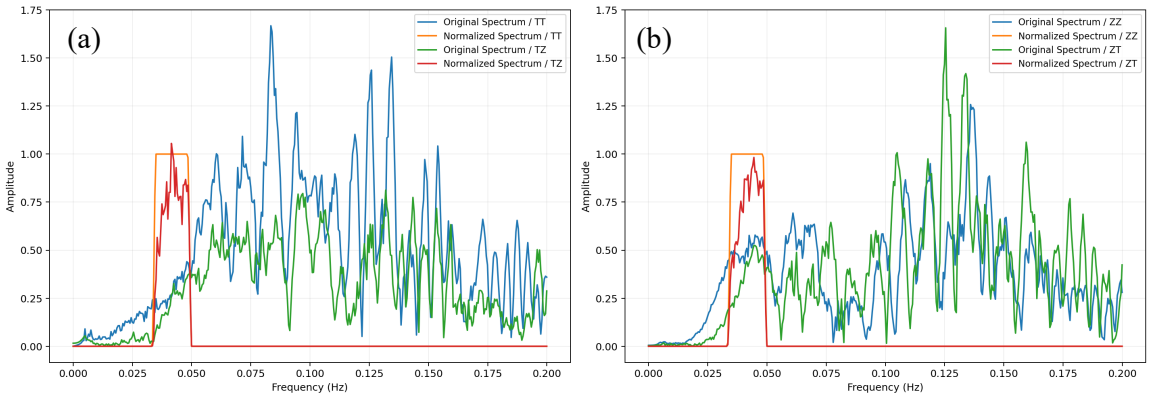

Figure 13. Illustration of the Phase 3 empirical source-group normalization in the frequency domain. The example is the positive lag of station pair AK-CNP–AK-SAW, separated by 300 km, in the 20–30 s period band. (a) Spectral amplitudes of TT^+ and TZ^+ before and after normalization by the spectrally stabilized TT^+ carrier amplitude spectrum. (b) Spectral amplitudes of ZZ^+ and ZT^+ before and after normalization by the spectrally stabilized ZZ^+ carrier amplitude spectrum.

tains 85 station pairs; 29 remain after the complete quality-control procedure and are shown in Figure 11.

In the first pre-fit step, we define signal, precursory-noise, and trailing-noise windows for the carrier waveforms. For each period band $[T_{\min}, T_{\max}]$, the central period is $T = (T_{\min} + T_{\max})/2$. The windows are determined separately for the positive and negative lags. For a given lag, let τ_{TT} and τ_{ZZ} denote the times of the maximum absolute amplitudes of $\overline{TT}$ and $\overline{ZZ}$, respectively. We define $t_1 = \min(\tau_{TT}, \tau_{ZZ}) - 2T$ and $t_2 = \max(\tau_{TT}, \tau_{ZZ}) + 2T$. The signal window is $[t_1, t_2]$, the precursory-noise window is $[0, t_1]$, and the trailing-noise window is $[t_2, t_2 + 500\ \mathrm{s}]$.

For each carrier component, the signal amplitude is the maximum absolute amplitude within the signal window, and the precursory and trailing noise levels are the mean absolute amplitudes within the corresponding noise windows. Let SNR_p and SNR_t denote the resulting precursory and trailing signal-to-noise ratios. For a given lag, if either $\overline{TT}$ or $\overline{ZZ}$ has $\mathrm{SNR}_p < 3$ or $\mathrm{SNR}_t < 5$, that lag is discarded for all four components. For these data, precursory noise is generally larger than trailing noise, so the precursory SNR is commonly the more restrictive criterion.

Motivated by the near-source limitations identified in the numerical benchmarks of Section 3.1,

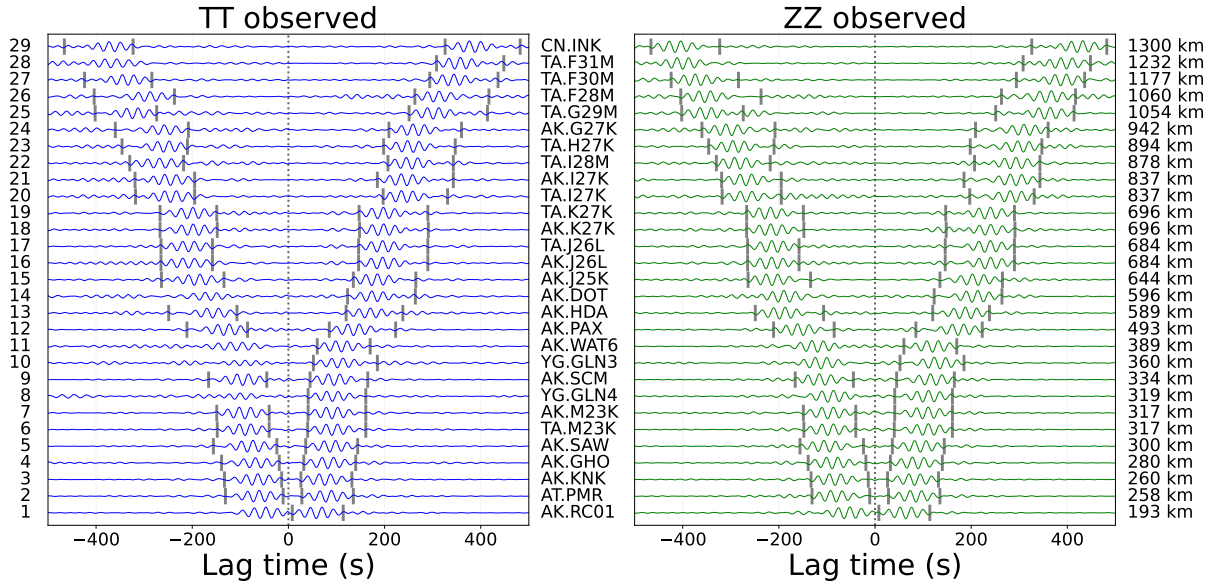

Figure 14. Phase 3-normalized TT and ZZ carrier waveforms retained after quality control for polarization analysis. The 29 station pairs are the final retained pairs from the narrow-azimuth selection; their geometry is shown in Figure 11. Grey vertical lines delimit the signal windows retained for analysis; absence of a window on one lag indicates that the corresponding lag was rejected by the carrier-waveform quality control.

we also require the inter-station distance to exceed approximately two wavelengths. For each period band, the wavelength is estimated as $\lambda = cT$, where c is the phase speed of the reference model. Together, the carrier-waveform and distance criteria reduce the example data set from 85 to 51 station pairs.

In the second pre-fit step, quality control is applied separately to each surviving $\overline{TZ}^{\pm}$ and $\overline{ZT}^{\pm}$ component-lag waveform. For each waveform, the signal amplitude S is defined as the maximum absolute amplitude within the signal window of its corresponding source-group carrier waveform: $\overline{TT}^{+}$ for $\overline{TZ}^{+}$, $\overline{ZZ}^{+}$ for $\overline{ZT}^{+}$, $\overline{ZZ}^{-}$ for $\overline{TZ}^{-}$, and $\overline{TT}^{-}$ for $\overline{ZT}^{-}$. The noise levels N_p and N_t are the mean absolute amplitudes of the polarization-sensitive waveform within its precursory and trailing noise windows. A component-lag waveform is retained only if both $N_p < S/5$ and $N_t < S/5$. The positive and negative lags of each cross-component are therefore accepted or rejected independently. A station pair is rejected if both lags are rejected for either $\overline{TZ}$ or $\overline{ZT}$, or if neither lag contains both an accepted $\overline{TZ}$ and an accepted $\overline{ZT}$ waveform. Consequently, every retained station pair contains at least one usable $\overline{TZ}$ waveform and at least one usable $\overline{ZT}$ waveform, with both components retained together at at least one lag. These criteria reduce the number of station pairs from 51 to 42.

Station pairs that survive the two pre-fit steps are passed to the polarization-parameter estimation procedure described in Section 4.4. The third quality-control step is applied after fitting and uses the

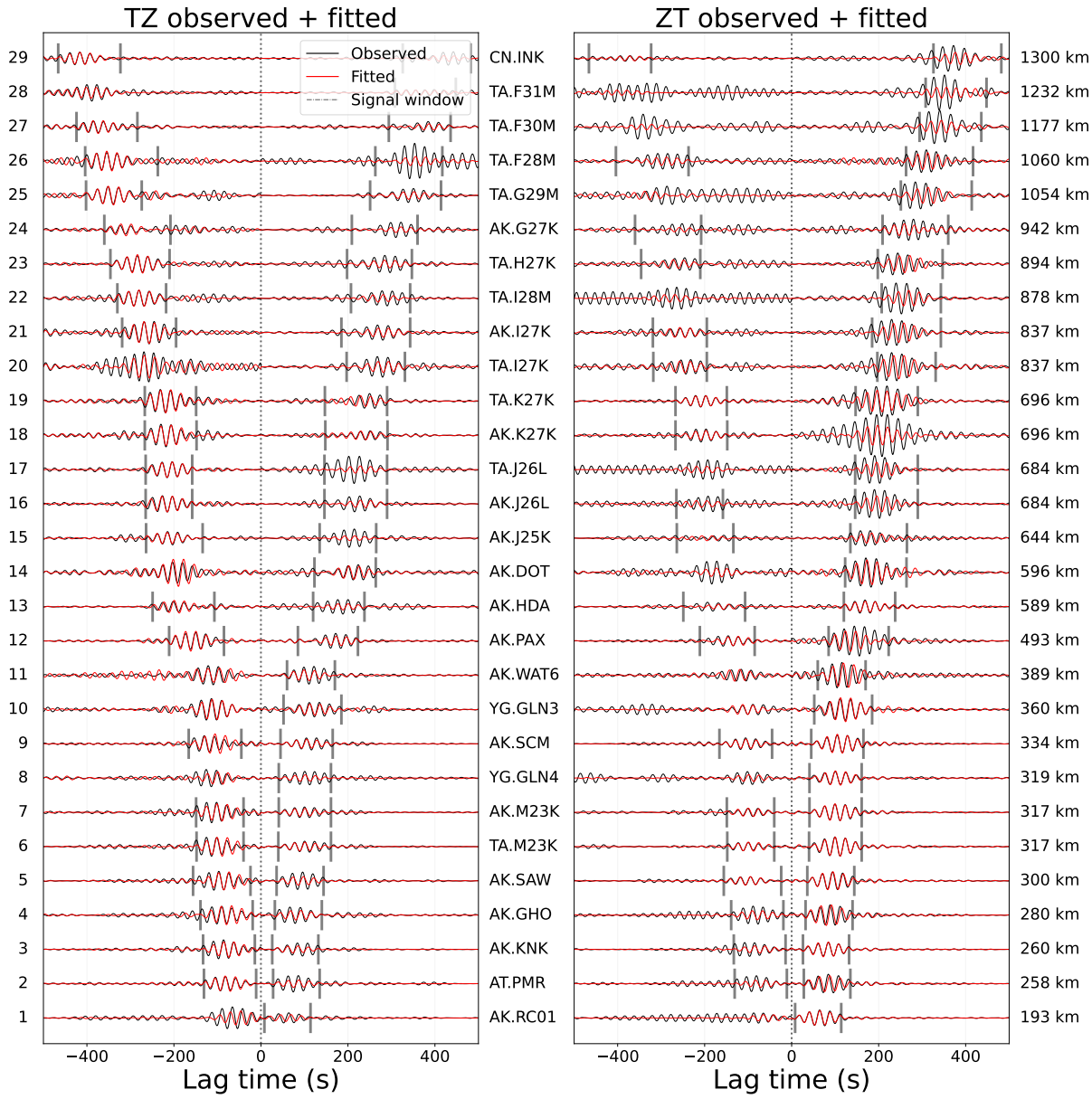

Figure 15. Phase 3-normalized TZ and ZT polarization-sensitive waveforms retained after quality control for polarization analysis. The station pairs are the same as in Figure 14; station names are listed at left and inter–station distances at right. Observed waveforms are shown in black, and red curves show the best-fitting waveforms obtained from the TT and ZZ carrier waveforms using the estimated Γ_{ref} and Γ_{fld} values from the procedure described in Section 4.4. Grey vertical lines delimit the signal windows retained for fitting. The fitted waveforms reproduce the principal coherent TZ and ZT arrivals for many station pairs, particularly at shorter inter–station distances.

waveform misfit defined by equation (25). A station pair is retained only if the minimum mean misfit satisfies $\mathcal{J}_{\min} \leq 0.8$. This post-fit criterion reduces the example data set from 42 to 29 station pairs.

Figures 14 and 15 show the 29 Phase 3-normalized station-pair waveforms retained after quality control. All positive carrier lags are retained, whereas six negative carrier lags are rejected; the higher positive-lag retention is consistent with stronger Pacific ambient noise sources. In total, 22 $\overline{TZ}^{-}$, 29 $\overline{TZ}^{+}$, 19 $\overline{ZT}^{-}$, and 28 $\overline{ZT}^{+}$ waveforms are retained for fitting.

4.4 Polarization-parameter estimation and uncertainties

In each narrow period band, we estimate the signed polarization parameters $\Gamma_{\rm ref}$ and $\Gamma_{\rm fld}$ for station pairs whose waveforms pass the quality-control steps of Section 4.3 by fitting the Phase 3-normalized $\overline{TZ}$ and $\overline{ZT}$ waveforms under the assumption of X-dominance. Equations (11) and (12) show that the TR and RT components contain redundant first-order polarization information, but because radial components are generally noisier than the corresponding vertical components, we base the estimation on $\overline{TZ}$ and $\overline{ZT}$ alone. For each trial pair $(\Gamma_{\rm ref}, \Gamma_{\rm fld})$, equations (14)–(17) are evaluated using the observed $\overline{TT}$ and $\overline{ZZ}$ carrier waveforms to predict $\widehat{\overline{TZ}}$ and $\widehat{\overline{ZT}}$. The two polarization parameters are local to the reference and field stations, respectively; within each narrow period band, their frequency dependence and that of the relevant reference eigenfunction ratios are assumed to be negligible.

For an accepted component-lag waveform X, where $X \in \{TZ^{+}, ZT^{+}, TZ^{-}, ZT^{-}\}$, we define the normalized L_2 waveform misfit over its signal window as

$$\mathcal{J}_X(\Gamma_{\rm ref}, \Gamma_{\rm fld}) = \frac{\left\| \widehat{X}(\Gamma_{\rm ref}, \Gamma_{\rm fld}) - \overline{X} \right\|_2}{\left\| \overline{X} \right\|_2}. \tag{25}$$

The signal windows are those defined in Section 4.3. Because the positive and negative lags of TZ and ZT can be accepted or rejected independently, a station pair may contribute two, three, or four component-lag waveforms. Let $\mathcal{A}$ denote the set of accepted waveforms and M their number. The objective function is their mean misfit,

$$\mathcal{J}(\Gamma_{\rm ref}, \Gamma_{\rm fld}) = \frac{1}{M} \sum_{X \in \mathcal{A}} \mathcal{J}_X(\Gamma_{\rm ref}, \Gamma_{\rm fld}). \tag{26}$$

We evaluate $\mathcal{J}$ by grid search over $\mathcal{D} = [-1, 1] \times [-1, 1]$. The grid point at which $\mathcal{J}$ is smallest defines $(\widehat{\Gamma}_{\rm ref}, \widehat{\Gamma}_{\rm fld})$ and the minimum misfit $\mathcal{J}_{\min}$.

For the observations, accepted positive- and negative-lag waveforms are fit jointly whenever available, providing more waveform constraints than in the positive-lag-only numerical benchmarks. The TT–ZZ carrier-waveform correlations for the 29 retained station pairs are also generally smaller than in the poorly conditioned benchmark examples. We therefore do not apply the Stage 2 constraint to these observations; both $\Gamma_{\rm ref}$ and $\Gamma_{\rm fld}$ remain free for each station pair.

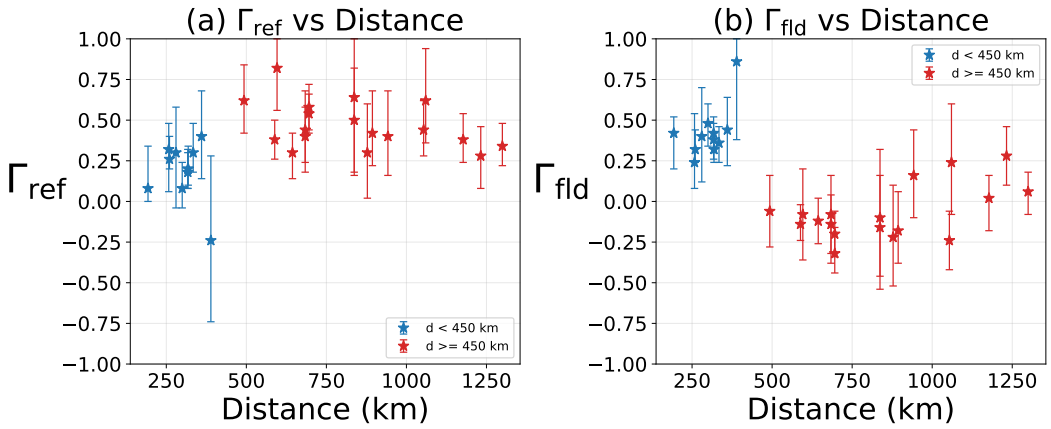

Figure 16. Distance dependence of the polarization-parameter estimates in the 20–30 s period band. (a) Γ_{ref} and (b) Γ_{fld} for the 29 retained station pairs in the narrow-azimuth subset. Blue and red symbols identify field stations at distances less than 450 km and greater than or equal to 450 km, respectively; this division approximately corresponds to crossing the Denali Fault. Error bars show the generally asymmetric operational uncertainty intervals obtained by projecting the $\mathcal{J} \leq 1.2\mathcal{J}_{\min}$ region onto the corresponding parameter axis. For field stations within 450 km, the endpoint estimates are predominantly positive and comparatively coherent. Beyond about 450 km, Γ_{ref} shifts toward larger values while Γ_{fld} becomes predominantly negative before recovering toward zero and positive values at greater distances.

We estimate operational uncertainty intervals from the two-dimensional misfit surface using the empirically calibrated region

$$\mathcal{U} = \{(\Gamma_{\mathrm{ref}}, \Gamma_{\mathrm{fld}}) \in \mathcal{D} : \mathcal{J}(\Gamma_{\mathrm{ref}}, \Gamma_{\mathrm{fld}}) \leq 1.2\mathcal{J}_{\min}\}\,. \tag{27}$$

The factor 1.2 is calibrated from the repeatability of Γ_{ref} among nearby station pairs that share the same reference station. The corresponding parameter ranges define the operational uncertainty intervals shown below. These intervals are practical error estimates rather than formal probabilistic confidence intervals. Errors introduced by the empirical source-group normalization are not represented explicitly in these uncertainty estimates.

The third, post-fit quality-control step of Section 4.3 retains a station pair only if $\mathcal{J}_{\min} \leq 0.8$, leaving 29 station pairs in the 20–30 s narrow-azimuth example. Figure 15 shows the Phase 3-normalized polarization-sensitive waveforms and their best-fitting predictions obtained using $(\widehat{\Gamma}_{\mathrm{ref}}, \widehat{\Gamma}_{\mathrm{fld}})$. Figure 16 presents the resulting polarization-parameter estimates and operational uncertainty intervals, and Figure 17 shows the corresponding component-lag waveform misfits. Their distance dependence and observational implications are described in Section 5.

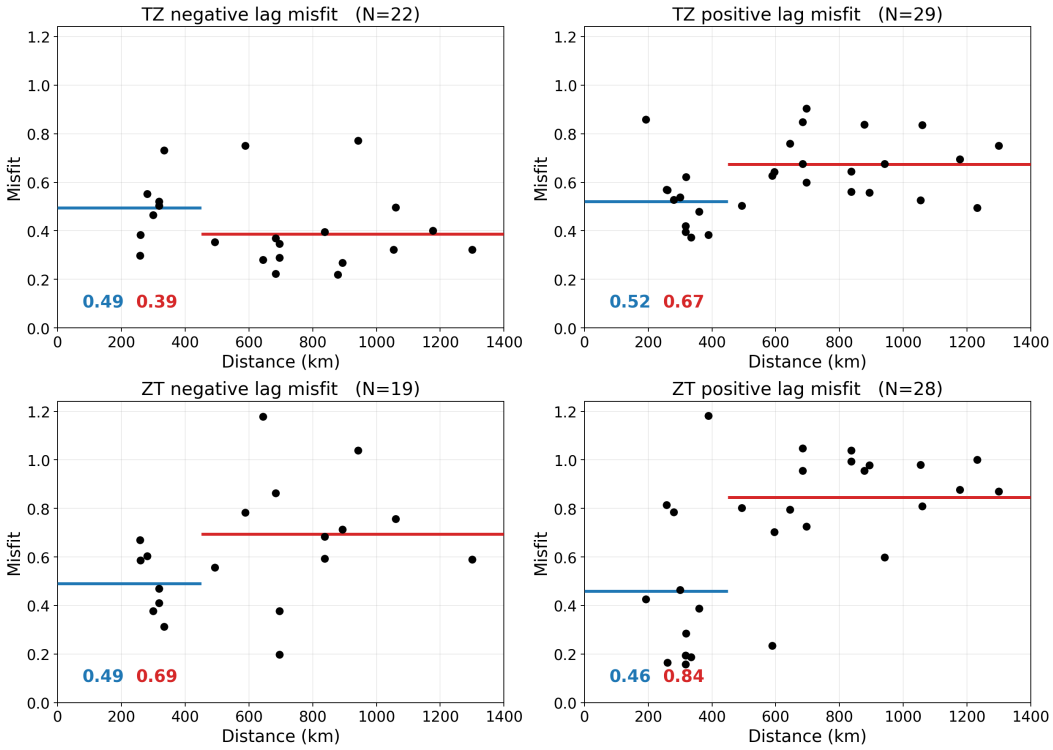

Figure 17. Inter-station distance dependence of the normalized waveform misfit $\mathcal{J}_X$ for the polarization-sensitive components. Results are shown for the accepted (a) TZ^-, (b) TZ^+, (c) ZT^-, and (d) ZT^+ waveforms. Horizontal blue and red lines show the mean misfits for inter–station distances less than 450 km and greater than or equal to 450 km, respectively; their values are given in each panel. Beyond 450 km, the mean misfit increases for three of the four component-lag groups, with TZ^- the exception.

5 EXAMPLE POLARIZATION OBSERVATIONS IN ALASKA

In this section, we present selected polarization observations in Alaska for the 20–30 s narrow-azimuth station subset introduced in Figure 11. We focus on the distance dependence of Γ_{ref} and Γ_{fld} and on the corresponding waveform misfits shown in Figures 16 and 17. The observations are described here primarily in terms of their empirical behavior; their interpretation in relation to lateral structural variations, the validity of the adiabatic approximation, and constraints on the elastic tensor is developed in Section 6.

Figure 16 shows the joint estimates of Γ_{ref} and Γ_{fld} for the 29 station pairs in the narrow-azimuth subset of Figure 11. Because the reference station is fixed at AK-CNP, the estimates of Γ_{ref} provide repeated estimates associated with the same reference location. For field stations within 450 km, Γ_{ref} is generally positive and comparatively coherent, with estimates averaging about 0.25. The corresponding Γ_{fld} estimates are also predominantly positive and cluster around a mean of about 0.35. The

scatter of the individual estimates about these mean values is largely encompassed by their operational uncertainty intervals.

The behavior changes markedly for field stations beyond 450 km from the reference station. The Γ_{ref} estimates remain positive but are, on average, shifted toward larger values. In contrast, Γ_{fld} changes sign shortly beyond 450 km and is predominantly negative over much of the intermediate distance range. At larger distances, Γ_{fld} increases again toward zero and positive values. Along these propagation paths, the Denali Fault lies approximately 450 km from the reference location, so the change in the polarization estimates occurs approximately where the paths begin to cross the fault.

The waveform misfits in Figure 17 also change across this distance range. For field stations within 450 km, the four component-lag groups have similar mean normalized waveform misfits, between 0.46 and 0.52. Beyond 450 km, the mean misfit increases from 0.52 to 0.67 for TZ^{+}, from 0.49 to 0.69 for ZT^{-}, and from 0.46 to 0.84 for ZT^{+}. The TZ^{-} observations behave differently, with their mean misfit decreasing from 0.49 to 0.39. Thus, beyond about 450 km, the polarization-parameter estimates change systematically and the mean waveform misfit increases for three of the four component-lag groups. The origin and interpretation of these observations are examined in Section 6.

6 DISCUSSION

The theory, numerical benchmarks, and Alaska observations presented above show that surface-wave polarization can be measured from ambient noise cross-correlations and, when propagation is sufficiently adiabatic, interpreted in terms of local anisotropic structure. We first examine the physical interpretation of the adiabatic condition and the factors that control conversion between quasi-Rayleigh and quasi-Love waves. Two practical questions then follow. First, because polarization may remain measurable even when nonadiabatic propagation compromises its local interpretability, how should polarization measurements be selected and used so that they are most likely to represent local structure reliably? Second, when local interpretation is justified, what additional constraints can polarization provide when combined with the phase-speed observations conventionally used to infer anisotropy?

6.1 Physical interpretation of the adiabatic condition

Equation (1) provides a simple operational criterion for adiabatic surface-wave propagation by requiring the characteristic length scale of structural variation to be large compared with the wavelength. This condition is useful, but incomplete. A reduced two-mode propagation analysis presented in Section 1 of the Supplementary Materials provides a more complete interpretation. It shows that adiabaticity depends not only on the spatial scale of structural variation, but also on the magnitude of the

resulting polarization change and the separation of the quasi-Rayleigh and quasi-Love branches. In either the X-dominant or E-dominant limit, the phase relating the complex mixing coefficient χ to the signed real polarization parameter Γ is spatially constant, so that $|\mathrm{d}\chi/\mathrm{d}x| = |\mathrm{d}\Gamma/\mathrm{d}x|$. For a characteristic change $\Delta\Gamma$ occurring over a structural length scale $\ell_{\mathrm{structure}}$, the more complete adiabaticity condition can be written as

$$\varepsilon_{\mathrm{ad}} \sim \frac{|\Delta\Gamma|}{|\Delta k|\,\ell_{\mathrm{structure}}} = \frac{\bar{k}|\Delta\Gamma|}{2\pi|\Delta k|}\frac{\lambda_{\mathrm{wave}}}{\ell_{\mathrm{structure}}} \ll 1, \tag{28}$$

where $\Delta k = k_{qR} - k_{qL}$, $\bar{k} = (k_{qR} + k_{qL})/2$, and $\lambda_{\mathrm{wave}} = 2\pi/\bar{k}$. Equation (28) is equation (S43) of the Supplementary Materials. The spatial variation of Γ entering equation (28) need not arise solely from changes in anisotropy. In the X- and E-dominant regimes, respectively, $\Gamma = X/(A - B)$ and $\Gamma = E/(A - B)$, so variations in Γ can result from changes in the anisotropic coupling numerator, the branch-separation denominator, or both. Changes in isotropic structure can therefore affect Γ by altering the separation of the quasi-Rayleigh and quasi-Love branches. In particular, even if the magnitude of anisotropy changes little, $|\Gamma|$ can increase substantially as the branches approach quasi-degeneracy, making the adiabatic condition more difficult to satisfy. The effects of quasi-degeneracy are discussed in detail by Liu & Ritzwoller (2025).

Equation (28) compares the spatial rate of change of the local polarization with the wavenumber separation of the two propagation branches. The quantity $|\Delta\Gamma|/\ell_{\mathrm{structure}}$ characterizes the spatial rate of polarization change, whereas $|\Delta k|$ measures the separation of the quasi-Rayleigh and quasi-Love branches at fixed frequency. When the spatial gradient in polarization is small relative to the branch separation, a wave remains predominantly on its instantaneous local eigenbranch and its polarization follows the local anisotropic structure. If the polarization varies too strongly over a short distance, or if the two branches are too closely separated, significant mode conversion can occur between the quasi-Rayleigh and quasi-Love branches (e.g., Park & Yu, 1992). The resulting wavefield then contains converted quasi-Rayleigh and quasi-Love energy, and when the converted and unconverted contributions overlap in the measured waveform, the measured polarization need not represent the local polarization of either branch.

This fuller criterion clarifies both the usefulness and the limitations of the wavelength criterion in equation (1). When $|\Delta\Gamma|$ is modest and the branch separation is not unusually small, the ratio $\lambda_{\mathrm{wave}}/\ell_{\mathrm{structure}}$ can provide a useful proxy for the degree of adiabaticity. The qualitative period dependence of the stair-step benchmarks in Section 3 is consistent with this wavelength scaling. In contrast, a sufficiently large localized change in polarization can produce substantial nonadiabatic conversion even when the structural change is confined to a single region, as explored in Section 6.2.

For observations, the quantities entering equation (28) are generally not known accurately along

the entire propagation path. The criterion therefore does not provide a simple a priori test of whether an individual polarization measurement is locally interpretable but instead explains physically why both the magnitude and spatial scale of structural variations along a path matter. It also motivates the conservative approach to observational interpretation discussed in Section 6.2.

6.2 Practical interpretation of station polarization parameters

In the adiabatic theory, the two endpoint parameters Γ_{ref} and Γ_{fld} have equivalent local meanings: each describes the polarization at one of the two station locations used in the cross-correlation. The numerical benchmarks in Section 3 show that both parameters can be recovered when propagation is sufficiently adiabatic. In practice, however, local interpretability depends on whether variations in anisotropy along the propagation path significantly perturb the quasi-Rayleigh and quasi-Love wavefields. Because the degree of adiabaticity of a real propagation path is generally not known a priori, we advise a conservative strategy when interpreting the inferred polarization parameters as local constraints on Earth structure.

The shorter-distance observations in Figure 16 illustrate the most favorable regime for interpretation. For field stations south of the Denali Fault, Γ_{ref} and Γ_{fld} have similar mean values, repeated estimates of Γ_{ref} at the fixed reference location are mutually consistent within their uncertainties, and the waveform fits are comparatively stable (Figures 15 and 17). These observations are consistent with the behavior of the homogeneous and slowly varying numerical benchmarks in Section 3.

A markedly different pattern appears after the propagation paths cross the Denali Fault. The reference location remains fixed south of the fault, yet the inferred Γ_{ref} shifts systematically to larger values when the field stations lie north of it. At the same time, Γ_{fld} changes sign and varies systematically with distance, and the waveform fits degrade on average. The dependence of Γ_{ref} on the location of a distant field station, despite the fixed reference location, indicates that the fitted endpoint parameters have acquired path sensitivity and casts doubt on their local interpretability.

To illuminate this behavior, we consider an additional numerical experiment containing a single sharp discontinuity in anisotropy 450 km from the reference station (Figure 18). Before the discontinuity, the model is identical to the homogeneous benchmark of Section 3.1; beyond it, the medium is isotropic. Before the discontinuity is crossed, the inferred endpoint parameters remain close to their input values. After crossing it, the inferred Γ_{ref} increases even though its true value has not changed, while Γ_{fld} develops a negative downstream excursion before gradually recovering toward zero.

The behavior of this numerical experiment is qualitatively similar to the distance dependence in Figure 16. In both cases, crossing a strong structural boundary is followed by an increase in the apparent reference-location parameter and a change of sign in the field-station parameter. We do not

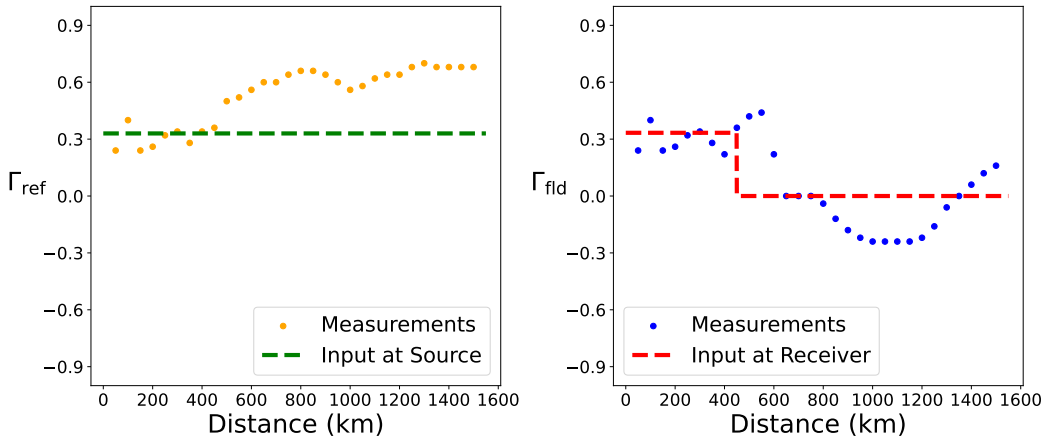

Figure 18. Polarization-parameter measurements versus source–receiver distance for a numerical model containing a sharp discontinuity in anisotropy 450 km from the source location. The source and receiver locations correspond, respectively, to the reference- and field-station locations used in the observational analysis. Before the discontinuity, the model is identical to the homogeneous benchmark, with input $\Gamma = 0.33$; beyond it, the medium is isotropic, so the receiver-location input parameter becomes zero while the source-location input remains 0.33. The inferred parameters agree approximately with their input values before the discontinuity but display a downstream boundary transient after it is crossed, where the inferred endpoint parameters no longer represent their local input values.

expect this numerical experiment to reproduce the Alaska observations quantitatively, because it was not designed to model the change in anisotropy across the Denali Fault. The principal conclusion is that a single sharp structural change in this numerical experiment generates a significant downstream boundary transient. Within this transient, polarization remains measurable, but the fitted endpoint parameters need not equal the polarization parameters implied by the local elastic structure at the two stations. In this experiment, loss of local interpretability arises from a single sharp structural change rather than repeated scattering along a complicated path.

This result clarifies the practical roles of Γ_{ref} and Γ_{fld}. Both parameters are equally interpretable when wave propagation is adiabatic, but Γ_{ref} has an important practical advantage. A single reference station can be paired with several nearby field stations, providing repeated estimates associated with the same physical location. When these estimates are mutually consistent, as for the shorter Alaska paths in Figure 16, their repeatability provides empirical evidence against substantial path-dependent contamination. The field-station parameter Γ_{fld} can likewise reflect the local polarization under favorable propagation conditions, but it lacks repeated estimation at a fixed location unless other paths are considered.

For practical applications, we recommend repeated estimates of Γ_{ref} from relatively short paths, together with mutually consistent estimates and satisfactory fits to the polarization-sensitive wave-

forms. Ideally, the reference and field stations should also lie within the same broad tectonic domain so that major faults or other strong structural boundaries do not intervene along the propagation path. These criteria provide the most favorable circumstances for obtaining polarization parameter estimates that are locally interpretable.

6.3 Joint constraints from polarization and phase speed

Here we consider what information surface-wave polarization adds to the Rayleigh- and Love-wave phase-speed observations conventionally used to infer anisotropy. We compare an inversion using the Rayleigh- and Love-wave 2ψ and 4ψ phase-speed observations with a joint inversion that also includes polarization. Ideally, polarization would itself be measured as a function of propagation azimuth and period. The present example is deliberately more limited. We use the reference-station polarization parameter estimated from the restricted azimuthal range considered in Section 5, with $\Gamma_{\mathrm{ref}} \simeq 0.3$ at approximately 25 s period, representative of the 20–30 s band. This provides a single polarization constraint associated with the reference location and sampled propagation azimuth. The comparison therefore illustrates the additional constraint provided by even a single polarization measurement.

The inversions use a TTI model of the crust and uppermost mantle and closely follow the procedures of Xie et al., (2015, 2017) and C. Liu & Ritzwoller (2024) but revised with the quasi-degenerate theory of X. Liu & Ritzwoller (2025) that incorporates Rayleigh-Love coupling. We use Rayleigh- and Love-wave 2ψ and 4ψ phase-speed observations from Liu et al. (2025). Figure 19 shows the 2ψ observations at AK-CNP and the corresponding fits from models accepted in the phase-speed-only and joint inversions. The two inversions provide comparable fits to the phase-speed observations shown, but the accepted models differ substantially in their predicted polarization. Models accepted using the phase-speed observations alone span a broad range of polarization values, including both signs of Γ_{ref}. When the polarization observation is added, the predicted polarization is restricted to values consistent with the measured constraint while the phase-speed fits remain essentially unchanged. Thus, polarization provides a complementary constraint on the Rayleigh–Love coupling among models accepted by the phase-speed-only inversion.

The effect on the inferred anisotropic structure is illustrated by the posterior distributions in Figures 20 and 21, shown at crustal depths of 8 and 30 km and at a mantle depth of 80 km. The inferred strike angle is qualitatively consistent with the receiver function results in this region (Schulte-Pelkum et al., 2020). The clearest change concerns the dip of the symmetry axis of the TTI structure. With the phase-speed observations alone (Figure 20), the posterior distribution contains two principal modes corresponding to opposite senses of dip; thus, phase-speed observations do not uniquely resolve the dip orientation. Adding polarization (Figure 21) strongly suppresses one of the two modes and pro-

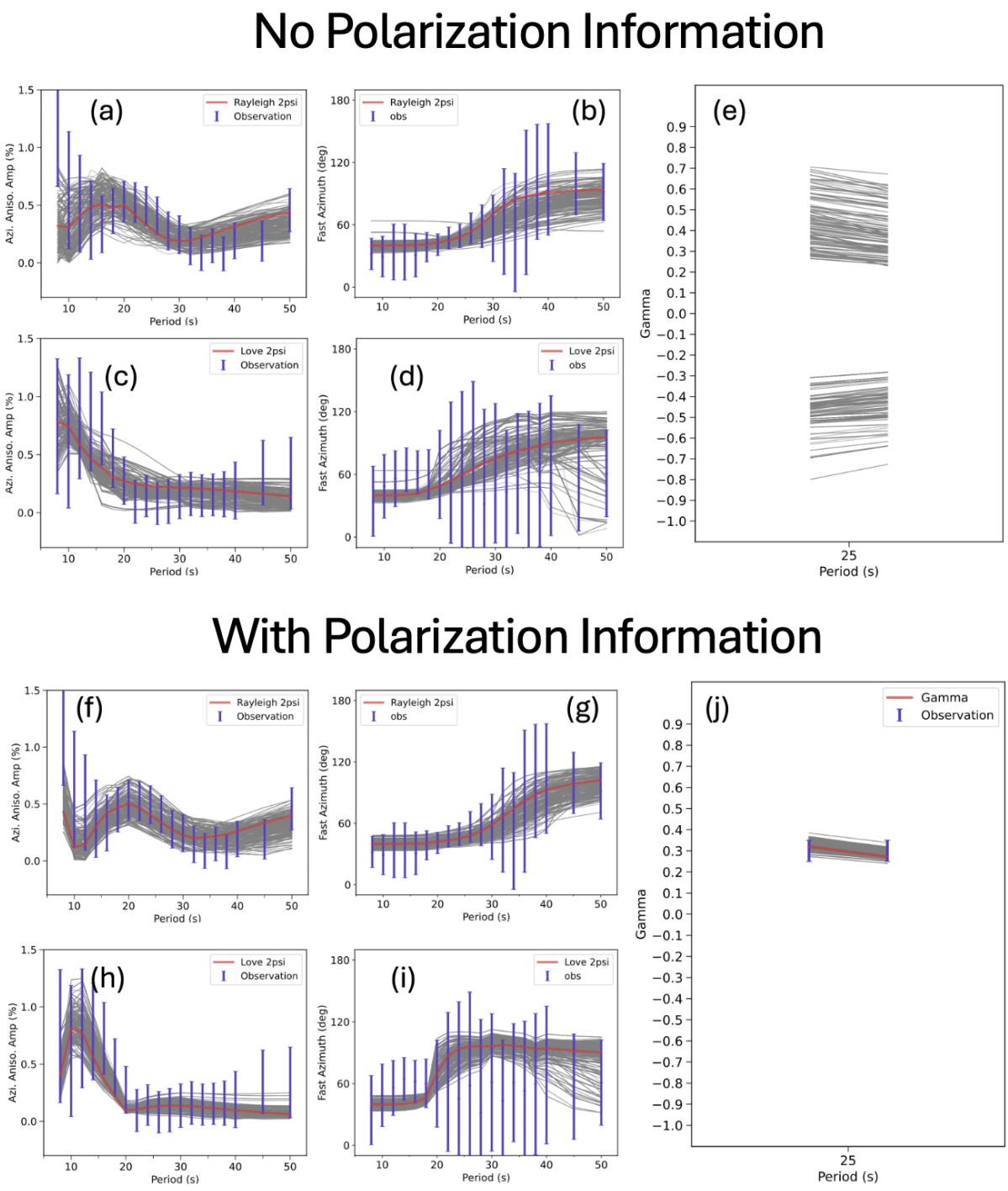

Figure 19. Effect of adding a polarization observation to inversions using Rayleigh- and Love-wave 2ψ and 4ψ phase-speed observations. Only the 2ψ phase-speed observations and fits are shown. (a)–(e) Fits to the 2ψ phase-speed observations and corresponding polarization predictions from models accepted using the phase-speed observations alone. (f)–(j) Corresponding results from models accepted in the joint inversion that also includes the polarization observation. The two inversions provide comparable fits to the 2ψ phase-speed observations shown, whereas including polarization restricts the accepted models to polarization values consistent with the observation.

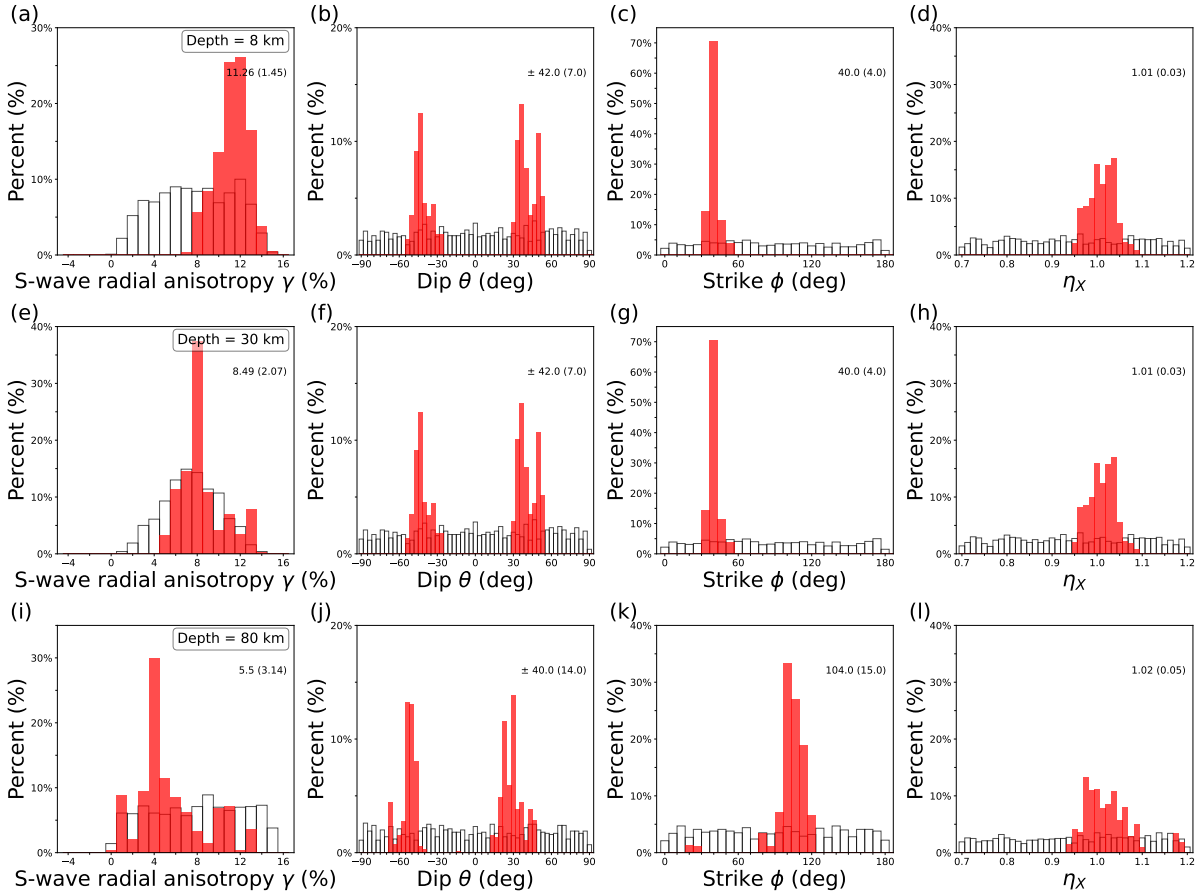

Figure 20. Posterior (red) and prior (white) distributions of selected TTI anisotropy parameters for inversion of Rayleigh- and Love-wave 2ψ and 4ψ phase-speed observations. Rows show results at depths of 8, 30, and 80 km; columns show S-wave radial anisotropy γ, dip θ, strike ϕ, and ellipticity η_X. Here $\gamma = (N - L)/(2L)$, where N and L are Love moduli of the underlying VTI tensor before tilting; θ is the dip of the symmetry axis, ϕ defines its strike, and η_X is the ellipticity parameter. Numbers in each panel give the posterior mean, with the standard deviation in parentheses. The dip distributions retain two principal modes with opposite dip orientations.

duces a single preferred dip orientation, with the selected sense of dip depending on the sign of the polarization parameter. The two solutions represent different senses of inclination of the anisotropic fabric and can therefore lead to different tectonic interpretations (e.g., Bokelmann, 2002). Adding polarization also narrows the posterior distributions of several other anisotropic parameters, although these changes are less pronounced than the resolution of the dip-orientation ambiguity.

Figures 19–21 illustrate two complementary roles for polarization. The polarization observation constrains the Rayleigh–Love coupling among models accepted by the phase-speed-only inversion and, in this example, resolves the dip-orientation ambiguity that remains after inversion of the 2ψ and

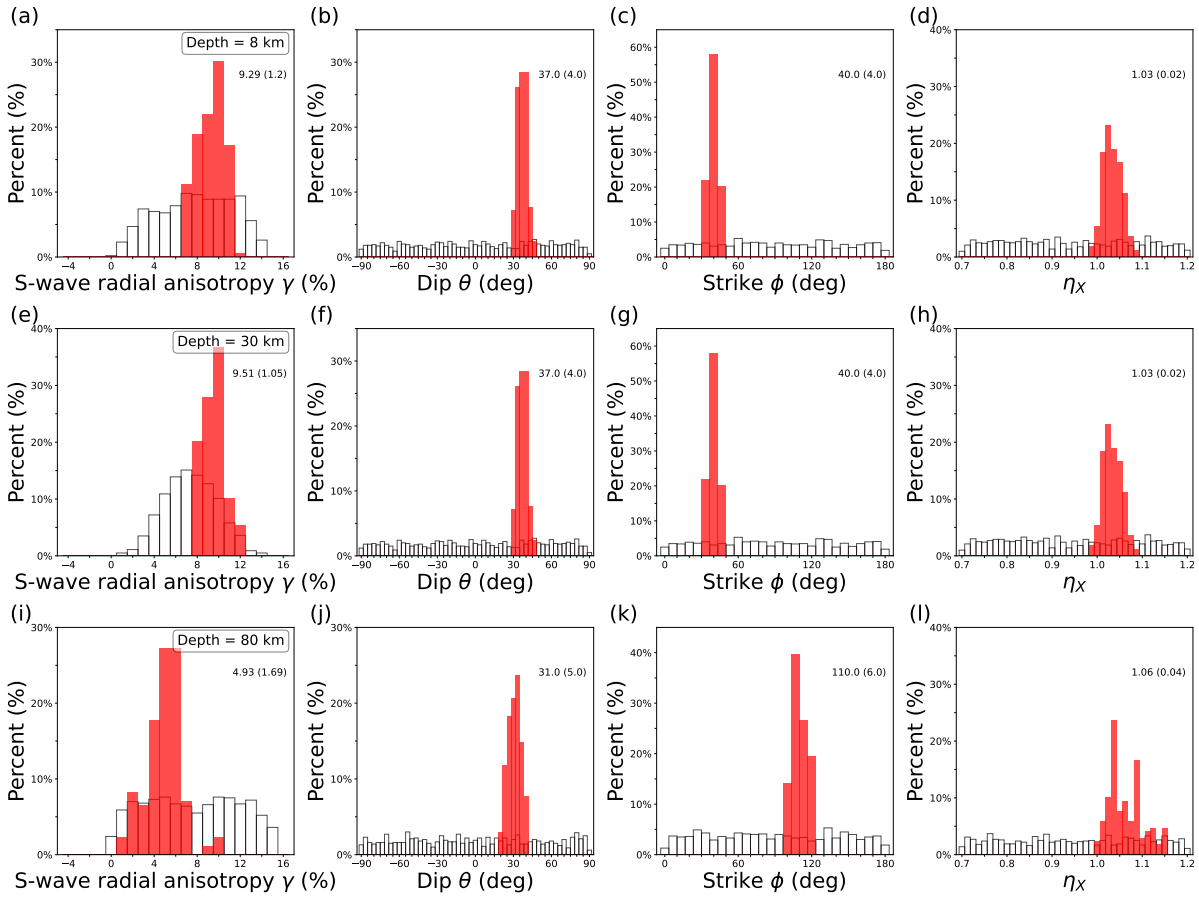

Figure 21. Effect of adding a polarization observation on the posterior distributions of selected TTI anisotropy parameters. Similar to Figure 20, but for the joint inversion of Rayleigh- and Love-wave 2ψ and 4ψ phase-speed observations and the polarization observation. Numbers in each panel give the posterior mean, with the standard deviation in parentheses. Including polarization strongly suppresses one of the two principal dip-orientation modes and narrows the posterior distributions of other anisotropy parameters.

4ψ phase-speed observations alone. The comparison illustrates how surface-wave polarization can provide structural information that is not supplied by conventional phase-speed observations alone.

7 CONCLUSIONS

We present a theory that relates the polarization of quasi-Rayleigh and quasi-Love waves in anisotropic media directly to the appropriately source-group-normalized ambient noise cross-correlation tensor. Within the two-mode, weak-mixing approximation, the complex Rayleigh–Love mixing coefficient is determined by depth integrals of the elastic tensor and reference eigenfunctions. In either the E-dominant or X-dominant limit considered here, a single signed polarization parameter Γ_j governs the first-order polarization perturbations of both quasi-Rayleigh and quasi-Love waves at a given station

and period, although their polarization angles are generally different. The resulting waveform relations connect the TT and ZZ carrier waveforms to the polarization-sensitive TZ and ZT waveforms and allow the polarization parameters at the reference (Γ_{ref}) and field (Γ_{fld}) stations to be estimated jointly even when the quasi-Rayleigh and quasi-Love arrivals overlap in time.

The source-group normalization is a critical bridge between the theory and its observational application because source-related amplitude factors must be removed before relative amplitudes among tensor components can be interpreted in terms of polarization. In addition to the well-established ambient noise processing procedures of Phases 1 and 2, we introduce a Phase 3 that approximates this theoretical normalization empirically using the observed TT and ZZ carrier amplitudes. This step allows the theoretical polarization relations to be applied to ambient noise cross-correlations while preserving the relative amplitudes that carry the polarization information. Because the empirical normalization is approximate, it remains a potential source of uncertainty in the estimated polarization parameters.

Successfully measuring surface-wave polarization does not necessarily imply that the measurement can be interpreted reliably in terms of local anisotropic structure. Such an interpretation requires sufficiently adiabatic propagation, in which the polarizations of quasi-Rayleigh and quasi-Love waves evolve smoothly with the local anisotropic structure as the waves propagate, so that each wave retains its local character with negligible mode conversion between the two wave types. The operational wavelength criterion provides a useful guide, while the more complete two-mode condition shows that adiabaticity depends on the spatial scale and magnitude of the resulting polarization change and on the separation of the quasi-Rayleigh and quasi-Love branches. The numerical benchmarks also identify two distinct limitations on polarization-parameter recovery. Poor conditioning can produce strong trade-offs between Γ_{ref} and Γ_{fld} even when the forward theory remains accurate, whereas sufficiently nonadiabatic propagation degrades the forward theory itself and compromises local interpretability. In the sharp-discontinuity numerical experiment, a single sharp structural change generates a downstream boundary transient in which polarization remains measurable, but the fitted endpoint parameters need not represent the polarization implied by the local elastic structure.

These results motivate a conservative strategy for local interpretation of polarization measurements. We recommend repeated estimates of Γ_{ref} from relatively short paths, favoring cases in which the estimates are mutually consistent and the polarization-sensitive waveforms are fit satisfactorily. Ideally, the reference and field stations should lie within the same broad tectonic domain so that major faults or other strong structural boundaries do not intervene along the propagation path. These criteria provide the most favorable circumstances for obtaining polarization-parameter estimates that are locally interpretable.

The Alaska observations show that our methods can be applied to real ambient noise data to obtain polarization measurements that provide meaningful constraints on local anisotropic structure. For the 20–30 s observations considered here, repeated estimates of Γ_{ref} from relatively short paths south of the Denali Fault are mutually consistent, and the corresponding Γ_{fld} estimates show similar behavior. For paths crossing the Denali Fault, the inferred Γ_{ref} changes systematically even though the reference location is fixed, while Γ_{fld} also varies strongly with distance and the waveform fits degrade on average. Together with the sharp-discontinuity numerical experiment, these observations indicate that, when field stations lie beyond the fault, the measured polarization is affected by a boundary transient associated with the change in anisotropic structure across the Denali Fault, compromising the local interpretation of the fitted polarization parameters.

The joint inversion of phase-speed observations and polarization provides a concrete example of the additional structural information supplied by polarization. An inversion of the Rayleigh- and Love-wave 2ψ and 4ψ phase-speed observations alone produces accepted models in which the dip of the TTI symmetry axis is nonunique; adding a single polarization constraint resolves this nonuniqueness by strongly suppressing one of the two principal dip modes. Polarization also narrows the posterior distributions of other anisotropic parameters. These results demonstrate that polarization can materially reduce nonuniqueness in estimates of three-dimensional anisotropic structure. Moreover, because the alternative dip solutions correspond to distinct three-dimensional orientations of the anisotropic fabric, resolving this ambiguity may have important tectonic implications.

Future work should extend both the observational and theoretical developments presented here. Observationally, polarization measurements should be expanded to other regions and to broader ranges of propagation azimuth and period, particularly where station coverage permits repeated estimates at common reference locations. Theoretically, an important goal is to extend the present treatment beyond the adiabatic approximation by describing explicitly the conversion between quasi-Rayleigh and quasi-Love waves through strongly heterogeneous structure. Such a theory could ultimately allow both the locally interpretable polarization measurements emphasized here and the boundary transients generated by strong structural variations to be exploited as complementary constraints on anisotropy in the Earth.

8 ACKNOWLEDGEMENTS

We are very grateful to Qicheng Zeng and Fan-Chi Lin for providing data processing software. We are also very grateful to Chuanming Liu for providing the depth-dependent elastic tensor model beneath Alaska (C. Liu & Ritzwoller, 2024). We greatly appreciate help from IRIS Data Services, which are funded through the Seismological Facilities for the Advancement of Geoscience and EarthScope

(SAGE) Proposal of the National Science Foundation under Cooperative Agreement EAR-1851048. Aspects of this research were supported by EAR-1928395 and EAR-1952209 at the University of Colorado Boulder.

9 DATA AVAILABILITY STATEMENT

Original seismic waveform data were obtained from the Data Management Center of IRIS (www.iris.edu). ObsPy (Beyreuther *et al*. 2010) is used in data processing.

REFERENCES

Aki, K. & Richards, P. G., 2002. *Quantitative seismology*.

Bensen, G., Ritzwoller, M., Barmin, M., Levshin, A. L., Lin, F., Moschetti, M., Shapiro, N., & Yang, Y., 2007. Processing seismic ambient noise data to obtain reliable broad-band surface wave dispersion measurements, *Geophysical journal international*, **169**(3), 1239–1260.

Beyreuther, M., Barsch, R., Krischer, L., Megies, T., Behr, Y., & Wassermann, J., 2010. Obspy: A python toolbox for seismology, *Seismological Research Letters*, **81**(3), 530–533.

Bokelmann, G., 2002. Which forces drive north america?, *Geology*, **30**(11), 1027–1030.

Bowden, D. C., Tsai, V. C., & Lin, F.-C., 2017. Amplification and attenuation across usarray using ambient noise wavefront tracking, *Journal of Geophysical Research: Solid Earth*, **122**(12), 10–086.

Chen, M. & Tromp, J., 2007. Theoretical and numerical investigations of global and regional seismic wave propagation in weakly anisotropic earth models, *Geophysical Journal International*, **168**(3), 1130–1152.

Cheng, W., Hu, X., & Liu, L., 2021. Anisotropy gradients in the middle of the ross sea embayment, west antarctica: Evidence from ql scattered surface waves, *Geophysical Research Letters*, **48**(6), e2020GL091232.

Cheng, W., Hu, X., Lu, Y., Liang, X., Liu, L., Zhang, P., & Zhou, Y., 2026. Lateral anisotropic gradients in the subslab mantle beneath the kuril subduction zone detected by observations of quasi-love wave scattering, *Tectonophysics*, p. 231066.

Cupillard, P. & Capdeville, Y., 2010. On the amplitude of surface waves obtained by noise correlation and the capability to recover the attenuation: a numerical approach, *Geophysical Journal International*, **181**(3), 1687–1700.

Denolle, M., Dunham, E., Prieto, G., & Beroza, G., 2013. Ground motion prediction of realistic earthquake sources using the ambient seismic field, *Journal of Geophysical Research: Solid Earth*, **118**(5), 2102–2118.

Denolle, M., Dunham, E., Prieto, G., & Beroza, G., 2014. Strong ground motion prediction using virtual earthquakes, *Science*, **343**(6169), 399–403.

Durand, S., Montagner, J., Roux, P., Brenguier, F., Nadeau, R., & Ricard, Y., 2011. Passive monitoring of anisotropy change associated with the parkfield 2004 earthquake, *Geophysical Research Letters*, **38**(13).

Eakin, C. M., 2021. Quasi-love wave scattering reveals tectonic history of australia and its margins reflected by mantle anisotropy, *Communications Earth & Environment*, **2**(1), 210.

Kennett, B., 1984. Guided wave propagation in laterally varying media—i. theoretical development, *Geophysical Journal International*, **79**(1), 235–255.

Komatitsch, D. & Tromp, J., 1999. Introduction to the spectral element method for three-dimensional seismic wave propagation, *Geophysical journal international*, **139**(3), 806–822.

Levin, V. & Park, J., 1998. Quasi-love phases between tonga and hawaii: Observations, simulations, and explanations, *Journal of Geophysical Research: Solid Earth*, **103**(B10), 24321–24331.

Levin, V., Park, J., Lucente, F., Margheriti, L., & Pondrelli, S., 2007. End of subduction in northern apennines confirmed by observations of quasi-love waves from the great 2004 sumatra-andaman earthquake, *Geophysical Research Letters*, **34**(4).

Lin, F.-C., Moschetti, M. P., & Ritzwoller, M. H., 2008. Surface wave tomography of the western united states from ambient seismic noise: Rayleigh and love wave phase velocity maps, *Geophysical Journal International*, **173**(1), 281–298.

Lin, F.-C., Ritzwoller, M. H., & Shen, W., 2011. On the reliability of attenuation measurements from ambient noise cross-correlations, *Geophysical Research Letters*, **38**(11).

Lin, F.-C., Tsai, V. C., & Schmandt, B., 2014. 3-d crustal structure of the western united states: application of rayleigh-wave ellipticity extracted from noise cross-correlations, *Geophysical Journal International*, **198**(2), 656–670.

Liu, C. & Ritzwoller, M. H., 2024. Seismic anisotropy and deep crustal deformation across alaska, *Journal of Geophysical Research: Solid Earth*, **129**(5), e2023JB028525.

Liu, X. & Ritzwoller, M. H., 2025. The effect of rayleigh–love coupling in an anisotropic medium, *Geophysical Journal International*, **241**(2), 1204–1225.

Liu, X., Liu, C., & Ritzwoller, M. H., 2025. The characteristics of rayleigh and love wave azimuthal anisotropy: Observations across alaska, *Journal of Geophysical Research: Solid Earth*, **130**(11), e2025JB032042.

Liu, X., Liu, C., & Ritzwoller, M. H., 2026. The elastic tensor in the crust and uppermost mantle beneath alaska from surface wave observations, *Manuscript in preparation*.

Maupin, V., 1988. Surface waves across 2-d structures: a method based on coupled local modes, *Geophysical Journal International*, **93**(1), 173–185.

Merry, T. A. & Eakin, C. M., 2024. Insights on the african upper mantle from quasi-love wave scattering, *Geochemistry, Geophysics, Geosystems*, **25**(4), e2023GC011385.

Montagner, J.-P. & Nataf, H.-C., 1986. A simple method for inverting the azimuthal anisotropy of surface waves, *Journal of Geophysical Research: Solid Earth*, **91**(B1), 511–520.

Park, J., 1990. The subspace projection method for constructing coupled-mode synthetic seismograms, *Geophysical Journal International*, **101**(1), 111–123.

Park, J. & Yu, Y., 1992. Anisotropy and coupled free oscillations: simplified models and surface wave observations, *Geophysical Journal International*, **110**(3), 401–420.

Peng, H. & Li, J., 2024. Rayleigh wave attenuation tomography based on ambient noise interferometry: methods and an application to northeast china, *Geophysical Journal International*, **237**(3), 1536–1553.

Pettersen, Ø. & Maupin, V., 2002. Lithospheric anisotropy on the kerguelen hotspot track inferred from rayleigh wave polarisation anomalies, *Geophysical journal international*, **149**(1), 225–246.

Prieto, G., Lawrence, J., & Beroza, G., 2009. Anelastic earth structure from the coherency of the ambient seismic field, *Journal of Geophysical Research: Solid Earth*, **114**(B7).

Prieto, G. A. & Beroza, G. C., 2008. Earthquake ground motion prediction using the ambient seismic field, *Geophysical Research Letters*, **35**(14).

Rieger, D. & Park, J., 2010. Usarray observations of quasi-love surface wave scattering: Orienting anisotropy in the cascadia plate boundary, *Journal of Geophysical Research: Solid Earth*, **115**(B5).

Ritzwoller, M. H., Feng, L., Nakata, N., Gualtieri, L., & Fichtner, A., 2019. Overview of pre-and post-

processing of ambient noise correlations, *Seismic ambient noise*, pp. 144–187.

Saade, M., Montagner, J., Roux, P., Cupillard, P., Durand, S., & Brenguier, F., 2015. Influence of seismic anisotropy on the cross correlation tensor: numerical investigations, *Geophysical Journal International*, **201**(2), 595–604.

Saadé, M., Montagner, J.-P., Roux, P., Shiomi, K., Enescu, B., & Brenguier, F., 2017. Monitoring of seismic anisotropy at the time of the 2008 iwate-miyagi (japan) earthquake, *Geophysical Journal International*, **211**(1), 483–497.

Saade, M., Araragi, K., Montagner, J. P., Kaminski, E., Roux, P., Aoki, Y., & Brenguier, F., 2019. Evidence of reactivation of a hydrothermal system from seismic anisotropy changes, *Nature communications*, **10**(1), 5278.

Schulte-Pelkum, V., Caine, J. S., Jones III, J. V., & Becker, T. W., 2020. Imaging the tectonic grain of the northern cordillera orogen using transportable array receiver functions, *Seismological Society of America*, **91**(6), 3086–3105.

Servali, A., Long, M. D., Park, J., Benoit, M. H., & Aragon, J. C., 2020. Love-to-rayleigh scattering across the eastern north american passive margin, *Tectonophysics*, **776**, 228321.

Stehly, L., Campillo, M., & Shapiro, N., 2006. A study of the seismic noise from its long-range correlation properties, *Journal of Geophysical Research: Solid Earth*, **111**(B10).

Tanimoto, T., 1987. Surface-wave ray tracing equations and fermat's principle in an anisotropic earth, *Geophysical Journal International*, **88**(1), 231–240.

Tanimoto, T., 2004. The azimuthal dependence of surface wave polarization in a slightly anisotropic medium, *Geophysical Journal International*, **156**(1), 73–78.

Thomsen, L., 1986. Weak elastic anisotropy, *Geophysics*, **51**(10), 1954–1966.

Tromp, J., 1994a. A coupled local-mode analysis of surface-wave propagation in a laterally heterogeneous waveguide, *Geophysical Journal International*, **117**(1), 153–161.

Tromp, J., 1994b. Surface-wave propagation on a rotating, anisotropic earth, *Geophysical Journal International*, **117**(1), 141–152.

Tromp, J. & Dahlen, F., 1992. Variational principles for surface wave propagation on a laterally heterogeneous earth—ii. frequency-domain jwkb theory, *Geophysical Journal International*, **109**(3), 599–619.

Tromp, J. & Dahlen, F., 1993. Surface wave propagation in a slowly varying anisotropic waveguide, *Geophysical Journal International*, **113**(1), 239–249.

Tsai, V. C., 2009. On establishing the accuracy of noise tomography travel-time measurements in a realistic medium, *Geophysical Journal International*, **178**(3), 1555–1564.

Tsai, V. C., 2010. The relationship between noise correlation and the green's function in the presence of degeneracy and the absence of equipartition, *Geophysical Journal International*, **182**(3), 1509–1514.

Tsai, V. C., 2011. Understanding the amplitudes of noise correlation measurements, *Journal of Geophysical Research: Solid Earth*, **116**(B9).

Wapenaar, K., 2004. Retrieving the elastodynamic green's function of an arbitrary inhomogeneous medium

by cross correlation, *Physical review letters*, **93**(25), 254301.

Weaver, R. L., 2011. On the amplitudes of correlations and the inference of attenuations, specific intensities and site factors from ambient noise, *Comptes Rendus. Géoscience*, **343**(8-9), 615–622.

Woodhouse, J., 1974. Surface waves in a laterally varying layered structure, *Geophysical Journal International*, **37**(3), 461–490.

Xie, J., Ritzwoller, M. H., Brownlee, S., & Hacker, B., 2015. Inferring the oriented elastic tensor from surface wave observations: preliminary application across the western united states, *Geophysical Journal International*, **201**(2), 996–1021.

Xie, J., Ritzwoller, M. H., Shen, W., & Wang, W., 2017. Crustal anisotropy across eastern tibet and surroundings modeled as a depth-dependent tilted hexagonally symmetric medium, *Geophysical Journal International*, **209**(1), 466–491.

Yu, Y. & Park, J., 1994. Hunting for azimuthal anisotropy beneath the pacific ocean region, *Journal of Geophysical Research: Solid Earth*, **99**(B8), 15399–15421.

Yu, Y., Park, J., & Wu, F., 1995. Mantle anisotropy beneath the tibetan plateau: Evidence from long-period surface waves, *Physics of the Earth and Planetary Interiors*, **87**(3-4), 231–246.

Zhou, L., Song, X., & Weaver, R. L., 2020. Retrieval of amplitude and attenuation from ambient seismic noise: synthetic data and practical considerations, *Geophysical Journal International*, **222**(1), 544–559.

APPENDIX A: THEORETICAL DERIVATION

Let $\boldsymbol{x}_{\mathrm{ref}}$ and $\boldsymbol{x}_{\mathrm{fld}}$ denote a fixed reference station and a fixed field station. The observational R, T, Z coordinate system is defined once, with $\hat{\boldsymbol{R}}$ directed from the reference station toward the field station; the same axes are retained at both correlation lags. For a cross-correlation component XY, the first letter denotes the component at the reference station and the second denotes the component at the field station. The station identities and observational coordinates are therefore fixed, while the virtual-source roles change with lag:

	propagation direction	effective source	effective receiver
$+$ lag	$\mathrm{ref} \to \mathrm{fld}$	ref	fld
$-$ lag	$\mathrm{fld} \to \mathrm{ref}$	fld	ref.

This appendix establishes the following result. Under horizontal adiabaticity, weak anisotropy, weak quasi-degenerate coupling of the fundamental Rayleigh and Love branches, the near-common-wavenumber approximation specified below, and the two-mode approximation, the complete theoretical source-group-normalized ambient noise cross-correlation tensor, denoted by $\widetilde{\boldsymbol{C}}^{\pm}$, is determined to first order by the modal reference traces $TT^{\pm}$ and $ZZ^{\pm}$, the fixed-endpoint mixing coefficients $\chi_{\mathrm{ref}}, \chi_{\mathrm{fld}} \in \mathbb{C}$, and known ratios of the real reference surface eigenfunctions. The mixing coefficient for the fixed reference-to-field azimuth satisfies

$$\chi = \frac{E + \mathrm{i}X}{A - B} + \mathcal{O}(\epsilon^2), \qquad \chi \in \mathbb{C}, \quad A, B, E, X \in \mathbb{R}, \qquad \epsilon \in \mathbb{R}_{>0}, \tag{A.1}$$

where A, B, E, and X are depth integrals of the local elastic tensor and reference eigenfunctions. The X- and E-dominant limits of this result provide the working equations used in the main text.

The derivation introduces progressively more restrictive assumptions. We begin with a fixed-frequency adiabatic modal Green tensor expressed in terms of exact local anisotropic eigenfunctions. We then project those eigenfunctions onto the fundamental reference Rayleigh–Love subspace and derive their general first-order form. Section A3 adopts the two-mode approximation, after which all subsequent results use only the two fundamental branches for quasi-Rayleigh and quasi-Love waves. We then relate the mixing coefficient to the elastic tensor. Sections A5–A7 connect the positive-lag cross-correlation and Green tensors, apply the theoretical source-group normalization, derive all nine entries of the normalized tensor $\widetilde{\boldsymbol{C}}^{+}$, and specialize to the X- and E-dominant regimes. Section A8 treats propagation in the reverse direction, $\mathrm{fld} \to \mathrm{ref}$. The natural propagation-oriented horizontal basis reverses in that direction, but all final negative-lag cross-correlation components are expressed in the same fixed observational R, T, Z coordinates used at positive lag.

A1 Adiabatic modal Green tensor

Surface-wave propagation in slowly varying media has been studied extensively, including for isotropic media by Woodhouse (1974) and Tromp & Dahlen (1992) and for anisotropic media by Tanimoto (1987) and Tromp & Dahlen (1993). Motivated particularly by Tromp & Dahlen (1993) and Tromp (1994b), we adopt a related form for the far-field frequency-domain Green tensor, with normalization and propagation factors chosen to preserve Green-tensor reciprocity under the approximations introduced below. At angular frequency $\omega \in \mathbb{R}_{>0}$, the far-field frequency-domain Green tensor $\boldsymbol{G}(\omega) \in \mathbb{C}^{3\times 3}$ for surface-wave propagation through a smoothly varying anisotropic medium may be represented as a sum over local surface-wave branches:

$$G_{YX}(\boldsymbol{x}_{\mathrm{fld}}, \boldsymbol{x}_{\mathrm{ref}}, \omega) \simeq \sum_{\nu} \frac{[\boldsymbol{p}_{\nu,\mathrm{fld}}(0)]_Y [\boldsymbol{p}_{\nu,\mathrm{ref}}(0)]^*_X}{I_{1\nu} D_\nu} \exp(\mathrm{i}\Phi_\nu). \tag{A.2}$$

Equation (A.2) is written for the positive-lag propagation direction $\mathrm{ref} \to \mathrm{fld}$. Its dyadic form explicitly incorporates the local polarization eigenvectors at both endpoints, providing the basis for estimating polarization parameters at both the reference and field stations. The Green-tensor element G_{YX} is displacement in direction Y at the field station produced by a force in direction X at the reference station, with $X, Y \in \{R, T, Z\}$. The asterisk denotes complex conjugation. The modal branch label ν ranges over the local surface-wave modes, $j \in \{\mathrm{ref}, \mathrm{fld}\}$ labels a fixed endpoint, and $\boldsymbol{p}_{\nu,j}(z) \in \mathcal{H}$ is the exact local anisotropic eigenfunction of branch ν at endpoint j, evaluated at the surface in equation (A.2). Here $\mathcal{H}$ is the Hilbert space of admissible depth-dependent, three-component displacement eigenfunctions for the local one-dimensional surface-wave eigenproblem, equipped with the common density-weighted modal inner product defined below. In this appendix, "exact local" means exact for the one-dimensional depth-dependent anisotropic eigenproblem associated with the local medium; it does not mean exact for the full laterally varying three-dimensional wave equation. We do not include attenuation terms in Equation (A.2) because the subsequent normalization removes the absolute amplitude information associated with attenuation. In addition, to first order, we assume that the quality factors of the quasi-Love and quasi-Rayleigh waves are comparable to first-order.

The real, positive modal normalization factor $I_{1\nu} \in \mathbb{R}_{>0}$ is

$$\begin{aligned} I_{1\nu}(\boldsymbol{x}_{\mathrm{fld}}, \boldsymbol{x}_{\mathrm{ref}}, \omega) &= \left[I^{\mathrm{fld}}_{1\nu} I^{\mathrm{ref}}_{1\nu} \right]^{1/2} \\ &= \left[\left\{ \int_0^\infty \rho_{\mathrm{fld}}(z)\, \boldsymbol{p}^\dagger_{\nu,\mathrm{fld}}(z) \boldsymbol{p}_{\nu,\mathrm{fld}}(z)\, \mathrm{d}z \right\} \left\{ \int_0^\infty \rho_{\mathrm{ref}}(z)\, \boldsymbol{p}^\dagger_{\nu,\mathrm{ref}}(z) \boldsymbol{p}_{\nu,\mathrm{ref}}(z)\, \mathrm{d}z \right\} \right]^{1/2}. \end{aligned} \tag{A.3}$$

where $\rho(z) \in \mathbb{R}_{>0}$ is density and $\dagger$ denotes conjugate transpose. The propagation factor $D_\nu \in \mathbb{R}_{>0}$ contains the phase- and group-velocity and geometrical-spreading factors appropriate to the branch.

With the convention used in the present manuscript,

$$\begin{aligned} D_\nu(\boldsymbol{x}_{\rm fld}, \boldsymbol{x}_{\rm ref}, \omega) &= \left[D_\nu^{\rm fld} D_\nu^{\rm ref}\right]^{1/2} \\ &= \left[\left\{4c_\nu^{\rm fld} G_\nu^{\rm fld}\left(\frac{k_\nu^{\rm fld}\pi}{2}\zeta_\nu^{\rm fld}\right)^{1/2}\right\}\left\{4c_\nu^{\rm ref} G_\nu^{\rm ref}\left(\frac{k_\nu^{\rm ref}\pi}{2}\zeta_\nu^{\rm ref}\right)^{1/2}\right\}\right]^{1/2}. \end{aligned} \tag{A.4}$$

where $k_\nu, c_\nu, G_\nu, \zeta_\nu \in \mathbb{R}_{>0}$ denote the local wavenumber, phase velocity, group velocity, and geometrical spreading distance, respectively. In principle, the quasi-Love and quasi-Rayleigh waves may follow different propagation paths and therefore have different geometrical spreading. Here we adopt a common-path approximation in which both propagate along the great-circle path connecting the reference and field stations. The geometrical spreading distance is then the inter-station distance and is invariant under interchange of the reference and field endpoints. The quasi-Love and quasi-Rayleigh propagation factors may nevertheless differ through their wavenumbers, phase velocities, and group velocities. The modal phase $\Phi_\nu \in \mathbb{R}$ is

$$\Phi_\nu = \int_{\boldsymbol{x}_{\rm ref}}^{\boldsymbol{x}_{\rm fld}} \boldsymbol{k}_\nu \cdot \mathrm{d}\boldsymbol{x} + \gamma_\nu + \frac{\pi}{4}, \tag{A.5}$$

where $\boldsymbol{k}_\nu \in \mathbb{R}^2$ is the local horizontal wavevector and $\gamma_\nu \in \mathbb{R}$ is the geometric (Berry) phase. The specific allocation of slowly varying normalization factors between $I_{1\nu}$, D_ν, and $\boldsymbol{p}_\nu$ is conventional; only their consistent product in equation (A.2) is physically meaningful. These definitions ensure that the Green tensor satisfies reciprocity for the reciprocal elastic medium considered here,

$$G_{YX}(\boldsymbol{x}_{\rm fld}, \boldsymbol{x}_{\rm ref}, \omega) = G_{XY}(\boldsymbol{x}_{\rm ref}, \boldsymbol{x}_{\rm fld}, \omega).$$

Equation (A.2) is written at fixed ω. In the isotropic, horizontally homogeneous limit, equation (A.2) reduces to the standard far-field surface-wave Green tensor (e.g., Aki & Richards, 2002). The local wavenumber and polarization eigenfunction of each branch are therefore evaluated on its local dispersion relation, $k_\nu = k_\nu(\omega)$. The coupling calculation below is formulated at a nearly common reference wavenumber k_0, where the reference fundamental Rayleigh and Love branches are close in frequency. Applying that result to equation (A.2) assumes that the mixing coefficient and the reference eigenfunctions vary negligibly over the small wavenumber separation between the two branches at the specified frequency. This approximation is distinct from horizontal adiabaticity and should be checked numerically where the branch separation is not small.

The adiabatic assumption in equation (A.2) is a propagation assumption: a wave remains on a continuously followed local branch as the medium varies horizontally, with negligible conversion to

other branches caused by rapid lateral variation. A useful operational scale-separation condition is

$$\frac{\ell_{\mathrm{structure}}}{\lambda_{\mathrm{wave}}} \gg 1. \tag{A.6}$$

This condition is a practical guide rather than a necessary or complete criterion for adiabaticity. The fuller condition also depends on the magnitude of the polarization change and the separation of neighboring modal branches, as discussed in Section 6.1 and the Supplementary Materials. It is not itself a two-mode assumption. At this stage, the sum in equation (A.2) may include all quasi-Rayleigh and quasi-Love branches needed to represent the local wavefield. Thus Section A1 establishes the fixed-frequency propagation framework without yet restricting the local eigenfunctions to a two-mode subspace.

A2 Local reference Rayleigh and Love modes

At each horizontal position, the local reference modes $\boldsymbol{p}_n^0 \in \mathcal{H}$ are defined by a one-dimensional, lossless eigenproblem at horizontal wavenumber $k \in \mathbb{R}_{>0}$,

$$\mathcal{L}_0(k)\boldsymbol{p}_n^0 = [\omega_n^0(k)]^2 \boldsymbol{p}_n^0. \tag{A.7}$$

Here $\mathcal{L}_0(k) : \mathcal{H} \to \mathcal{H}$ denotes the operator for the local isotropic or vertically transversely isotropic reference medium. The reference and local anisotropic eigenproblems are assumed to share the same density profile (equivalently, the same mass operator) and to be self-adjoint with respect to the common density-weighted modal inner product

$$\langle \boldsymbol{p}, \boldsymbol{q} \rangle_0 \equiv \int_0^\infty \rho(z)\, \boldsymbol{p}^\dagger(z)\boldsymbol{q}(z)\, \mathrm{d}z, \qquad \langle \boldsymbol{p}_m^0, \boldsymbol{p}_n^0 \rangle_0 = \delta_{mn}, \tag{A.8}$$

where $\boldsymbol{p}, \boldsymbol{q} \in \mathcal{H}$. This common inner product supplies the orthogonality and projection relations used below.

The fundamental reference Love and Rayleigh eigenfunctions are evaluated near a common wavenumber k_0, with $k_0 \in \mathbb{R}_{>0}$, at which the two branches are close enough in eigenfrequency for quasi-degenerate coupling to be important. In the (R, T, Z) component order and with the phase convention used here,

$$\boldsymbol{p}_L^0(z; k_0) = \begin{pmatrix} 0 \\ W(z; k_0) \\ 0 \end{pmatrix}, \qquad \boldsymbol{p}_R^0(z; k_0) = \begin{pmatrix} V(z; k_0) \\ 0 \\ \mathrm{i}U(z; k_0) \end{pmatrix}. \tag{A.9}$$

The functions $U, V, W \in \mathbb{R}$ under the adopted phase convention; U and V are the vertical and radial Rayleigh-wave eigenfunctions, respectively, and W is the transverse Love-wave eigenfunction. Their local values at the reference and field stations are denoted by $U_{\mathrm{ref}}, V_{\mathrm{ref}}, W_{\mathrm{ref}}$ and $U_{\mathrm{fld}}, V_{\mathrm{fld}}, W_{\mathrm{fld}}$,

respectively; throughout, an omitted depth argument on an endpoint eigenfunction denotes its surface value at $z = 0$.

For the displacement normalization used in the current manuscript, equation (A.8) reduces for the two fundamental modes to

$$\int_0^\infty \rho W^2 \, \mathrm{d}z = 1, \qquad \int_0^\infty \rho (U^2 + V^2) \, \mathrm{d}z = 1. \tag{A.10}$$

The retained fundamental Rayleigh–Love subspace $\mathcal{S}_0(k_0) \subset \mathcal{H}$ is

$$\mathcal{S}_0(k_0) = \mathrm{span}\{\boldsymbol{p}_L^0, \boldsymbol{p}_R^0\}, \tag{A.11}$$

and $P_0 : \mathcal{H} \to \mathcal{S}_0$ denotes the orthogonal projection onto $\mathcal{S}_0$ in the inner product $\langle \cdot, \cdot \rangle_0$.

The exact local anisotropic modes used below are solutions of the corresponding depth-dependent anisotropic eigenproblem at the same local horizontal position and reference wavenumber. They are labeled qL and qR by continuous branch continuation and dominant projection onto the reference fundamental Love and Rayleigh modes.

A3 Projection and the two-mode approximation

Let $\boldsymbol{p}_{qL}, \boldsymbol{p}_{qR} \in \mathcal{H}$ be the normalized exact local anisotropic eigenfunctions identified by continuous branch continuation and dominant projection as quasi-Love and quasi-Rayleigh, respectively. Their exact orthogonal decompositions with respect to the fundamental reference subspace $\mathcal{S}_0$ are

$$\boldsymbol{p}_{qL} = a_L \boldsymbol{p}_L^0 + b_L \boldsymbol{p}_R^0 + \boldsymbol{\eta}^L, \tag{A.12}$$

$$\boldsymbol{p}_{qR} = a_R \boldsymbol{p}_R^0 + b_R \boldsymbol{p}_L^0 + \boldsymbol{\eta}^R, \tag{A.13}$$

where $a_L, a_R, b_L, b_R \in \mathbb{C}$ and $\boldsymbol{\eta}^L, \boldsymbol{\eta}^R \in \mathcal{S}_0^\perp$, where $\mathcal{S}_0^\perp$ denotes the space perpendicular to the subspace $\mathcal{S}_0$. These are exact projection identities, not perturbative ansatzes (e.g. Park 1990). The residuals describe local eigenfunction structure outside the fundamental Rayleigh–Love subspace and are distinct from path-dependent nonadiabatic mode conversion.

Because the local anisotropic eigenproblem is lossless and self-adjoint, the exact modes may be normalized and chosen mutually orthogonal. Equations (A.8), (A.12), and (A.13) then give

$$|a_L|^2 + |b_L|^2 + \left\|\boldsymbol{\eta}^L\right\|_0^2 = 1, \tag{A.14}$$

$$|a_R|^2 + |b_R|^2 + \left\|\boldsymbol{\eta}^R\right\|_0^2 = 1, \tag{A.15}$$

$$a_L^* b_R + b_L^* a_R + \left\langle \boldsymbol{\eta}^L, \boldsymbol{\eta}^R \right\rangle_0 = 0. \tag{A.16}$$

Here and below, the subscript 0 on $\|\cdot\|_0$ and $\langle \cdot, \cdot \rangle_0$ denotes the norm and inner product associated

with the density-weighted reference inner product defined in equation (A.8); it is not a subscript on the residual vectors $\boldsymbol{\eta}^L$ or $\boldsymbol{\eta}^R$.

Introduce a dimensionless perturbation parameter $\epsilon \in \mathbb{R}_{>0}$, $\epsilon \ll 1$, and assume

$$b_L, b_R = \mathcal{O}(\epsilon), \qquad \left\|\boldsymbol{\eta}^L\right\|_0, \left\|\boldsymbol{\eta}^R\right\|_0 = \mathcal{O}(\epsilon). \tag{A.17}$$

Normalization, together with a phase convention in which the dominant projection coefficients are real and positive, yields

$$a_L = a_R = 1 + \mathcal{O}(\epsilon^2), \qquad b_R = -b_L^* + \mathcal{O}(\epsilon^2). \tag{A.18}$$

Defining the complex mixing coefficient $\chi \equiv b_L \in \mathbb{C}$, the local anisotropic eigenfunctions are therefore

$$\boldsymbol{p}_{qL} = \boldsymbol{p}_L^0 + \chi \boldsymbol{p}_R^0 + \boldsymbol{\eta}^L + \mathcal{O}(\epsilon^2), \tag{A.19}$$

$$\boldsymbol{p}_{qR} = \boldsymbol{p}_R^0 - \chi^* \boldsymbol{p}_L^0 + \boldsymbol{\eta}^R + \mathcal{O}(\epsilon^2). \tag{A.20}$$

If the residuals contribute at first order at the surface, the two branch polarizations acquire independent corrections and cannot be represented by a single mixing coefficient χ.

For the remainder of this appendix we adopt the two-mode approximation

$$\boldsymbol{\eta}^L = \mathcal{O}(\epsilon^2), \qquad \boldsymbol{\eta}^R = \mathcal{O}(\epsilon^2), \tag{A.21}$$

so that

$$\boldsymbol{p}_{qL} = \boldsymbol{p}_L^0 + \chi \boldsymbol{p}_R^0 + \mathcal{O}(\epsilon^2), \tag{A.22}$$

$$\boldsymbol{p}_{qR} = \boldsymbol{p}_R^0 - \chi^* \boldsymbol{p}_L^0 + \mathcal{O}(\epsilon^2). \tag{A.23}$$

The residuals need not vanish; equation (A.21) states that they do not contribute to the first-order theory. Equations (A.22) and (A.23) define the two-mode eigenvectors used below.

A4 Rayleigh–Love coupling and dependence on the elastic tensor

The quasi-degenerate coupling of fundamental Rayleigh and Love waves in a weakly anisotropic medium was developed in detail by Liu & Ritzwoller (2025). We use only the first-order result required here. Within the two-mode approximation, at a nearly common reference wavenumber k_0, the mixing coefficient $\chi \in \mathbb{C}$ is

$$\chi = \frac{E + \mathrm{i}X}{A - B} + \mathcal{O}(\epsilon^2), \tag{A.24}$$

where $A, B, E, X \in \mathbb{R}$ are depth integrals of the local elastic tensor and the reference fundamental eigenfunctions at k_0. Equation (A.24) assumes weak modal mixing,

$$\left|\frac{E+\mathrm{i}X}{A-B}\right| \ll 1, \tag{A.25}$$

and is not valid arbitrarily close to $A = B$. To first order, we write

$$\begin{aligned}
&\chi = \widetilde{\Gamma}\exp(\mathrm{i}\phi), \qquad \widetilde{\Gamma} \equiv \left|\frac{E+\mathrm{i}X}{A-B}\right| = \frac{\sqrt{E^2+X^2}}{|A-B|} \in \mathbb{R}_{\geq 0}, \\
&\phi \equiv \operatorname{atan2}\!\left(\frac{X}{A-B}, \frac{E}{A-B}\right) \pmod{2\pi}.
\end{aligned} \tag{A.26}$$

This polar representation separates the nonnegative magnitude $\widetilde{\Gamma}$ of the leading-order mixing coefficient from its phase ϕ. When $E = X = 0$, $\widetilde{\Gamma} = 0$ and ϕ is undefined but physically immaterial. In the limiting regimes used below, it is more convenient to fix the phase and absorb the possible sign into a real polarization parameter Γ: in the X-dominant regime $\chi = \mathrm{i}\Gamma$ with $\Gamma = X/(A-B)$, whereas in the E-dominant regime $\chi = \Gamma$ with $\Gamma = E/(A-B)$. Equivalently, changing the sign of Γ shifts ϕ by π. Because A, B, E, and X have identical dimensions, χ, $\widetilde{\Gamma}$, and Γ are dimensionless.

With $\psi \in \mathbb{R}$ denoting the fixed reference-to-field azimuth and a prime denoting $\mathrm{d}/\mathrm{d}z$, Liu and Ritzwoller (2025) present expressions for A, B, E, and X.

$$\begin{aligned}
A(\psi) = k^2 \int_0^\infty \mathrm{d}z \Bigg[&(\mathcal{N} - E_c\cos 4\psi + E_s \sin 4\psi)\, W^2 \\
&+ (\mathcal{L} - G_c \cos 2\psi + G_s \sin 2\psi)\, \frac{W'^2}{k^2} \Bigg],
\end{aligned} \tag{A.27}$$

$$\begin{aligned}
B(\psi) = k^2 \int_0^\infty \mathrm{d}z \Bigg[&(\mathcal{A} + B_c\cos 2\psi - B_s \sin 2\psi + E_c \cos 4\psi - E_s \sin 4\psi)\, V^2 \\
&+ (\mathcal{L} + G_c \cos 2\psi - G_s \sin 2\psi) \left(U - \frac{V'}{k}\right)^2 \\
&+ 2\,(\mathcal{F} + H_c \cos 2\psi - H_s \sin 2\psi)\, V \frac{U'}{k} + \mathcal{C}\frac{U'^2}{k^2} \Bigg],
\end{aligned} \tag{A.28}$$

$$\begin{aligned}
E(\psi) = k^2 \int_0^\infty \mathrm{d}z \Bigg[&\left(-\frac{1}{2}B_c \sin 2\psi - \frac{1}{2}B_s \cos 2\psi - E_c \sin 4\psi - E_s \cos 4\psi\right) WV \\
&+ (G_c \sin 2\psi + G_s \cos 2\psi) \left(U - \frac{V'}{k}\right) \frac{W'}{k} \\
&- (H_c \sin 2\psi + H_s \cos 2\psi)\, W \frac{U'}{k} \Bigg],
\end{aligned} \tag{A.29}$$

$$X(\psi) = k^2 \int_0^\infty \mathrm{d}z \left\{ \left[2(J_c - M_c)\sin\psi - 2(J_s + M_s)\cos\psi + D_c \sin 3\psi - D_s \cos 3\psi\right] V \frac{W'}{k} \right.$$
$$+ \left[M_c \sin\psi + M_s \cos\psi + D_c \sin 3\psi - D_s \cos 3\psi\right] W \left(U - \frac{V'}{k}\right)$$
$$\left. + 2\left[(J_c - K_c)\sin\psi - (J_s - K_s)\cos\psi\right] \frac{W'U'}{k^2} \right\}. \tag{A.30}$$

Here $\mathcal{A}, \mathcal{C}, \mathcal{N}, \mathcal{L}$, and $\mathcal{F}$ denote the azimuthally averaged elastic combinations used to construct the reference VTI medium, while $B_{c,s}, D_{c,s}, E_{c,s}, G_{c,s}, H_{c,s}, J_{c,s}, K_{c,s}$, and $M_{c,s}$ are the anisotropic elastic parameters defined in Section 3 of the Supplementary Materials. Calligraphic symbols are used for the azimuthally averaged elastic combinations to distinguish them from the coupling integrals A and B.

The four integrals have identical dimensions, and their common modal normalization cancels in the dimensionless ratio in equation (A.24). Equations (A.27)–(A.30), together with equation (A.24), therefore provide the forward relation from the local elastic tensor to the first-order quasi-Rayleigh and quasi-Love polarization. The X- and E-dominant regimes considered later are limiting phase regimes of this single complex mixing coefficient.

A5 Adiabatic cross-correlation tensor and source-group normalization: positive correlation lag

We first consider positive correlation lag, for which propagation is $\mathrm{ref} \rightarrow \mathrm{fld}$. The reference station is the effective source and the field station is the effective receiver. Superscripts $+$ and $-$ are reserved for quantities that genuinely depend on correlation lag or propagation direction, principally the cross-correlation time series and modal phases. Fixed endpoint quantities are identified instead by the subscripts ref and fld.

For this propagation direction, at endpoint $j \in \{\mathrm{ref}, \mathrm{fld}\}$, equations (A.22), (A.23), and (A.26), together with the reference eigenfunctions in equation (A.9), give the surface eigenvectors

$$\boldsymbol{p}^+_{qL,j}(0) = \begin{pmatrix} \chi_j V_j \\ W_j \\ \mathrm{i}\chi_j U_j \end{pmatrix} + \mathcal{O}(\epsilon^2), \tag{A.31}$$

$$\boldsymbol{p}^+_{qR,j}(0) = \begin{pmatrix} V_j \\ -\chi_j^* W_j \\ \mathrm{i}U_j \end{pmatrix} + \mathcal{O}(\epsilon^2), \tag{A.32}$$

where $j \in \{\mathrm{ref}, \mathrm{fld}\}$ and $\chi_j \in \mathbb{C}$ is

$$\chi_j = \widetilde{\Gamma}_j \exp(\mathrm{i}\phi_j), \qquad \widetilde{\Gamma}_j = |\chi_j| \geq 0. \tag{A.33}$$

A5.1 Cross-correlation–Green-tensor correspondence

All results from this point onward use the two-mode approximation adopted in Section A3. Under the assumptions commonly adopted in ambient-noise interferometry, an appropriate noise-source distribution allows the cross-correlation tensor to retrieve the corresponding Green tensor (e.g., Wapenaar, 2004). For the present treatment, we further assume that, for an uneven noise-source distribution, the positive- and negative-lag cross-correlations remain proportional to the corresponding Green tensors, with their asymmetry represented by different source-strength factors associated with the radial, transverse, and vertical effective source directions. The noise source distribution can have a large impact on the extracted Green's function (e.g. Cupillard & Capdeville 2010; Weaver 2011; Tsai 2009, 2010, 2011 and many others) so more sophositicated theory and data processing could be done in the future. With $\boldsymbol{C}(\omega), \boldsymbol{G}(\omega) \in \mathbb{C}^{3\times3}$, $\Lambda \in \mathbb{C}$, and $F_{R,\mathrm{ref}}, F_{T,\mathrm{ref}}, F_{Z,\mathrm{ref}} \in \mathbb{R}_{\geq 0}$, we write

$$\boldsymbol{C}^{+}(\omega) = \begin{pmatrix} RR^{+} & TR^{+} & ZR^{+} \\ RT^{+} & TT^{+} & ZT^{+} \\ RZ^{+} & TZ^{+} & ZZ^{+} \end{pmatrix} \simeq \Lambda \begin{pmatrix} G_{RR}F_{R,\mathrm{ref}} & G_{RT}F_{T,\mathrm{ref}} & G_{RZ}F_{Z,\mathrm{ref}} \\ G_{TR}F_{R,\mathrm{ref}} & G_{TT}F_{T,\mathrm{ref}} & G_{TZ}F_{Z,\mathrm{ref}} \\ G_{ZR}F_{R,\mathrm{ref}} & G_{ZT}F_{T,\mathrm{ref}} & G_{ZZ}F_{Z,\mathrm{ref}} \end{pmatrix} = \Lambda\, \boldsymbol{G}(\boldsymbol{x}_{\mathrm{fld}}, \boldsymbol{x}_{\mathrm{ref}}; \omega)\boldsymbol{F}_{\mathrm{ref}}, \tag{A.34}$$

where

$$\boldsymbol{F}_{\mathrm{ref}} = \mathrm{diag}(F_{R,\mathrm{ref}}, F_{T,\mathrm{ref}}, F_{Z,\mathrm{ref}}). \tag{A.35}$$

The matrix rows in equation (A.34) identify the component at the field station, whereas the columns identify the component at the reference station. In the component label XY, the first letter denotes the reference-station component and the second denotes the field-station component. At positive lag these fixed station identities coincide with the effective source and receiver roles; for example, TZ^{+} denotes vertical displacement at the field station produced by a transverse effective source at the reference station. The factor Λ converts the ambient noise cross-correlation convention to the Green-tensor convention and may be complex. Its value is not required because it cancels under the source-group normalization below.

Using equation (A.2) and retaining only the fundamental quasi-Love and quasi-Rayleigh branches, an unnormalized component is

$$C^{+}_{XY} \simeq \Lambda F_{X,\mathrm{ref}} \left[\frac{(p_{qL,\mathrm{fld}})_Y (p_{qL,\mathrm{ref}})^{*}_X}{I_{1qL} D_{qL}} \exp(\mathrm{i}\Phi^{+}_{qL}) + \frac{(p_{qR,\mathrm{fld}})_Y (p_{qR,\mathrm{ref}})^{*}_X}{I_{1qR} D_{qR}} \exp(\mathrm{i}\Phi^{+}_{qR}) \right]. \tag{A.36}$$

In addition to the two-mode representation of the local eigenfunctions adopted in Section A3, we now truncate the modal sum in equation (A.2) to the fundamental quasi-Love and quasi-Rayleigh branches. These assumptions are physically related but logically distinct. Because the retained modes are normalized and their first-order corrections are orthogonal to the dominant reference modes,

$$I_{1qL} = 1 + \mathcal{O}(\epsilon^2), \qquad I_{1qR} = 1 + \mathcal{O}(\epsilon^2), \tag{A.37}$$

and these factors may be replaced by unity in the first-order tensor calculation.

A5.2 Cross-correlation tensor before source-group normalization

Before applying the source-group normalization, we write the individual components of the cross-correlation tensor explicitly. Substitution of the first-order two-mode eigenvectors in equations (A.22) and (A.23) into equation (A.36), with the modal normalization factors replaced by unity according to equation (A.37), gives the sum of the quasi-Love and quasi-Rayleigh contributions to each component. Products containing two mixing coefficients are $\mathcal{O}(\epsilon^2)$ and are omitted.

For a transverse source and transverse receiver,

$$\begin{aligned} TT^+ &= \Lambda F_{T,\mathrm{ref}} \left[\frac{(\boldsymbol{p}_{qL,\mathrm{fld}})_T (\boldsymbol{p}_{qL,\mathrm{ref}})_T^*}{D_{qL}} \exp(\mathrm{i}\Phi_{qL}^+) + \frac{(\boldsymbol{p}_{qR,\mathrm{fld}})_T (\boldsymbol{p}_{qR,\mathrm{ref}})_T^*}{D_{qR}} \exp(\mathrm{i}\Phi_{qR}^+) \right] \\ &= \Lambda F_{T,\mathrm{ref}} \frac{W_{\mathrm{fld}} W_{\mathrm{ref}}}{D_{qL}} \exp(\mathrm{i}\Phi_{qL}^+) + \mathcal{O}(\epsilon^2). \end{aligned} \tag{A.38}$$

Similarly, the vertical–vertical and radial–radial components are

$$\begin{aligned} ZZ^+ &= \Lambda F_{Z,\mathrm{ref}} \left[\frac{(\boldsymbol{p}_{qL,\mathrm{fld}})_Z (\boldsymbol{p}_{qL,\mathrm{ref}})_Z^*}{D_{qL}} \exp(\mathrm{i}\Phi_{qL}^+) + \frac{(\boldsymbol{p}_{qR,\mathrm{fld}})_Z (\boldsymbol{p}_{qR,\mathrm{ref}})_Z^*}{D_{qR}} \exp(\mathrm{i}\Phi_{qR}^+) \right] \\ &= \Lambda F_{Z,\mathrm{ref}} \frac{U_{\mathrm{fld}} U_{\mathrm{ref}}}{D_{qR}} \exp(\mathrm{i}\Phi_{qR}^+) + \mathcal{O}(\epsilon^2), \end{aligned} \tag{A.39}$$

$$\begin{aligned} RR^+ &= \Lambda F_{R,\mathrm{ref}} \left[\frac{(\boldsymbol{p}_{qL,\mathrm{fld}})_R (\boldsymbol{p}_{qL,\mathrm{ref}})_R^*}{D_{qL}} \exp(\mathrm{i}\Phi_{qL}^+) + \frac{(\boldsymbol{p}_{qR,\mathrm{fld}})_R (\boldsymbol{p}_{qR,\mathrm{ref}})_R^*}{D_{qR}} \exp(\mathrm{i}\Phi_{qR}^+) \right] \\ &= \Lambda F_{R,\mathrm{ref}} \frac{V_{\mathrm{fld}} V_{\mathrm{ref}}}{D_{qR}} \exp(\mathrm{i}\Phi_{qR}^+) + \mathcal{O}(\epsilon^2). \end{aligned} \tag{A.40}$$

The radial–vertical components are also zeroth-order quasi-Rayleigh quantities:

$$\begin{aligned} ZR^+ &= \Lambda F_{Z,\mathrm{ref}} \left[\frac{(\boldsymbol{p}_{qL,\mathrm{fld}})_R (\boldsymbol{p}_{qL,\mathrm{ref}})_Z^*}{D_{qL}} \exp(\mathrm{i}\Phi_{qL}^+) + \frac{(\boldsymbol{p}_{qR,\mathrm{fld}})_R (\boldsymbol{p}_{qR,\mathrm{ref}})_Z^*}{D_{qR}} \exp(\mathrm{i}\Phi_{qR}^+) \right] \\ &= -\mathrm{i}\Lambda F_{Z,\mathrm{ref}} \frac{V_{\mathrm{fld}} U_{\mathrm{ref}}}{D_{qR}} \exp(\mathrm{i}\Phi_{qR}^+) + \mathcal{O}(\epsilon^2), \end{aligned} \tag{A.41}$$

$$\begin{aligned} RZ^+ &= \Lambda F_{R,\mathrm{ref}} \left[\frac{(\boldsymbol{p}_{qL,\mathrm{fld}})_Z (\boldsymbol{p}_{qL,\mathrm{ref}})_R^*}{D_{qL}} \exp(\mathrm{i}\Phi_{qL}^+) + \frac{(\boldsymbol{p}_{qR,\mathrm{fld}})_Z (\boldsymbol{p}_{qR,\mathrm{ref}})_R^*}{D_{qR}} \exp(\mathrm{i}\Phi_{qR}^+) \right] \\ &= \mathrm{i}\Lambda F_{R,\mathrm{ref}} \frac{U_{\mathrm{fld}} V_{\mathrm{ref}}}{D_{qR}} \exp(\mathrm{i}\Phi_{qR}^+) + \mathcal{O}(\epsilon^2). \end{aligned} \tag{A.42}$$

In contrast, the transverse–vertical components contain first-order contributions from both quasi-Love and quasi-Rayleigh waves:

$$TZ^+ = \Lambda F_{T,\mathrm{ref}} \left[\frac{(\boldsymbol{p}_{qL,\mathrm{fld}})_Z (\boldsymbol{p}_{qL,\mathrm{ref}})_T^*}{D_{qL}} \exp(\mathrm{i}\Phi_{qL}^+) + \frac{(\boldsymbol{p}_{qR,\mathrm{fld}})_Z (\boldsymbol{p}_{qR,\mathrm{ref}})_T^*}{D_{qR}} \exp(\mathrm{i}\Phi_{qR}^+) \right]$$
$$= \mathrm{i}\Lambda F_{T,\mathrm{ref}} U_{\mathrm{fld}} W_{\mathrm{ref}} \left[\frac{\chi_{\mathrm{fld}}}{D_{qL}} \exp(\mathrm{i}\Phi_{qL}^+) - \frac{\chi_{\mathrm{ref}}}{D_{qR}} \exp(\mathrm{i}\Phi_{qR}^+) \right] + \mathcal{O}(\epsilon^2), \tag{A.43}$$

$$ZT^+ = \Lambda F_{Z,\mathrm{ref}} \left[\frac{(\boldsymbol{p}_{qL,\mathrm{fld}})_T (\boldsymbol{p}_{qL,\mathrm{ref}})_Z^*}{D_{qL}} \exp(\mathrm{i}\Phi_{qL}^+) + \frac{(\boldsymbol{p}_{qR,\mathrm{fld}})_T (\boldsymbol{p}_{qR,\mathrm{ref}})_Z^*}{D_{qR}} \exp(\mathrm{i}\Phi_{qR}^+) \right]$$
$$= \mathrm{i}\Lambda F_{Z,\mathrm{ref}} W_{\mathrm{fld}} U_{\mathrm{ref}} \left[-\frac{\chi_{\mathrm{ref}}^*}{D_{qL}} \exp(\mathrm{i}\Phi_{qL}^+) + \frac{\chi_{\mathrm{fld}}^*}{D_{qR}} \exp(\mathrm{i}\Phi_{qR}^+) \right] + \mathcal{O}(\epsilon^2). \tag{A.44}$$

The remaining transverse–radial components are

$$TR^+ = \Lambda F_{T,\mathrm{ref}} \left[\frac{(\boldsymbol{p}_{qL,\mathrm{fld}})_R (\boldsymbol{p}_{qL,\mathrm{ref}})_T^*}{D_{qL}} \exp(\mathrm{i}\Phi_{qL}^+) + \frac{(\boldsymbol{p}_{qR,\mathrm{fld}})_R (\boldsymbol{p}_{qR,\mathrm{ref}})_T^*}{D_{qR}} \exp(\mathrm{i}\Phi_{qR}^+) \right]$$
$$= \Lambda F_{T,\mathrm{ref}} V_{\mathrm{fld}} W_{\mathrm{ref}} \left[\frac{\chi_{\mathrm{fld}}}{D_{qL}} \exp(\mathrm{i}\Phi_{qL}^+) - \frac{\chi_{\mathrm{ref}}}{D_{qR}} \exp(\mathrm{i}\Phi_{qR}^+) \right] + \mathcal{O}(\epsilon^2), \tag{A.45}$$

$$RT^+ = \Lambda F_{R,\mathrm{ref}} \left[\frac{(\boldsymbol{p}_{qL,\mathrm{fld}})_T (\boldsymbol{p}_{qL,\mathrm{ref}})_R^*}{D_{qL}} \exp(\mathrm{i}\Phi_{qL}^+) + \frac{(\boldsymbol{p}_{qR,\mathrm{fld}})_T (\boldsymbol{p}_{qR,\mathrm{ref}})_R^*}{D_{qR}} \exp(\mathrm{i}\Phi_{qR}^+) \right]$$
$$= \Lambda F_{R,\mathrm{ref}} W_{\mathrm{fld}} V_{\mathrm{ref}} \left[\frac{\chi_{\mathrm{ref}}^*}{D_{qL}} \exp(\mathrm{i}\Phi_{qL}^+) - \frac{\chi_{\mathrm{fld}}^*}{D_{qR}} \exp(\mathrm{i}\Phi_{qR}^+) \right] + \mathcal{O}(\epsilon^2). \tag{A.46}$$

Equations (A.38)–(A.46) show explicitly the modal content of the unnormalized cross-correlation tensor. To first order, TT contains only the quasi-Love branch, whereas ZZ, RR, ZR, and RZ contain only the quasi-Rayleigh branch. The polarization-sensitive components TZ, ZT, TR, and RT contain first-order contributions from both branches. They also retain the source-strength factor associated with their source direction and the distinct quasi-Love and quasi-Rayleigh propagation factors. Source-group normalization removes the former and, to first order in the polarization perturbation, eliminates the effect of the difference between the latter, as shown below.

A5.3 Theoretical source-group normalization

The source factors $F_{R,\mathrm{ref}}, F_{T,\mathrm{ref}}, F_{Z,\mathrm{ref}}$ and the conversion factor Λ are generally unknown. The theoretical source-group normalization removes them separately for each source direction. From the dominant unnormalized components in equations (A.38)–(A.40), the carrier-component amplitudes define

$$N_{T,\mathrm{ref}} \equiv \Lambda F_{T,\mathrm{ref}} \frac{W_{\mathrm{fld}} W_{\mathrm{ref}}}{D_{qL}}, \tag{A.47}$$

$$N_{Z,\mathrm{ref}} \equiv \Lambda F_{Z,\mathrm{ref}} \frac{U_{\mathrm{fld}} U_{\mathrm{ref}}}{D_{qR}}, \tag{A.48}$$

$$N_{R,\mathrm{ref}} \equiv \Lambda F_{R,\mathrm{ref}} \frac{V_{\mathrm{fld}} V_{\mathrm{ref}}}{D_{qR}}. \tag{A.49}$$

At positive lag the first fixed-station component index identifies the effective-source direction, so the source groups are $R : \{RR^+, RT^+, RZ^+\}$, $T : \{TR^+, TT^+, TZ^+\}$, and $Z : \{ZR^+, ZT^+, ZZ^+\}$. We denote the resulting source-group-normalized positive-lag tensor by $\widetilde{\boldsymbol{C}}^+$. The tilde is applied only to the tensor variable; its evaluated entries are written without tildes as RR^+, TT^+, ... Thus the entry labeled XY^+ in $\widetilde{\boldsymbol{C}}^+$ is obtained by dividing the corresponding unnormalized component C^+_{XY} by $N_{X,\mathrm{ref}}$, where $N_{X,\mathrm{ref}} = N_{R,\mathrm{ref}}$, $N_{T,\mathrm{ref}}$, or $N_{Z,\mathrm{ref}}$ according to the first fixed-station component index X.

The empirical source-group normalization described in Section 4.2 uses the observed carrier amplitude spectra within each narrow frequency band as proxies for the magnitudes of the corresponding theoretical normalization factors. It therefore approximates the theoretical normalization derived here. Any residual multiplicative factor common to every element of $\widetilde{\boldsymbol{C}}^+$ is immaterial for estimating Γ and is absorbed into the tensor convention.

The quasi-Love and quasi-Rayleigh propagation factors are generally unequal. Under the reciprocal common-path approximation used here, their positive amplitude factors are unchanged by reversal of propagation. We define their ratio as

$$\rho_D \equiv \frac{D_{qL}}{D_{qR}}. \tag{A.50}$$

The dimensionless quantity $\rho_D \in \mathbb{R}_{>0}$ is the quasi-Love–to–quasi-Rayleigh modal propagation-factor ratio. With the positive branch-normalization convention used here, D_{qL} and D_{qR}, and hence ρ_D, are real and positive. The two factors depend on phase velocity, group velocity, wavenumber, and geometrical spreading. At fixed frequency and for the common propagation geometry adopted here, equation (A.4) gives $D^j_\nu \propto G^j_\nu \sqrt{c^j_\nu}$ at each endpoint j, and hence $D_\nu \propto [G^{\mathrm{fld}}_\nu G^{\mathrm{ref}}_\nu]^{1/2} [c^{\mathrm{fld}}_\nu c^{\mathrm{ref}}_\nu]^{1/4}$. For the continental structures considered here, numerical calculations show that $\rho_D = 1 + \mathcal{O}(\epsilon)$. Because ρ_D enters the polarization-sensitive components only in products with the first-order mixing coefficient $\chi = \mathcal{O}(\epsilon)$, its departure from unity contributes only at second order:

$$\rho_D \chi = \chi + \mathcal{O}(\epsilon^2), \qquad (\rho_D)^{-1} \chi = \chi + \mathcal{O}(\epsilon^2). \tag{A.51}$$

We therefore omit ρ_D from the first-order polarization expressions below. Numerical calculations retaining the full propagation-factor ratio confirm that this approximation has negligible effect for the continental structures considered here.

A6 Cross-correlation tensor under the two-mode approximation: positive correlation lag

A6.1 Modal reference components

For a transverse source and transverse receiver, the quasi-Rayleigh contribution is quadratic in χ, so equations (A.38) and (A.47) give

$$TT^{+} = \exp(\mathrm{i}\Phi^{+}_{qL}) + \mathcal{O}(\epsilon^2). \tag{A.52}$$

Similarly, the quasi-Love contributions to ZZ^{+} and RR^{+} are quadratic, yielding

$$ZZ^{+} = \exp(\mathrm{i}\Phi^{+}_{qR}) + \mathcal{O}(\epsilon^2), \tag{A.53}$$

$$RR^{+} = \exp(\mathrm{i}\Phi^{+}_{qR}) + \mathcal{O}(\epsilon^2) = ZZ^{+} + \mathcal{O}(\epsilon^2). \tag{A.54}$$

The radial–vertical components are zeroth-order quasi-Rayleigh quantities. Substituting the two-mode surface eigenvectors in equations (A.31) and (A.32) into the two-branch cross-correlation expression (A.36), and applying the vertical- and radial-source-group normalizations in equations (A.48) and (A.49), gives

$$ZR^{+} = -\mathrm{i}\frac{V_{\mathrm{fld}}}{U_{\mathrm{fld}}}\, ZZ^{+} + \mathcal{O}(\epsilon^2), \tag{A.55}$$

$$RZ^{+} = \mathrm{i}\frac{U_{\mathrm{fld}}}{V_{\mathrm{fld}}}\, ZZ^{+} + \mathcal{O}(\epsilon^2). \tag{A.56}$$

The endpoint factors at the effective source (the reference station) cancel through source-group normalization, leaving only eigenfunction ratios at the effective receiver (the field station).

A6.2 Polarization-sensitive components

The TZ^{+} component contains a quasi-Love contribution controlled by the field-station mixing coefficient and a quasi-Rayleigh contribution controlled by the reference-station mixing coefficient. Retaining the distinct modal amplitude denominators gives

$$\begin{aligned} TZ^{+} &= \frac{U_{\mathrm{fld}}}{W_{\mathrm{fld}}}\left[\mathrm{i}\chi_{\mathrm{fld}}\, TT^{+} - \mathrm{i}\chi_{\mathrm{ref}}\, ZZ^{+}\right] + \mathcal{O}(\epsilon^2) \\ &= \frac{U_{\mathrm{fld}}}{W_{\mathrm{fld}}}\left[\mathrm{i}\widetilde{\Gamma}_{\mathrm{fld}} e^{\mathrm{i}\phi_{\mathrm{fld}}} TT^{+} - \mathrm{i}\widetilde{\Gamma}_{\mathrm{ref}} e^{\mathrm{i}\phi_{\mathrm{ref}}} ZZ^{+}\right] + \mathcal{O}(\epsilon^2). \end{aligned} \tag{A.57}$$

For the complementary ZT^{+} component,

$$\begin{aligned} ZT^{+} &= \frac{W_{\mathrm{fld}}}{U_{\mathrm{fld}}}\left[-\mathrm{i}\chi^{*}_{\mathrm{ref}}\, TT^{+} + \mathrm{i}\chi^{*}_{\mathrm{fld}}\, ZZ^{+}\right] + \mathcal{O}(\epsilon^2) \\ &= \frac{W_{\mathrm{fld}}}{U_{\mathrm{fld}}}\left[-\mathrm{i}\widetilde{\Gamma}_{\mathrm{ref}} e^{-\mathrm{i}\phi_{\mathrm{ref}}} TT^{+} + \mathrm{i}\widetilde{\Gamma}_{\mathrm{fld}} e^{-\mathrm{i}\phi_{\mathrm{fld}}} ZZ^{+}\right] + \mathcal{O}(\epsilon^2). \end{aligned} \tag{A.58}$$

The remaining transverse–radial components are

$$\begin{aligned} TR^{+} &= \frac{V_{\mathrm{fld}}}{W_{\mathrm{fld}}}\left[\chi_{\mathrm{fld}}\,TT^{+} - \chi_{\mathrm{ref}}\,ZZ^{+}\right] + \mathcal{O}(\epsilon^{2}) \\ &= \frac{V_{\mathrm{fld}}}{W_{\mathrm{fld}}}\left[\widetilde{\Gamma}_{\mathrm{fld}}e^{\mathrm{i}\phi_{\mathrm{fld}}}TT^{+} - \widetilde{\Gamma}_{\mathrm{ref}}e^{\mathrm{i}\phi_{\mathrm{ref}}}ZZ^{+}\right] + \mathcal{O}(\epsilon^{2}), \end{aligned} \tag{A.59}$$

$$\begin{aligned} RT^{+} &= \frac{W_{\mathrm{fld}}}{V_{\mathrm{fld}}}\left[\chi^{*}_{\mathrm{ref}}\,TT^{+} - \chi^{*}_{\mathrm{fld}}\,ZZ^{+}\right] + \mathcal{O}(\epsilon^{2}) \\ &= \frac{W_{\mathrm{fld}}}{V_{\mathrm{fld}}}\left[\widetilde{\Gamma}_{\mathrm{ref}}e^{-\mathrm{i}\phi_{\mathrm{ref}}}TT^{+} - \widetilde{\Gamma}_{\mathrm{fld}}e^{-\mathrm{i}\phi_{\mathrm{fld}}}ZZ^{+}\right] + \mathcal{O}(\epsilon^{2}). \end{aligned} \tag{A.60}$$

Equations (A.57)–(A.60) imply the useful proportionalities

$$TR^{+} = -\mathrm{i}\frac{V_{\mathrm{fld}}}{U_{\mathrm{fld}}}\,TZ^{+} + \mathcal{O}(\epsilon^{2}), \tag{A.61}$$

$$RT^{+} = \mathrm{i}\frac{U_{\mathrm{fld}}}{V_{\mathrm{fld}}}\,ZT^{+} + \mathcal{O}(\epsilon^{2}). \tag{A.62}$$

A6.3 Complete source-group-normalized tensor

Collecting equations (A.52)–(A.62), the complete first-order source-group-normalized positive-lag cross-correlation tensor is

$$\widetilde{\boldsymbol{C}}^{+} = \begin{pmatrix} ZZ^{+} & -\mathrm{i}\dfrac{V_{\mathrm{fld}}}{U_{\mathrm{fld}}}TZ^{+} & -\mathrm{i}\dfrac{V_{\mathrm{fld}}}{U_{\mathrm{fld}}}ZZ^{+} \\ \mathrm{i}\dfrac{U_{\mathrm{fld}}}{V_{\mathrm{fld}}}ZT^{+} & TT^{+} & ZT^{+} \\ \mathrm{i}\dfrac{U_{\mathrm{fld}}}{V_{\mathrm{fld}}}ZZ^{+} & TZ^{+} & ZZ^{+} \end{pmatrix} + \mathcal{O}(\epsilon^{2}), \tag{A.63}$$

where TZ^{+} and ZT^{+} are given explicitly by equations (A.57) and (A.58). The ordering of the entries is the same as that defined in equation (A.34). Thus $\widetilde{\boldsymbol{C}}^{+}$ is determined, to first order, by the two modal traces TT^{+} and ZZ^{+}, the endpoint mixing coefficients χ_{fld} and χ_{ref}, and the known reference eigenfunction ratios at the effective receiver, the field station.

The main text concentrates on TT^{+}, ZZ^{+}, TZ^{+}, and ZT^{+}; the remaining five components provide internal consistency relations and complete the tensor prediction.

A7 Principal working equations: positive correlation lag

The complete first-order tensor derived in Section A6 simplifies in two polarization regimes of practical importance. No further modal approximation is introduced. For an X-dominant first-order theory we require $X/(A-B) = \mathcal{O}(\epsilon)$ and $E/(A-B) = \mathcal{O}(\epsilon^{2})$; for an E-dominant theory we require $E/(A-B) = \mathcal{O}(\epsilon)$ and $X/(A-B) = \mathcal{O}(\epsilon^{2})$. If the smaller term is not second order, its contribution must be retained explicitly.

A7.1 X-dominant regime

In the asymptotic X-dominant regime, we replace the nonnegative magnitude $\widetilde{\Gamma}_j$ by the signed real polarization parameter $\Gamma_j = X_j/(A_j - B_j)$, thereby fixing the phase at $\pi/2$ and carrying its sign in Γ_j. Equation (A.24) then becomes

$$\chi_j = \mathrm{i}\Gamma_j + \mathcal{O}(\epsilon^2), \qquad \Gamma_j \equiv \frac{X_j}{A_j - B_j} \in \mathbb{R}, \tag{A.64}$$

where the sign of Γ_j is determined by the local elastic tensor, propagation azimuth, and branch convention. Because $\chi_j^* = -\mathrm{i}\Gamma_j$, the required factors are, explicitly, $\mathrm{i}\chi_j = -\Gamma_j$, $-\mathrm{i}\chi_j = +\Gamma_j$, $-\mathrm{i}\chi_j^* = -\Gamma_j$, and $\mathrm{i}\chi_j^* = +\Gamma_j$. Substituting these relations into equations (A.57) and (A.58) gives the principal X-dominant equations for a laterally varying medium:

$$\boxed{\begin{aligned} TZ^+ &= \frac{U_{\mathrm{fld}}}{W_{\mathrm{fld}}}\left(-\Gamma_{\mathrm{fld}} TT^+ + \Gamma_{\mathrm{ref}} ZZ^+\right) + \mathcal{O}(\epsilon^2), && \text{(A.65)} \\ ZT^+ &= \frac{W_{\mathrm{fld}}}{U_{\mathrm{fld}}}\left(-\Gamma_{\mathrm{ref}} TT^+ + \Gamma_{\mathrm{fld}} ZZ^+\right) + \mathcal{O}(\epsilon^2). && \text{(A.66)} \end{aligned}}$$

The field-station eigenfunction ratios multiply the complete reference–field waveform combinations, whereas Γ_{fld} and Γ_{ref} describe the local polarization coupling at the two fixed endpoints.

For a horizontally homogeneous medium, the local reference eigenfunctions and coupling parameters are identical at the reference and field stations,

$$U_{\mathrm{fld}} = U_{\mathrm{ref}} = U, \qquad W_{\mathrm{fld}} = W_{\mathrm{ref}} = W, \qquad \Gamma_{\mathrm{fld}} = \Gamma_{\mathrm{ref}} = \Gamma. \tag{A.67}$$

Equations (A.65) and (A.66) then reduce for a horizontally homogeneous X-dominant medium to

$$\boxed{\begin{aligned} TZ^+ &= \frac{U}{W}\,\Gamma\left(-TT^+ + ZZ^+\right) + \mathcal{O}(\epsilon^2), && \text{(A.68)} \\ ZT^+ &= \frac{W}{U}\,\Gamma\left(-TT^+ + ZZ^+\right) + \mathcal{O}(\epsilon^2). && \text{(A.69)} \end{aligned}}$$

The two components contain the same waveform combination but are scaled by reciprocal effective-receiver polarization factors and therefore are not, in general, equal.

A7.2 E-dominant regime

In the asymptotic E-dominant regime, we replace the nonnegative magnitude $\widetilde{\Gamma}_j$ by the signed real polarization parameter $\Gamma_j = E_j/(A_j - B_j)$, thereby fixing the phase at zero and carrying its sign in Γ_j. Equation (A.24) then becomes

$$\chi_j = \Gamma_j + \mathcal{O}(\epsilon^2), \qquad \Gamma_j \equiv \frac{E_j}{A_j - B_j} \in \mathbb{R}. \tag{A.70}$$

Because $\chi_j = \chi_j^* = \Gamma_j \in \mathbb{R}$, direct substitution into equations (A.57) and (A.58) supplies the corresponding explicit factors of $\pm$i and gives, for a horizontally heterogeneous E-dominant medium,

$$\boxed{\begin{aligned} TZ^+ &= \mathrm{i}\frac{U_{\mathrm{fld}}}{W_{\mathrm{fld}}}\left(\Gamma_{\mathrm{fld}} TT^+ - \Gamma_{\mathrm{ref}} ZZ^+\right) + \mathcal{O}(\epsilon^2), \qquad \text{(A.71)} \\ ZT^+ &= \mathrm{i}\frac{W_{\mathrm{fld}}}{U_{\mathrm{fld}}}\left(-\Gamma_{\mathrm{ref}} TT^+ + \Gamma_{\mathrm{fld}} ZZ^+\right) + \mathcal{O}(\epsilon^2). \qquad \text{(A.72)} \end{aligned}}$$

Relative to the X-dominant equations, the E-dominant coupling places the polarization-sensitive components in quadrature with the modal reference traces under the adopted phase convention.

For a horizontally homogeneous E-dominant medium,

$$\boxed{\begin{aligned} TZ^+ &= \mathrm{i}\frac{U}{W}\,\Gamma\left(TT^+ - ZZ^+\right) + \mathcal{O}(\epsilon^2), \qquad \text{(A.73)} \\ ZT^+ &= \mathrm{i}\frac{W}{U}\,\Gamma\left(-TT^+ + ZZ^+\right) + \mathcal{O}(\epsilon^2). \qquad \text{(A.74)} \end{aligned}}$$

As in the X-dominant case, horizontal homogeneity equates the endpoint eigenfunctions and coupling parameters, while the reciprocal effective-receiver polarization factors generally keep TZ^+ and ZT^+ distinct.

Equations (A.65)–(A.74) are the principal working equations. They connect the source-group-normalized tensor $\widetilde{\boldsymbol{C}}^+$ to signed local polarization parameters at the two fixed endpoints, Γ_{ref} and Γ_{fld}. The X-dominant form is expected to apply over most of the TTI models and parameter ranges considered in the main text, whereas the E-dominant form describes the limiting behavior when the symmetry axis approaches horizontal.

These equations complete the first-order relation between the elastic tensor and the source-group-normalized tensor $\widetilde{\boldsymbol{C}}^+$ used in the main text.

The equations in Sections A5–A7 apply to positive correlation lag, $\mathrm{ref} \to \mathrm{fld}$. At negative lag the virtual source moves to the field station and propagation is $\mathrm{fld} \to \mathrm{ref}$. The observational R, T, Z axes remain fixed; the reversal of the auxiliary propagation-oriented modal basis is incorporated before the negative-lag tensor is formed.

A8 Negative correlation lag

At negative correlation lag, propagation is $\mathrm{fld} \to \mathrm{ref}$: the field station is the effective source and the reference station is the effective receiver. The station identities and the observational R, T, Z coordinate system remain fixed, with $\hat{\boldsymbol{R}}$ directed from the reference station toward the field station.

Equation (A.2), however, was written in a propagation-oriented coordinate system, with the radial direction pointing from source to receiver. To apply the same modal Green-tensor representation to negative lag, with the source and receiver endpoints interchanged, we therefore introduce a temporary

propagation-oriented coordinate system (R', T', Z') for propagation from the field station to the reference station. Because the negative-lag propagation direction is opposite to the fixed observational radial direction, and because the transverse direction reverses with it, the two coordinate systems are related by

$$\hat{\boldsymbol{R}}' = -\hat{\boldsymbol{R}}, \qquad \hat{\boldsymbol{T}}' = -\hat{\boldsymbol{T}}, \qquad \hat{\boldsymbol{Z}}' = \hat{\boldsymbol{Z}}. \tag{A.75}$$

Thus equation (A.2) can be used for the reverse propagation direction in the primed system after interchanging the source and receiver endpoints. The primed coordinates are introduced only for this propagation-oriented modal construction; the final negative-lag Green and cross-correlation tensors will be expressed in the original fixed observational coordinates.

It is useful to write the coordinate transformation in matrix form. Define

$$\boldsymbol{S} \equiv \begin{pmatrix} -1 & 0 & 0 \\ 0 & -1 & 0 \\ 0 & 0 & 1 \end{pmatrix}.$$

If $\boldsymbol{v}'$ denotes the components of a physical vector in the primed (R', T', Z') basis and $\boldsymbol{v}$ denotes the components of the same vector in the fixed (R, T, Z) basis, then

$$\boldsymbol{v} = \boldsymbol{S}\,\boldsymbol{v}'.$$

The transformation therefore changes the signs of the radial and transverse components but leaves the vertical component unchanged.

The reverse propagation direction also changes the propagation azimuth from ψ to $\psi + \pi$. As shown explicitly in equations (A.90) and (A.91) below,

$$\chi_j(\psi + \pi) = \chi_j^*(\psi), \qquad j \in \{\mathrm{ref}, \mathrm{fld}\}.$$

Because the primed basis is aligned with the reverse propagation direction, the positive-propagation eigenvector forms in equations (A.31) and (A.32) can be used directly in this basis, with χ_j replaced by χ_j^*. The reverse-propagating quasi-Love and quasi-Rayleigh eigenvectors expressed in the primed basis are therefore

$$\boldsymbol{p}'^{-}_{qL,j}(0) = \begin{pmatrix} \chi_j^* V_j \\ W_j \\ \mathrm{i}\chi_j^* U_j \end{pmatrix} + \mathcal{O}(\epsilon^2), \qquad \boldsymbol{p}'^{-}_{qR,j}(0) = \begin{pmatrix} V_j \\ -\chi_j W_j \\ \mathrm{i}U_j \end{pmatrix} + \mathcal{O}(\epsilon^2).$$

These are the eigenvectors in the temporary propagation-oriented coordinates. Before constructing the negative-lag Green and cross-correlation tensors, we transform them back to the fixed observational

coordinates using $\boldsymbol{S}$:

$$\boldsymbol{p}^{-}_{qL,j}(0) = \boldsymbol{S}\,\boldsymbol{p}'^{-}_{qL,j}(0) = \begin{pmatrix} -\chi_j^* V_j \\ -W_j \\ \mathrm{i}\chi_j^* U_j \end{pmatrix} + \mathcal{O}(\epsilon^2), \qquad \boldsymbol{p}^{-}_{qR,j}(0) = \boldsymbol{S}\,\boldsymbol{p}'^{-}_{qR,j}(0) = \begin{pmatrix} -V_j \\ \chi_j W_j \\ \mathrm{i}U_j \end{pmatrix} + \mathcal{O}(\epsilon^2).$$

The complete sequence is therefore

$$(R,T,Z) \xrightarrow{\text{fld}\to\text{ref}} (R',T',Z') \xrightarrow{\chi\to\chi^*} \boldsymbol{p}'^{-}_{\nu} \xrightarrow{\boldsymbol{S}} \boldsymbol{p}^{-}_{\nu} \quad \text{in fixed } (R,T,Z).$$

Thus the primed basis is purely auxiliary. From this point onward, all negative-lag eigenvectors, Green-tensor elements, and cross-correlation components are expressed in the fixed observational R, T, Z coordinate system. The reverse-propagating eigenvectors above already contain the horizontal-coordinate parity introduced by propagation reversal, so no additional sign transformation is applied to the negative-lag cross-correlation components.

A8.1 Cross-correlation–Green-tensor correspondence

At negative lag the field station is the effective source, so the second fixed-station component index identifies the force direction and the first identifies the observed displacement at the reference station. The negative-lag counterpart of equation (A.34) is

$$\boldsymbol{C}^{-}(\omega) = \begin{pmatrix} RR^- & TR^- & ZR^- \\ RT^- & TT^- & ZT^- \\ RZ^- & TZ^- & ZZ^- \end{pmatrix} \simeq \Lambda \begin{pmatrix} F_{R,\text{fld}}G_{RR} & F_{R,\text{fld}}G_{TR} & F_{R,\text{fld}}G_{ZR} \\ F_{T,\text{fld}}G_{RT} & F_{T,\text{fld}}G_{TT} & F_{T,\text{fld}}G_{ZT} \\ F_{Z,\text{fld}}G_{RZ} & F_{Z,\text{fld}}G_{TZ} & F_{Z,\text{fld}}G_{ZZ} \end{pmatrix} = \Lambda\,\boldsymbol{F}_{\text{fld}}\boldsymbol{G}(\boldsymbol{x}_{\text{ref}}, \boldsymbol{x}_{\text{fld}}; \omega)^T, \tag{A.76}$$

where $\boldsymbol{F}_{\text{fld}} = \text{diag}(F_{R,\text{fld}}, F_{T,\text{fld}}, F_{Z,\text{fld}})$. The Green tensor is evaluated for propagation from the field station to the reference station. The modal normalization integrals $I_{1\nu}$ and positive propagation-amplitude factors D_ν are unchanged by reversal under the reciprocal common-path assumptions adopted here. Under the same assumptions, $\Phi^+_\nu = \Phi^-_\nu$; the superscripts are retained to identify the correlation lag and propagation direction. The reverse-propagation dependence is carried explicitly by the endpoint ordering and the reverse-propagating eigenvectors above. Equivalently,

$$C^-_{XY} \simeq \Lambda F_{Y,\text{fld}} \left[\frac{(p^-_{qL,\text{ref}})_X (p^-_{qL,\text{fld}})^*_Y}{I_{1qL} D_{qL}} \exp(\mathrm{i}\Phi^-_{qL}) + \frac{(p^-_{qR,\text{ref}})_X (p^-_{qR,\text{fld}})^*_Y}{I_{1qR} D_{qR}} \exp(\mathrm{i}\Phi^-_{qR}) \right]. \tag{A.77}$$

Relative to equation (A.36), the endpoint product is reversed and the effective-source factor is determined by the second fixed-station component index Y.

A8.2 Carrier components, source-group normalization, and TZ^- and ZT^-

The carrier components are

$$TT^- = \Lambda F_{T,\mathrm{fld}} \frac{W_{\mathrm{ref}} W_{\mathrm{fld}}}{D_{qL}} \exp(\mathrm{i}\Phi^-_{qL}) + \mathcal{O}(\epsilon^2), \tag{A.78}$$

$$ZZ^- = \Lambda F_{Z,\mathrm{fld}} \frac{U_{\mathrm{ref}} U_{\mathrm{fld}}}{D_{qR}} \exp(\mathrm{i}\Phi^-_{qR}) + \mathcal{O}(\epsilon^2), \tag{A.79}$$

$$RR^- = \Lambda F_{R,\mathrm{fld}} \frac{V_{\mathrm{ref}} V_{\mathrm{fld}}}{D_{qR}} \exp(\mathrm{i}\Phi^-_{qR}) + \mathcal{O}(\epsilon^2). \tag{A.80}$$

At negative lag the source groups are determined by the second fixed-station component index: $F_{R,\mathrm{fld}}$: $\{RR^-, TR^-, ZR^-\}$, $F_{T,\mathrm{fld}} : \{RT^-, TT^-, ZT^-\}$, and $F_{Z,\mathrm{fld}} : \{RZ^-, TZ^-, ZZ^-\}$. The normalization factors are

$$N_{R,\mathrm{fld}} = \Lambda F_{R,\mathrm{fld}} \frac{V_{\mathrm{ref}} V_{\mathrm{fld}}}{D_{qR}}, \qquad N_{T,\mathrm{fld}} = \Lambda F_{T,\mathrm{fld}} \frac{W_{\mathrm{ref}} W_{\mathrm{fld}}}{D_{qL}}, \qquad N_{Z,\mathrm{fld}} = \Lambda F_{Z,\mathrm{fld}} \frac{U_{\mathrm{ref}} U_{\mathrm{fld}}}{D_{qR}}. \tag{A.81}$$

We denote the resulting source-group-normalized negative-lag tensor by $\widetilde{\boldsymbol{C}}^-$. As at positive lag, the tilde is applied only to the tensor variable; its evaluated entries are written without tildes as RR^-, TT^-, ... The entry labeled XY^- in $\widetilde{\boldsymbol{C}}^-$ is obtained by dividing the corresponding unnormalized component C^-_{XY} by $N_{Y,\mathrm{fld}}$, where the second fixed-station component index Y identifies the source group.

After source-group normalization, the negative-lag carrier components are

$$TT^- = \exp(\mathrm{i}\Phi^-_{qL}) + \mathcal{O}(\epsilon^2). \tag{A.82}$$

Similarly,

$$ZZ^- = \exp(\mathrm{i}\Phi^-_{qR}) + \mathcal{O}(\epsilon^2), \tag{A.83}$$

$$RR^- = \exp(\mathrm{i}\Phi^-_{qR}) + \mathcal{O}(\epsilon^2) = ZZ^- + \mathcal{O}(\epsilon^2). \tag{A.84}$$

To verify explicitly the signs of the polarization-sensitive components in the fixed observational coordinates, equation (A.77) gives

$$\begin{aligned} TZ^- &= \Lambda F_{Z,\mathrm{fld}} \left[\frac{(p^-_{qL,\mathrm{ref}})_T (p^-_{qL,\mathrm{fld}})^*_Z}{D_{qL}} \exp(\mathrm{i}\Phi^-_{qL}) + \frac{(p^-_{qR,\mathrm{ref}})_T (p^-_{qR,\mathrm{fld}})^*_Z}{D_{qR}} \exp(\mathrm{i}\Phi^-_{qR}) \right] \\ &= \mathrm{i}\Lambda F_{Z,\mathrm{fld}} W_{\mathrm{ref}} U_{\mathrm{fld}} \left[\frac{\chi_{\mathrm{fld}}}{D_{qL}} \exp(\mathrm{i}\Phi^-_{qL}) - \frac{\chi_{\mathrm{ref}}}{D_{qR}} \exp(\mathrm{i}\Phi^-_{qR}) \right] + \mathcal{O}(\epsilon^2). \end{aligned} \tag{A.85}$$

The corresponding result for ZT^- is

$$ZT^- = \mathrm{i}\Lambda F_{T,\mathrm{fld}} U_{\mathrm{ref}} W_{\mathrm{fld}} \left[-\frac{\chi^*_{\mathrm{ref}}}{D_{qL}} \exp(\mathrm{i}\Phi^-_{qL}) + \frac{\chi^*_{\mathrm{fld}}}{D_{qR}} \exp(\mathrm{i}\Phi^-_{qR}) \right] + \mathcal{O}(\epsilon^2). \tag{A.86}$$

Using the same first-order propagation-factor argument as for positive lag gives the normalized equa-

tions

$$TZ^{-} = \mathrm{i}\frac{W_{\mathrm{ref}}}{U_{\mathrm{ref}}}\left(\chi_{\mathrm{fld}}TT^{-} - \chi_{\mathrm{ref}}ZZ^{-}\right) + \mathcal{O}(\epsilon^{2}), \tag{A.87}$$

$$ZT^{-} = \mathrm{i}\frac{U_{\mathrm{ref}}}{W_{\mathrm{ref}}}\left(-\chi^{*}_{\mathrm{ref}}TT^{-} + \chi^{*}_{\mathrm{fld}}ZZ^{-}\right) + \mathcal{O}(\epsilon^{2}). \tag{A.88}$$

The waveform combinations in brackets have the same sign structure as their positive-lag counterparts in equations (A.57) and (A.58). Only the effective-receiver eigenfunction ratios change: the field station is the effective receiver at positive lag, whereas the reference station is the effective receiver at negative lag.

The remaining normalized negative-lag components satisfy, to first order, $RR^{-} = ZZ^{-}$, $TR^{-} = -\mathrm{i}(U_{\mathrm{ref}}/V_{\mathrm{ref}})TZ^{-}$, $RT^{-} = \mathrm{i}(V_{\mathrm{ref}}/U_{\mathrm{ref}})ZT^{-}$, $ZR^{-} = -\mathrm{i}(U_{\mathrm{ref}}/V_{\mathrm{ref}})ZZ^{-}$, and $RZ^{-} = \mathrm{i}(V_{\mathrm{ref}}/U_{\mathrm{ref}})ZZ^{-}$. Collecting these relations, the complete first-order source-group-normalized negative-lag cross-correlation tensor in the fixed observational coordinates is

$$\widetilde{\boldsymbol{C}}^{-} = \begin{pmatrix} ZZ^{-} & -\mathrm{i}\dfrac{U_{\mathrm{ref}}}{V_{\mathrm{ref}}}TZ^{-} & -\mathrm{i}\dfrac{U_{\mathrm{ref}}}{V_{\mathrm{ref}}}ZZ^{-} \\ \mathrm{i}\dfrac{V_{\mathrm{ref}}}{U_{\mathrm{ref}}}ZT^{-} & TT^{-} & ZT^{-} \\ \mathrm{i}\dfrac{V_{\mathrm{ref}}}{U_{\mathrm{ref}}}ZZ^{-} & TZ^{-} & ZZ^{-} \end{pmatrix} + \mathcal{O}(\epsilon^{2}). \tag{A.89}$$

Equation (A.89) gives $\widetilde{\boldsymbol{C}}^{-}$, the negative-lag counterpart of $\widetilde{\boldsymbol{C}}^{+}$ in equation (A.63). The ordering of the entries is the same as in equation (A.76), and the eigenfunction ratios are evaluated at the effective receiver, the reference station.

A8.3 Relation of the mixing coefficients for the two propagation directions

Reversal of propagation changes the azimuth from ψ to $\psi + \pi$. Equations (A.27)–(A.30) imply

$$A(\psi+\pi) = A(\psi), \qquad B(\psi+\pi) = B(\psi), \qquad E(\psi+\pi) = E(\psi), \qquad X(\psi+\pi) = -X(\psi). \tag{A.90}$$

Consequently, for $j \in \{\mathrm{ref}, \mathrm{fld}\}$,

$$\chi_{j}(\psi+\pi) = \chi^{*}_{j}(\psi). \tag{A.91}$$

With $\widetilde{\Gamma}_{j} = |\chi_{j}| \geq 0$,

$$\chi_{j} = \widetilde{\Gamma}_{j}\exp(\mathrm{i}\phi_{j}), \qquad \chi^{*}_{j} = \widetilde{\Gamma}_{j}\exp(-\mathrm{i}\phi_{j}). \tag{A.92}$$

The fixed endpoint mixing coefficient therefore carries no lag superscript; reverse propagation appears through complex conjugation in the auxiliary propagation-oriented basis and is already incorporated into the fixed-basis eigenvectors used above.

A8.4 X-dominant negative-lag equations

In the X-dominant regime, $\chi_j = \mathrm{i}\Gamma_j + \mathcal{O}(\epsilon^2)$. Equations (A.87) and (A.88) reduce to

$$\boxed{\begin{aligned} TZ^- &= \frac{W_{\mathrm{ref}}}{U_{\mathrm{ref}}}\left(-\Gamma_{\mathrm{fld}} TT^- + \Gamma_{\mathrm{ref}} ZZ^-\right) + \mathcal{O}(\epsilon^2), \qquad \text{(A.93)} \\ ZT^- &= \frac{U_{\mathrm{ref}}}{W_{\mathrm{ref}}}\left(-\Gamma_{\mathrm{ref}} TT^- + \Gamma_{\mathrm{fld}} ZZ^-\right) + \mathcal{O}(\epsilon^2). \qquad \text{(A.94)} \end{aligned}}$$

These equations have the same waveform-combination sign structure as their positive-lag counterparts in equations (A.65) and (A.66), but the eigenfunction ratios are evaluated at the negative-lag effective receiver, the reference station.

A8.5 E-dominant negative-lag equations

In the E-dominant regime, $\chi_j = \Gamma_j + \mathcal{O}(\epsilon^2)$ is real. The negative-lag equations become

$$\boxed{\begin{aligned} TZ^- &= \mathrm{i}\frac{W_{\mathrm{ref}}}{U_{\mathrm{ref}}}\left(\Gamma_{\mathrm{fld}} TT^- - \Gamma_{\mathrm{ref}} ZZ^-\right) + \mathcal{O}(\epsilon^2), \qquad \text{(A.95)} \\ ZT^- &= \mathrm{i}\frac{U_{\mathrm{ref}}}{W_{\mathrm{ref}}}\left(-\Gamma_{\mathrm{ref}} TT^- + \Gamma_{\mathrm{fld}} ZZ^-\right) + \mathcal{O}(\epsilon^2). \qquad \text{(A.96)} \end{aligned}}$$

As at positive lag, the E-dominant polarization-sensitive components are in quadrature with the corresponding modal reference combinations.

Supplementary Materials: Ambient Noise Surface-Wave Polarization in Anisotropic Media: Theory, Measurement, and Interpretation

S.1 BEYOND THE WAVELENGTH CRITERION FOR ADIABATIC SURFACE-WAVE PROPAGATION

The main text uses the operational condition

$$\frac{\ell_{\mathrm{structure}}}{\lambda_{\mathrm{wave}}} \gg 1 \tag{S1}$$

as a simple indicator of adiabatic surface-wave propagation. This criterion expresses the intuitive requirement that the medium vary little over a wavelength, but it does not contain all of the quantities that control conversion between quasi-Love and quasi-Rayleigh waves. In particular, the magnitude of the resulting polarization change and the separation between the two local surface-wave branches are also important. Here we develop a reduced two-mode propagation model to make these dependencies explicit and to clarify the physical content of equation (S1).

The purpose of the derivation is not to provide a complete theory of surface-wave scattering at arbitrary discontinuities and the analysis presented here for anisotropic media is similar to those of Kennett (1984), Maupin (1988), and Tromp (1994a), although their work focuses primarily on isotropic media or does not explicitly address Rayleigh-Love coupling. Rather, we retain the same fundamental quasi-Love–quasi-Rayleigh subspace used in the main text and ask how spatial variation of the local polarization eigenvectors generates conversion between these two forward-propagating wave types. This reduced model provides a more complete adiabaticity criterion than (S1) while remaining directly connected to the polarization parameter used in the main text.

Two-mode propagation in the local eigenbasis

At fixed angular frequency ω, let x measure distance along the propagation path and let z denote depth. The common time dependence is suppressed. We retain only the local fundamental quasi-Love and quasi-Rayleigh branches and denote their normalized displacement polarization eigenfunctions by $\boldsymbol{p}_{qL}(z;x)$ and $\boldsymbol{p}_{qR}(z;x)$, with local fixed-frequency wavenumbers $k_{qL}(x)$ and $k_{qR}(x)$. Consistent with the near-common-wavenumber approximation used in the main text, the polarization eigenfunctions are evaluated at a common local reference wavenumber, while the distinct qL and qR wavenumbers are retained in their propagation phases. The density-weighted modal inner product is the same as that used in the main paper,

$$\langle \boldsymbol{p}, \boldsymbol{q} \rangle \equiv \int_0^\infty \rho(z)\, \boldsymbol{p}^\dagger(z) \boldsymbol{q}(z)\, \mathrm{d}z, \tag{S2}$$

where † denotes the Hermitian (complex-conjugate) transpose. For the derivation below, the density weighting is taken to be independent of x, as in the numerical models used in the main text. The two local modes are normalized so that

$$\langle \boldsymbol{p}_{qL}, \boldsymbol{p}_{qL} \rangle = \langle \boldsymbol{p}_{qR}, \boldsymbol{p}_{qR} \rangle = 1, \qquad \langle \boldsymbol{p}_{qL}, \boldsymbol{p}_{qR} \rangle = 0. \tag{S3}$$

Within a reduced forward-propagating two-mode description, the physical displacement is expanded at each position in this local basis,

$$\boldsymbol{u}(x, z) = b_L(x)\boldsymbol{p}_{qL}(z; x) + b_R(x)\boldsymbol{p}_{qR}(z; x). \tag{S4}$$

The coefficients b_L and b_R include the rapidly varying propagation phase. Scalar amplitude factors associated with uncoupled propagation, such as geometrical spreading or a slowly varying flux normalization, are absorbed into the definitions of the modal coefficients; they do not by themselves produce conversion between the two retained branches. Over an infinitesimal distance $\mathrm{d}x$, if the local eigenbasis were held fixed, the two forward modes would therefore acquire their local propagation phases,

$$\begin{aligned}\boldsymbol{u}(x + \mathrm{d}x, z) = {} & b_L(x)e^{-\mathrm{i}k_{qL}(x)\mathrm{d}x}\boldsymbol{p}_{qL}(z; x) \\ & + b_R(x)e^{-\mathrm{i}k_{qR}(x)\mathrm{d}x}\boldsymbol{p}_{qR}(z; x) + \mathcal{O}(\mathrm{d}x^2).\end{aligned} \tag{S5}$$

Equation (S5) is the reduced local-mode propagation assumption used here. It retains forward qL and qR propagation and the change of their local basis, but not reflection or coupling to other surface-wave branches.

The same displacement at $x + \mathrm{d}x$ must also be expressible in the local basis there,

$$\boldsymbol{u}(x + \mathrm{d}x, z) = b_L(x + \mathrm{d}x)\boldsymbol{p}_{qL}(z; x + \mathrm{d}x) + b_R(x + \mathrm{d}x)\boldsymbol{p}_{qR}(z; x + \mathrm{d}x). \tag{S6}$$

Because the basis is orthonormal, the coefficient of either branch $m \in \{L, R\}$ is obtained by projection,

$$b_m(x + \mathrm{d}x) = \langle \boldsymbol{p}_{qm}(x + \mathrm{d}x), \boldsymbol{u}(x + \mathrm{d}x) \rangle . \tag{S7}$$

Expanding the local eigenfunction and propagation phase to first order,

$$\boldsymbol{p}_{qm}(x + \mathrm{d}x) = \boldsymbol{p}_{qm}(x) + \partial_x \boldsymbol{p}_{qm}(x)\, \mathrm{d}x + \mathcal{O}(\mathrm{d}x^2), \tag{S8}$$

$$e^{-\mathrm{i}k_{qn}\mathrm{d}x} = 1 - \mathrm{i}k_{qn}\mathrm{d}x + \mathcal{O}(\mathrm{d}x^2), \tag{S9}$$

and substituting equations (S5), (S8), and (S9) into (S7) gives

$$b_m(x+\mathrm{d}x) = b_m(x) - \mathrm{i}k_{qm}(x)b_m(x)\mathrm{d}x + \mathrm{d}x \sum_{n=L,R} b_n(x)\left\langle \partial_x \boldsymbol{p}_{qm}, \boldsymbol{p}_{qn}\right\rangle + \mathcal{O}(\mathrm{d}x^2). \tag{S10}$$

The derivative of the orthonormality relation is

$$0 = \partial_x \left\langle \boldsymbol{p}_{qm}, \boldsymbol{p}_{qn}\right\rangle = \left\langle \partial_x \boldsymbol{p}_{qm}, \boldsymbol{p}_{qn}\right\rangle + \left\langle \boldsymbol{p}_{qm}, \partial_x \boldsymbol{p}_{qn}\right\rangle, \tag{S11}$$

so equation (S10), after subtracting $b_m(x)$, dividing by $\mathrm{d}x$, and taking the limit $\mathrm{d}x \to 0$, becomes

$$\frac{\mathrm{d}b_m}{\mathrm{d}x} = -\mathrm{i}k_{qm}b_m - \sum_{n=L,R} b_n \left\langle \boldsymbol{p}_{qm}, \partial_x \boldsymbol{p}_{qn}\right\rangle. \tag{S12}$$

This equation separates the ordinary phase accumulation of each local branch from coupling caused by spatial change of the local eigenbasis.

We now remove the accumulated propagation phases by defining

$$\theta_L(x) = \int_{x_0}^{x} k_{qL}(s)\,\mathrm{d}s, \qquad \theta_R(x) = \int_{x_0}^{x} k_{qR}(s)\,\mathrm{d}s, \tag{S13}$$

and

$$b_L(x) = a_L(x)e^{-\mathrm{i}\theta_L(x)}, \qquad b_R(x) = a_R(x)e^{-\mathrm{i}\theta_R(x)}. \tag{S14}$$

Substitution into equation (S12) gives, for $m = L$ and $m = R$ respectively,

$$\frac{\mathrm{d}a_L}{\mathrm{d}x} = -a_L \left\langle \boldsymbol{p}_{qL}, \partial_x \boldsymbol{p}_{qL}\right\rangle - a_R \left\langle \boldsymbol{p}_{qL}, \partial_x \boldsymbol{p}_{qR}\right\rangle e^{-\mathrm{i}(\theta_R-\theta_L)}, \tag{S15}$$

$$\frac{\mathrm{d}a_R}{\mathrm{d}x} = -a_R \left\langle \boldsymbol{p}_{qR}, \partial_x \boldsymbol{p}_{qR}\right\rangle - a_L \left\langle \boldsymbol{p}_{qR}, \partial_x \boldsymbol{p}_{qL}\right\rangle e^{\mathrm{i}(\theta_R-\theta_L)}. \tag{S16}$$

The normalization in equation (S3) implies that $\left\langle \boldsymbol{p}_n, \partial_x \boldsymbol{p}_n\right\rangle$ is purely imaginary. The arbitrary local phase of each eigenvector can therefore be chosen so that

$$\left\langle \boldsymbol{p}_{qL}, \partial_x \boldsymbol{p}_{qL}\right\rangle = \left\langle \boldsymbol{p}_{qR}, \partial_x \boldsymbol{p}_{qR}\right\rangle = 0, \tag{S17}$$

which is the parallel-transport phase convention. With

$$\Delta k(x) \equiv k_{qR}(x) - k_{qL}(x), \qquad \Phi(x) \equiv \theta_R(x) - \theta_L(x) = \int_{x_0}^{x} \Delta k(s)\,\mathrm{d}s, \tag{S18}$$

and

$$\mathcal{A}_{RL}(x) \equiv \left\langle \boldsymbol{p}_{qR}, \partial_x \boldsymbol{p}_{qL}\right\rangle, \tag{S19}$$

equation (S16) reduces to

$$\frac{\mathrm{d}a_R}{\mathrm{d}x} = -\mathcal{A}_{RL}(x)a_L(x)e^{\mathrm{i}\Phi(x)}. \tag{S20}$$

Thus spatial change of the local polarization eigenvectors is the direct source of nonadiabatic conversion in the reduced two-mode system. The oscillatory factor $e^{\mathrm{i}\Phi}$ accounts for the differential phase accumulated between the quasi-Rayleigh and quasi-Love branches.

For an incident quasi-Love wave, take $a_L(x_0) = 1$ and $a_R(x_0) = 0$. When the conversion is weak, a_R is first order in $\mathcal{A}_{RL}$ and the change in a_L is second order. We may therefore set $a_L = 1$ in (S20) to obtain the first-order converted quasi-Rayleigh amplitude

$$a_R(X) \simeq -\int_{x_0}^{X} \mathcal{A}_{RL}(x) \exp\left[\mathrm{i}\int_{x_0}^{x} \Delta k(s)\,\mathrm{d}s\right] \mathrm{d}x. \tag{S21}$$

Equation (S21) is the basic result needed below. It shows that conversion depends both on the spatial variation of the local eigenvectors and on the differential qR–qL phase accumulated across the region of variation.

A complete derivation from the elastodynamic equations would formulate the spatial transport problem with an appropriately flux-normalized displacement–traction state and would retain reflected waves and additional surface-wave branches where required. The infinitesimal construction above is instead a reduced forward two-mode derivation designed to isolate the geometrical coupling produced by rotation of the local qL–qR eigenbasis. It is sufficient for identifying the amplitude and length scales that control the onset of nonadiabatic conversion in the setting considered here.

Connection with the polarization mixing coefficient

The two-mode polarization theory in the main text writes the local eigenvectors to first order as

$$\boldsymbol{p}_{qL} = \boldsymbol{p}_L^0 + \chi \boldsymbol{p}_R^0 + \mathcal{O}(\epsilon^2), \tag{S22}$$

$$\boldsymbol{p}_{qR} = \boldsymbol{p}_R^0 - \chi^* \boldsymbol{p}_L^0 + \mathcal{O}(\epsilon^2), \tag{S23}$$

where $\boldsymbol{p}_L^0$ and $\boldsymbol{p}_R^0$ are normalized fundamental Love and Rayleigh eigenfunctions of the local isotropic or VTI reference model and

$$\chi = \frac{E + \mathrm{i}X}{A - B} + \mathcal{O}(\epsilon^2). \tag{S24}$$

Here ϵ denotes the order of weak polarization mixing. The reference modes satisfy

$$\langle \boldsymbol{p}_L^0, \boldsymbol{p}_L^0 \rangle = \langle \boldsymbol{p}_R^0, \boldsymbol{p}_R^0 \rangle = 1, \qquad \langle \boldsymbol{p}_L^0, \boldsymbol{p}_R^0 \rangle = 0. \tag{S25}$$

We now evaluate the derivative coupling in (S19). Differentiating equation (S22) gives

$$\partial_x \boldsymbol{p}_{qL} = \partial_x \boldsymbol{p}_L^0 + \frac{\mathrm{d}\chi}{\mathrm{d}x} \boldsymbol{p}_R^0 + \chi\, \partial_x \boldsymbol{p}_R^0 + \mathcal{O}(\epsilon^2). \tag{S26}$$

The bra corresponding to equation (S23) is

$$\boldsymbol{p}_{qR}^\dagger = (\boldsymbol{p}_R^0)^\dagger - \chi (\boldsymbol{p}_L^0)^\dagger + \mathcal{O}(\epsilon^2). \tag{S27}$$

Using equations (S25)–(S27), and retaining terms through first order, gives

$$\mathcal{A}_{RL} = \left\langle \boldsymbol{p}_R^0, \partial_x \boldsymbol{p}_L^0 \right\rangle + \frac{\mathrm{d}\chi}{\mathrm{d}x} + \chi \left(\left\langle \boldsymbol{p}_R^0, \partial_x \boldsymbol{p}_R^0 \right\rangle - \left\langle \boldsymbol{p}_L^0, \partial_x \boldsymbol{p}_L^0 \right\rangle \right) + \mathcal{O}(\epsilon^2). \tag{S28}$$

This expression separates conversion caused by spatial variation of the reference eigenfunctions from conversion caused by spatial variation of the anisotropic mixing coefficient.

The numerical experiments emphasized in the main text are especially simple: the isotropic reference model is fixed horizontally and only the anisotropic perturbation varies along the path. For that case,

$$\partial_x \boldsymbol{p}_L^0 = \partial_x \boldsymbol{p}_R^0 = 0, \tag{S29}$$

and equation (S28) becomes

$$\boxed{\mathcal{A}_{RL}(x) = \frac{\mathrm{d}\chi}{\mathrm{d}x} + \mathcal{O}(\epsilon^2).} \tag{S30}$$

The first-order conversion amplitude is therefore

$$\boxed{a_R(X) \simeq -\int_{x_0}^{X} \frac{\mathrm{d}\chi}{\mathrm{d}x} \exp\left[\mathrm{i} \int_{x_0}^{x} \Delta k(s)\, \mathrm{d}s \right] \mathrm{d}x.} \tag{S31}$$

In the X-dominant regime used for most of the measurements and numerical benchmarks in the main text,

$$\chi = \mathrm{i}\Gamma, \tag{S32}$$

where Γ is the signed polarization parameter. Equation (S31) then becomes

$$a_R(X) \simeq -\mathrm{i} \int_{x_0}^{X} \frac{\mathrm{d}\Gamma}{\mathrm{d}x} \exp\left[\mathrm{i} \int_{x_0}^{x} \Delta k(s)\, \mathrm{d}s \right] \mathrm{d}x. \tag{S33}$$

Thus, for a fixed reference model, spatial variation of the polarization parameter itself drives qL–qR conversion to first order. In the E-dominant regime, $\chi = \Gamma$, so in either the X-dominant or E-dominant limit the phase relating χ to Γ is spatially constant and $|\mathrm{d}\chi/\mathrm{d}x| = |\mathrm{d}\Gamma/\mathrm{d}x|$. The Γ-based adiabaticity criteria derived below therefore apply to both limiting regimes.

A local adiabaticity criterion

Equation (S31) provides a direct route to an adiabaticity criterion. To expose the role of the differential phase, use

$$\frac{\mathrm{d}}{\mathrm{d}x} e^{\mathrm{i}\Phi(x)} = \mathrm{i}\Delta k(x) e^{\mathrm{i}\Phi(x)} \tag{S34}$$

to integrate equation (S21) by parts:

$$a_R(X) \simeq -\left[\frac{\mathcal{A}_{RL}(x)}{\mathrm{i}\Delta k(x)} e^{\mathrm{i}\Phi(x)}\right]_{x_0}^{X} + \int_{x_0}^{X} e^{\mathrm{i}\Phi(x)} \frac{\mathrm{d}}{\mathrm{d}x}\left[\frac{\mathcal{A}_{RL}(x)}{\mathrm{i}\Delta k(x)}\right] \mathrm{d}x. \tag{S35}$$

For a localized smooth transition, $\mathcal{A}_{RL}$ vanishes outside the transition and the boundary term is absent. Equation (S35) shows that conversion is small when the derivative coupling is small compared with the qR–qL wavenumber separation and when that ratio itself does not vary rapidly. The leading local adiabaticity requirement is therefore

$$\boxed{\varepsilon_{\mathrm{ad}}(x) \equiv \frac{|\mathcal{A}_{RL}(x)|}{|\Delta k(x)|} \ll 1.} \tag{S36}$$

For the fixed-reference two-mode problem in equation (S30), this becomes

$$\boxed{\varepsilon_{\mathrm{ad}}(x) \simeq \frac{|\mathrm{d}\chi/\mathrm{d}x|}{|\Delta k|} \ll 1.} \tag{S37}$$

In either the X-dominant or E-dominant limit,

$$\boxed{\varepsilon_{\mathrm{ad}}(x) \simeq \frac{|\mathrm{d}\Gamma/\mathrm{d}x|}{|\Delta k|} \ll 1.} \tag{S38}$$

Suppose that χ changes by a characteristic amount $\Delta\chi$ across a transition of width $\ell_{\mathrm{structure}}$. Then

$$\left|\frac{\mathrm{d}\chi}{\mathrm{d}x}\right| \sim \frac{|\Delta\chi|}{\ell_{\mathrm{structure}}}, \tag{S39}$$

and equation (S37) gives

$$\boxed{\varepsilon_{\mathrm{ad}} \sim \frac{|\Delta\chi|}{|\Delta k|\,\ell_{\mathrm{structure}}} \ll 1.} \tag{S40}$$

In either limiting regime, $|\Delta\chi| = |\Delta\Gamma|$, so

$$\boxed{\varepsilon_{\mathrm{ad}} \sim \frac{|\Delta\Gamma|}{|\Delta k|\,\ell_{\mathrm{structure}}} \ll 1.} \tag{S41}$$

Equation (S41) makes explicit that adiabaticity is controlled jointly by the magnitude of the polarization change, the length scale over which it occurs, and the separation of the qL and qR propagation constants.

Relation to the wavelength criterion used in the main text

To connect equation (S41) with the simpler criterion used in the main text, define a representative wavenumber and wavelength by

$$\bar{k} \equiv \frac{k_{qR} + k_{qL}}{2}, \qquad \lambda_{\mathrm{wave}} \equiv \frac{2\pi}{\bar{k}}. \tag{S42}$$

Using equation (S42), equation (S41) can be written

$$\boxed{\varepsilon_{\mathrm{ad}} \sim \frac{\bar{k}|\Delta\Gamma|}{2\pi|\Delta k|} \frac{\lambda_{\mathrm{wave}}}{\ell_{\mathrm{structure}}} \ll 1.} \tag{S43}$$

This expression shows directly what is suppressed when adiabaticity is judged only from $\ell_{\mathrm{structure}}/\lambda_{\mathrm{wave}}$. The wavelength ratio is one factor, but the prefactor $\bar{k}|\Delta\Gamma|/(2\pi|\Delta k|)$ contains both the magnitude of the polarization change and the relative separation of the qL and qR propagation constants. The operational condition $\ell_{\mathrm{structure}} \gg \lambda_{\mathrm{wave}}$ is therefore a useful heuristic when this prefactor is not large, but it is not a complete adiabaticity criterion. In particular, a small qL–qR wavenumber separation makes conversion more difficult to suppress, whereas a small $|\Delta\Gamma|$ can keep conversion weak even when the structural variation occurs on a comparatively short length scale.

The criterion in equation (S43) is obtained within a reduced forward two-mode treatment. Its simplified form in terms of $|\mathrm{d}\chi/\mathrm{d}x|$ assumes that horizontal variation of the local polarization basis is carried principally by χ, as in the numerical models used in the main text; if the isotropic or VTI reference structure also varies horizontally, the full derivative coupling in equation (S36) must be retained. The analysis also assumes weak Rayleigh–Love mixing and retains only the forward-propagating fundamental qL and qR branches. It is therefore intended to identify the quantities controlling the onset of nonadiabatic qL–qR conversion, rather than to provide a complete elastic scattering theory that includes reflected waves, overtones, and other scattered modes.

S.2 First-Order Residual Corrections to the Two-Mode Polarization Theory

This section retains projection residuals of order ϵ in the local quasi-Love and quasi-Rayleigh eigenfunctions, rather than imposing the two-mode approximation $\boldsymbol{\eta}_j^L, \boldsymbol{\eta}_j^R = \mathcal{O}(\epsilon^2)$ adopted in Appendix A of the main text. We formulate the residual calculation explicitly for positive-lag propagation from the reference station to the field station, $\mathrm{ref} \rightarrow \mathrm{fld}$, corresponding to Sections A5–A7 of the main text. To avoid overburdening the notation, the superscript $+$ is suppressed throughout this section: χ_j and $\boldsymbol{\eta}_j^{L,R}$ are evaluated for the fixed reference-to-field azimuth, and TT, ZZ, TZ, and ZT denote positive-lag source-group-normalized cross-correlations. The negative-lag two-mode transformation is derived separately in Section A8 of the main text; an extension of the residual corrections to neg-

ative lag is not required for the present residual assessment. Appendix A of the main text derives all nine source-group-normalized cross-correlation components. Here we retain only TT, ZZ, TZ, and ZT: to first order, TT and ZZ are the quasi-Love and quasi-Rayleigh carrier waveforms, while TZ and ZT contain the independent polarization information used to estimate the endpoint corrections. The remaining five components either reproduce a carrier waveform or are algebraically related to these four under the same assumptions. All quantities below are evaluated at fixed frequency and the fixed reference-to-field azimuth, and products of two first-order quantities are omitted.

A9 Branch-by-branch construction of TZ and ZT

The reference eigenvectors and the general first-order projected eigenvectors are given by equations (A.9), (A.19), and (A.20) of the main text. In the present section, $\chi_j = \mathcal{O}(\epsilon)$ and $\boldsymbol{\eta}_j^L, \boldsymbol{\eta}_j^R = \mathcal{O}(\epsilon)$ at endpoint $j \in \{\mathrm{ref}, \mathrm{fld}\}$. Of the six surface components, only the following four enter the first-order TZ and ZT equations:

$$(\boldsymbol{p}_{qL,j})_T = W_j + \eta_{jT}^L, \qquad (\boldsymbol{p}_{qL,j})_Z = \mathrm{i}\chi_j U_j + \eta_{jZ}^L, \tag{S44}$$

$$(\boldsymbol{p}_{qR,j})_Z = \mathrm{i}U_j + \eta_{jZ}^R, \qquad (\boldsymbol{p}_{qR,j})_T = -\chi_j^* W_j + \eta_{jT}^R. \tag{S45}$$

Here and below, an omitted depth argument denotes evaluation at the surface, $z = 0$.

We now follow the same branch-by-branch construction used in Appendix A of the main text. Equation (A.36) expresses each unnormalized cross-correlation component as the sum of quasi-Love and quasi-Rayleigh contributions, and equations (A.47)–(A.49) specify the source-group normalizations. Consistent with Appendix A of the main text, differences between the quasi-Love and quasi-Rayleigh propagation factors contribute only at second order to the polarization-sensitive terms and are omitted below. Write

$$TZ = TZ^{qL} + TZ^{qR} + \mathcal{O}(\epsilon^2), \qquad ZT = ZT^{qL} + ZT^{qR} + \mathcal{O}(\epsilon^2).$$

We show the branch-by-branch normalization explicitly for the quasi-Love contribution to TZ. Equation (A.43), followed by division by the reference-station transverse-source normalization $N_{T,\mathrm{ref}}$ in equation (A.47), gives

$$\begin{aligned} TZ^{qL} &= \frac{1}{N_{T,\mathrm{ref}}} \Lambda F_{T,\mathrm{ref}} \frac{(\boldsymbol{p}_{qL,\mathrm{fld}})_Z (\boldsymbol{p}_{qL,\mathrm{ref}})_T^*}{D_{qL}} \exp(\mathrm{i}\Phi_{qL}) \\ &= \frac{(\boldsymbol{p}_{qL,\mathrm{fld}})_Z (\boldsymbol{p}_{qL,\mathrm{ref}})_T^*}{W_{\mathrm{fld}} W_{\mathrm{ref}}} \exp(\mathrm{i}\Phi_{qL}), \end{aligned} \tag{S46a}$$

$$TT^{qL} = \frac{(\boldsymbol{p}_{qL,\mathrm{fld}})_T (\boldsymbol{p}_{qL,\mathrm{ref}})_T^*}{W_{\mathrm{fld}} W_{\mathrm{ref}}} \exp(\mathrm{i}\Phi_{qL}), \tag{S46b}$$

$$TZ^{qL} = \frac{(\boldsymbol{p}_{qL,\mathrm{fld}})_Z}{(\boldsymbol{p}_{qL,\mathrm{fld}})_T} TT + \mathcal{O}(\epsilon^2). \tag{S46c}$$

The third relation follows by dividing equation (S46a) by equation (S46b); the reference-station eigenfunction, modal phase, propagation factor, reference-station effective-source strength, and source-group normalization cancel. Here $TT = TT^{qL} + \mathcal{O}(\epsilon^2)$ because the quasi-Rayleigh contribution to TT is quadratic in the first-order mixing and residual amplitudes.

The other three branch contributions follow by the same procedure: apply the appropriate source-group normalization from equations (A.48)–(A.49) and divide by the corresponding carrier waveform. The results are

$$TZ^{qR} = \frac{U_{\mathrm{fld}}}{W_{\mathrm{fld}}} \left[\frac{U_{\mathrm{ref}}}{W_{\mathrm{ref}}} \frac{(\boldsymbol{p}_{qR,\mathrm{ref}})^*_T}{(\boldsymbol{p}_{qR,\mathrm{ref}})^*_Z} \right] ZZ, \tag{S47a}$$

$$ZT^{qL} = \frac{W_{\mathrm{fld}}}{U_{\mathrm{fld}}} \left[\frac{W_{\mathrm{ref}}}{U_{\mathrm{ref}}} \frac{(\boldsymbol{p}_{qL,\mathrm{ref}})^*_Z}{(\boldsymbol{p}_{qL,\mathrm{ref}})^*_T} \right] TT, \tag{S47b}$$

$$ZT^{qR} = \frac{(\boldsymbol{p}_{qR,\mathrm{fld}})_T}{(\boldsymbol{p}_{qR,\mathrm{fld}})_Z} ZZ. \tag{S47c}$$

Equations (S46c) and (S47a)–(S47c) are the individual branch contributions, not complete tensor components. In the quasi-Love contribution to TZ and the quasi-Rayleigh contribution to ZT, the reference-station-side factors cancel because the cross-component and its carrier waveform share the same source direction and modal branch. In the other two contributions, the different source-group normalizations leave the displayed reference-station eigenfunction ratios.

Substitution of equations (S44) and (S45) into the four branch factors in equations (S46c) and (S47a)–(S47c) gives, to first order,

$$\frac{(\boldsymbol{p}_{qL,j})_Z}{(\boldsymbol{p}_{qL,j})_T} = \mathrm{i}\chi_j \frac{U_j}{W_j} + \frac{\eta^L_{jZ}}{W_j} + \mathcal{O}(\epsilon^2), \tag{S48a}$$

$$\frac{U_j}{W_j} \frac{(\boldsymbol{p}_{qR,j})^*_T}{(\boldsymbol{p}_{qR,j})^*_Z} = -\mathrm{i}\chi_j + \mathrm{i}\frac{\eta^{R*}_{jT}}{W_j} + \mathcal{O}(\epsilon^2), \tag{S48b}$$

$$\frac{W_j}{U_j} \frac{(\boldsymbol{p}_{qL,j})^*_Z}{(\boldsymbol{p}_{qL,j})^*_T} = -\mathrm{i}\chi^*_j + \frac{\eta^{L*}_{jZ}}{U_j} + \mathcal{O}(\epsilon^2), \tag{S48c}$$

$$\frac{(\boldsymbol{p}_{qR,j})_T}{(\boldsymbol{p}_{qR,j})_Z} = \mathrm{i}\chi^*_j \frac{W_j}{U_j} - \mathrm{i}\frac{\eta^R_{jT}}{U_j} + \mathcal{O}(\epsilon^2). \tag{S48d}$$

The denominator corrections η^L_{jT} and η^R_{jZ} multiply first-order numerators and therefore contribute only at $\mathcal{O}(\epsilon^2)$. Equivalently, the carrier waveforms TT and ZZ already contain the first-order corrections parallel to the dominant quasi-Love and quasi-Rayleigh polarizations.

Combining equations (S46c) and (S47a)–(S47c) with equations (S48a)–(S48d) gives the general

first-order relations

$$TZ = \frac{U_{\rm fld}}{W_{\rm fld}}\left(\mathrm{i}\chi_{\rm fld} + \frac{\eta^L_{\rm fld,Z}}{U_{\rm fld}}\right)TT + \frac{U_{\rm fld}}{W_{\rm fld}}\left(-\mathrm{i}\chi_{\rm ref} + \mathrm{i}\frac{\eta^{R*}_{\rm ref,T}}{W_{\rm ref}}\right)ZZ + \mathcal{O}(\epsilon^2), \tag{S49}$$

$$ZT = \frac{W_{\rm fld}}{U_{\rm fld}}\left(-\mathrm{i}\chi^*_{\rm ref} + \frac{\eta^{L*}_{\rm ref,Z}}{U_{\rm ref}}\right)TT + \frac{W_{\rm fld}}{U_{\rm fld}}\left(\mathrm{i}\chi^*_{\rm fld} - \mathrm{i}\frac{\eta^{R}_{\rm fld,T}}{W_{\rm fld}}\right)ZZ + \mathcal{O}(\epsilon^2). \tag{S50}$$

Only η^L_Z and η^R_T enter these equations explicitly at first order. The residual components parallel to the carrier polarizations, η^L_T and η^R_Z, are absorbed into TT and ZZ and affect the component ratios only at second order.

A10 X-dominant residual corrections

In the X-dominant regime, Appendix A of the main text defines the signed real polarization parameter by $\chi_j = \mathrm{i}\Gamma_j + \mathcal{O}(\epsilon^2)$. Under the lossless phase convention used there, the relevant residual components have the phases $\eta^L_{jZ} \in \mathbb{R}$ and $\eta^R_{jT} \in \mathrm{i}\mathbb{R}$. We define their dimensionless effects on the inferred polarization parameter by

$$\Delta\Gamma^L_{jZ} \equiv \frac{\eta^L_{jZ}}{U_j}, \qquad \Delta\Gamma^R_{jT} \equiv -\mathrm{i}\frac{\eta^R_{jT}}{W_j}, \qquad \Delta\Gamma^L_{jZ}, \Delta\Gamma^R_{jT} \in \mathbb{R}. \tag{S51}$$

Equations (S49) and (S50) become

$$\boxed{TZ = \frac{U_{\rm fld}}{W_{\rm fld}}\left[\left(-\Gamma_{\rm fld} + \Delta\Gamma^L_{\rm fld,Z}\right)TT + \left(\Gamma_{\rm ref} + \Delta\Gamma^R_{\rm ref,T}\right)ZZ\right] + \mathcal{O}(\epsilon^2),} \tag{S52}$$

$$\boxed{ZT = \frac{W_{\rm fld}}{U_{\rm fld}}\left[\left(-\Gamma_{\rm ref} + \Delta\Gamma^L_{\rm ref,Z}\right)TT + \left(\Gamma_{\rm fld} + \Delta\Gamma^R_{\rm fld,T}\right)ZZ\right] + \mathcal{O}(\epsilon^2).} \tag{S53}$$

The two waveform coefficients associated with endpoint j therefore determine the effective quantities

$$\Gamma^L_{{\rm eff},j} = \Gamma_j - \Delta\Gamma^L_{jZ}, \qquad \Gamma^R_{{\rm eff},j} = \Gamma_j + \Delta\Gamma^R_{jT}. \tag{S54}$$

A11 E-dominant residual corrections

In the E-dominant regime, Appendix A of the main text gives $\chi_j = \Gamma_j + \mathcal{O}(\epsilon^2)$ with $\Gamma_j \in \mathbb{R}$. The corresponding residual phases are $\eta^L_{jZ} \in \mathrm{i}\mathbb{R}$ and $\eta^R_{jT} \in \mathbb{R}$. We define

$$\Delta\Gamma^L_{jZ} \equiv -\mathrm{i}\frac{\eta^L_{jZ}}{U_j}, \qquad \Delta\Gamma^R_{jT} \equiv -\frac{\eta^R_{jT}}{W_j}, \qquad \Delta\Gamma^L_{jZ}, \Delta\Gamma^R_{jT} \in \mathbb{R}. \tag{S55}$$

The same symbols are used in the two limiting regimes because they denote dimensionless corrections to the polarization parameter; their definitions absorb the regime-dependent residual phases. Equa-

tions (S49) and (S50) then give

$$\boxed{\begin{aligned} TZ &= \mathrm{i}\frac{U_{\mathrm{fld}}}{W_{\mathrm{fld}}}\left[\left(\Gamma_{\mathrm{fld}}+\Delta\Gamma^{L}_{\mathrm{fld},Z}\right)TT-\left(\Gamma_{\mathrm{ref}}+\Delta\Gamma^{R}_{\mathrm{ref},T}\right)ZZ\right]+\mathcal{O}(\epsilon^2), \qquad \text{(S56)}\\ ZT &= \mathrm{i}\frac{W_{\mathrm{fld}}}{U_{\mathrm{fld}}}\left[-\left(\Gamma_{\mathrm{ref}}+\Delta\Gamma^{L}_{\mathrm{ref},Z}\right)TT+\left(\Gamma_{\mathrm{fld}}+\Delta\Gamma^{R}_{\mathrm{fld},T}\right)ZZ\right]+\mathcal{O}(\epsilon^2). \qquad \text{(S57)}\end{aligned}}$$

The corresponding effective quantities are

$$\Gamma^{L}_{\mathrm{eff},j}=\Gamma_j+\Delta\Gamma^{L}_{jZ}, \qquad \Gamma^{R}_{\mathrm{eff},j}=\Gamma_j+\Delta\Gamma^{R}_{jT}. \qquad \text{(S58)}$$

A12 Reduction to the two-mode theory

When $\boldsymbol{\eta}^{L}_{j},\boldsymbol{\eta}^{R}_{j}=\mathcal{O}(\epsilon^2)$, the corrections $\Delta\Gamma^{L}_{jZ}$ and $\Delta\Gamma^{R}_{jT}$ are also second order. Equations (S52) and (S53) then reduce to the positive-lag X-dominant equations (A.65) and (A.66), and equations (S56) and (S57) reduce to the positive-lag E-dominant equations (A.71) and (A.72) of Appendix A in the main text.

S.3 The 21 Anisotropy Parameters

Montagner & Nataf (1986) introduced linear recombinations of the elastic tensor components to define certain anisotropic parameters needed to analyze surface-wave azimuthal anisotropy. Chen & Tromp (2007) introduced others that also are needed for body waves. We follow Chen & Tromp (2007) by

including the negative sign in the definition of G_s, B_s, H_s and E_s as follows:

$$\mathcal{A} = \frac{1}{8}(3C_{11} + 3C_{22} + 2C_{12} + 4C_{66}) \tag{S59}$$

$$\mathcal{C} = C_{33} \tag{S60}$$

$$\mathcal{N} = \frac{1}{8}(C_{11} + C_{22} - 2C_{12} + 4C_{66}) \tag{S61}$$

$$\mathcal{L} = \frac{1}{2}(C_{44} + C_{55}) \tag{S62}$$

$$\mathcal{F} = \frac{1}{2}(C_{13} + C_{23}) \tag{S63}$$

$$J_c = \frac{1}{8}(3C_{15} + C_{25} + 2C_{46}) \tag{S64}$$

$$J_s = \frac{1}{8}(C_{14} + 3C_{24} + 2C_{56}) \tag{S65}$$

$$K_c = \frac{1}{8}(3C_{15} + C_{25} + 2C_{46} - 4C_{35}) \tag{S66}$$

$$K_s = \frac{1}{8}(C_{14} + 3C_{24} + 2C_{56} - 4C_{34}) \tag{S67}$$

$$M_c = \frac{1}{4}(C_{15} - C_{25} + 2C_{46}) \tag{S68}$$

$$M_s = \frac{1}{4}(C_{14} - C_{24} - 2C_{56}) \tag{S69}$$

$$G_c = \frac{1}{2}(C_{55} - C_{44}) \tag{S70}$$

$$G_s = -C_{45} \tag{S71}$$

$$B_c = \frac{1}{2}(C_{11} - C_{22}) \tag{S72}$$

$$B_s = -(C_{16} + C_{26}) \tag{S73}$$

$$H_c = \frac{1}{2}(C_{13} - C_{23}) \tag{S74}$$

$$H_s = -C_{36} \tag{S75}$$

$$D_c = \frac{1}{4}(C_{15} - C_{25} - 2C_{46}) \tag{S76}$$

$$D_s = \frac{1}{4}(C_{14} - C_{24} + 2C_{56}) \tag{S77}$$

$$E_c = \frac{1}{8}(C_{11} + C_{22} - 2C_{12} - 4C_{66}) \tag{S78}$$

$$E_s = -\frac{1}{2}(C_{16} - C_{26}) \tag{S79}$$

We use the script notation $\mathcal{A}, \mathcal{C}, \mathcal{N}, \mathcal{L}$, and $\mathcal{F}$ for the five azimuthally averaged elastic combinations that define the reference VTI medium used in Appendix A of the main text. This notation also distinguishes $\mathcal{A}$ from the coupling integral A.

J_c (J_s), K_c (K_s) and M_c (M_s) are body wave 1ψ azimuthal anisotropy parameters and D_c (D_s) is the body wave 3ψ azimuthal anisotropy parameter, which were not included by Montagner & Nataf (1986). G_c (G_s), B_c (B_s) and H_c (H_s) are 2ψ azimuthal anisotropic parameters for both body

waves and surface-waves. E_c (E_s) is the 4ψ azimuthal anisotropic parameter for both body waves and surface-waves.

For a TTI medium in which the strike of anisotropy lies along the x_1-axis, all parameters with the "s" subscript are zero, so 13 of the anisotropic parameters are non-zero, forming a medium with effective monoclinic symmetry.